

Deep imaging inside scattering media through virtual spatiotemporal wavefront shaping

Yiwen Zhang^{1,†}, Minh Dinh^{1,†}, Zeyu Wang¹, Tianhao Zhang¹, Tianhang Chen^{1,2}, and Chia Wei Hsu^{1*}

¹Ming Hsieh Department of Electrical and Computer Engineering,
University of Southern California, Los Angeles, California 90089,
USA ²Interdisciplinary Center for Quantum Information,

State Key Laboratory of Modern Optical Instrumentation,
College of Information Science and Electronic Engineering, Zhejiang University,
310027 Hangzhou, China [†]These authors contributed equally to this work

The multiple scattering of light makes materials opaque and obstructs imaging. Wavefront shaping can reverse the scattering process, but imaging with physical wavefront shaping has limitations such as requiring physical guidestars, being restricted within a small isoplanatic volume, and relying on slow wavefront updates, with some approaches only working for planar targets outside the scattering media. Here, we introduce scattering matrix tomography (SMT): measure the hyperspectral scattering matrix of the sample, use it to digitally scan a synthesized confocal spatiotemporal focus and construct a volumetric image of the sample, and then use the tomograms as virtual guidestars in a nonconvex optimization to find the pulse shape, input wavefront, and output wavefront that can compensate for aberrations and scattering. SMT combines the strengths of wavefront shaping, spatiotemporal gating, and computational adaptive optics, eliminating physical guidestars and enabling digital double-path wavefront corrections tailored for every isoplanatic volume. We demonstrate sub-micron lateral resolution and one-micron axial resolution at one millimeter beneath *ex vivo* mouse brain tissue and over three transport mean free paths inside an opaque colloid, where existing imaging methods all fail due to the overwhelming multiple scattering. As a noninvasive and label-free method that works both inside and outside the scattering media, SMT may be applied broadly across medical imaging, biological science, device inspection, and colloidal physics.

I. INTRODUCTION

Light scattering from inhomogeneities scrambles the wavefront and attenuates the signal exponentially while obscuring it with a speckled multiple-scattering background.^{1,2} Overcoming light scattering to image at high resolution deep inside opaque media is a grand challenge that can enable through-skull optical imaging and stimulation, surgery-free biopsy, observation of cellular processes in their natural state, optical characterization of bulk colloids, high-resolution nondestructive device testing, and many other applications.

Traditional imaging methods tackle this problem by filtering away the multiple-scattering background. The reflectance confocal microscopy (RCM)^{3,4} uses spatial gating. Optical coherence tomography (OCT)⁵ applies a coherence gate. The axial span of the spatial beam (which is twice the Rayleigh range) must cover the axial span of the image (*i.e.*, the depth of field Δz), so OCT operates with a small numerical aperture (NA), leading to a coarse lateral resolution (typically 5–20 μm). Optical coherence microscopy (OCM)⁶ combines spatial filtering and coherence gating while trading off the depth of field. Interferometric synthetic aperture microscopy⁷ extends the depth of field, though its signal decreases with the loss of confocal gates away from the focal plane. Hardware,⁸ computational,^{9–12} and hybrid¹³ adaptive optics can restore the resolution of images blurred by aberrations but cannot

overcome severe scattering as they do not control the numerous scattering modes in both the incident and the return paths. Multiphoton microscopy adopts longer wavelengths where scattering is weaker but requires fluorescence labeling and high-power lasers.^{14,15} Tomographic phase microscopy quantitatively obtains the refractive index distribution^{16–20} but requires thin specimens and access to both sides of the sample for transmission measurements. Selective detection of the forward scattered photons^{21,22} and photoacoustic tomography²³ allow imaging deeper at reduced resolution. The depth-over-resolution ratio stays around or below 200 in biological tissue across most label-free imaging methods (including non-optical ones such as ultrasound, X-ray CT, and MRI).^{23–26}

Over the past decade, a paradigm shift came with the appreciation that light scattering is deterministic and controllable. Given enough control elements, a suitable incident wavefront can reverse multiple scattering^{27,28} thanks to the time-reversal symmetry of Maxwell's equations. Adopting such wavefronts can, in principle, allow imaging at much deeper depths. But the initial methods to determine these special wavefronts come with serious limitations as they introduce physical guidestars at the imaging site²⁹ such as invasive cameras^{30,31} or photorefractive crystals,^{32,33} fluorescence labels,^{34–37} acoustic foci with greatly reduced spatial resolution,^{38,39} or isolated moving particles.^{40,41} Additionally, each wavefront is only valid within a volume called the isoplanatic patch,⁸ whose size shrinks with depth and is less than 10 μm at 1 mm deep inside biological tissue.^{42,43} Most of these methods also require a spatial light modu-

* cwhsu@usc.edu

lator (SLM) with a limited update speed. Such physical-guidestar-based schemes are schematically illustrated in Fig. 1a. To avoid using physical guidestars, researchers developed incoherent imaging methods based on angular correlations^{44,45} and optimization.^{46–49} However, they only apply to planar targets at a large distance away from the scattering media because there is no gating mechanism for depth sectioning and because the small angular memory effect range limits the field of view. Reflection matrix measurement is another way to avoid physical guidestars. One can accumulate single-scattering signals using correlations in the reflection matrix⁵⁰ and remove aberrations and scattering through singular value decomposition^{51,52} or iterative phase conjugation,^{53–58} culminating in the “volumetric reflection-matrix microscopy” (VRM) method⁵⁸ that performs both spectral and angular corrections at multiple depths. These matrix-based methods show great potential but, to date, have yet to deliver the drastic beyond-adaptive-optics scattering reversal promised by wavefront shaping.

Here we use the scattering matrix to unify different approaches and combine the advantages of both the traditional and the recent methods, realizing label-free volumetric high-resolution imaging across a large depth of field deep inside the scattering media, with multi-isoplanatic spatiotemporal wavefront corrections on top of confocal and temporal gates while avoiding the restrictions of physical guidestars and slow SLMs. As illustrated in Fig. 1b, we measure the hyperspectral scattering matrix of the sample and use it to synthesize a spatiotemporal focus with pulse compression, refractive index mismatch correction, and wavefront correction for every isoplanatic volume. The focus is scanned digitally to yield a 3D image of the sample with no trade-off between the lateral resolution and the depth of field. We use the reconstructed image as virtual guidestars intrinsic to the sample and develop an optimization with regularization and progression strategies to find the optimal dispersion compensation and input/output wavefronts. This enables a depth-over-resolution ratio of 910 when imaging a resolution target at one millimeter beneath *ex vivo* mouse brain tissue—the highest reported in the literature (including both optical and non-optical label-free methods) to our knowledge. We attain diffraction-limited resolution when the signal is reduced by over ten-million-fold due to multiple scattering. We maintain the ideal transverse and axial resolutions across a depth of field of over 70 times the Rayleigh range at depths beyond three transport mean free paths inside an opaque colloid—the deepest reported to our knowledge. By formulating the problems of imaging and reversing light scattering as reconstruction and optimization problems, this approach offers a versatile platform that uses wave physics and computation to reveal hidden information.

II. SCATTERING MATRIX TOMOGRAPHY

The scattering matrix $S(\mathbf{k}_{\text{out}}, \mathbf{k}_{\text{in}}, \omega)$ encapsulates the sample’s complete linear response^{59,60} (Fig. 1c).

Any incident wave is a superposition of plane waves: $E_{\text{in}}(\mathbf{r}, t) = \sum_{\mathbf{k}_{\text{in}}, \omega} \tilde{E}_{\text{in}}(\mathbf{k}_{\text{in}}, \omega) e^{i\mathbf{k}_{\text{in}} \cdot \mathbf{r} - i\omega t}$, where $\mathbf{r} = (x, y, z)$ is the position, t is time, and $\tilde{E}_{\text{in}}(\mathbf{k}_{\text{in}}, \omega)$ is the amplitude of its plane-wave component with incoming momentum \mathbf{k}_{in} at frequency ω . The amplitudes $\tilde{E}_{\text{out}}(\mathbf{k}_{\text{out}}, \omega)$ that form the resulting outgoing wave $E_{\text{out}}(\mathbf{r}, t) = \sum_{\mathbf{k}_{\text{out}}, \omega} \tilde{E}_{\text{out}}(\mathbf{k}_{\text{out}}, \omega) e^{i\mathbf{k}_{\text{out}} \cdot \mathbf{r} - i\omega t}$ are given by the scattering matrix through $\tilde{E}_{\text{out}}(\mathbf{k}_{\text{out}}, \omega) = \sum_{\mathbf{k}_{\text{in}}} S(\mathbf{k}_{\text{out}}, \mathbf{k}_{\text{in}}, \omega) \tilde{E}_{\text{in}}(\mathbf{k}_{\text{in}}, \omega)$. The angular summations are restricted to $|\mathbf{k}|^2 = |\mathbf{k}_{\parallel}|^2 + k_z^2 = (n_{\text{bg}}\omega/c)^2$ in a background medium with speed of light c/n_{bg} ; we use “angle” interchangeably with “momentum.”

After measuring a subset of $S(\mathbf{k}_{\text{out}}, \mathbf{k}_{\text{in}}, \omega)$, one can digitally synthesize the sample’s response with tailored measurements in space-time given customized spatiotemporal inputs, which we collectively refer to as “virtual spatiotemporal wavefront shaping.” As illustrated in Fig. 1d, summing over incident angles \mathbf{k}_{in} with incoming plane-wave amplitudes $\tilde{E}_{\text{in}}(\mathbf{k}_{\text{in}}, \omega) = e^{-i\mathbf{k}_{\text{in}} \cdot \mathbf{r}_{\text{in}}}$ creates an incident beam $E_{\text{in}}(\mathbf{r}, \omega)$ spatially focused at \mathbf{r}_{in} , forming an input spatial gate; summing over outgoing angles \mathbf{k}_{out} with outgoing plane-wave amplitudes $\tilde{E}_{\text{out}}(\mathbf{k}_{\text{out}}, \omega)$ from the scattering matrix yields the scattered field $E_{\text{out}}(\mathbf{r} = \mathbf{r}_{\text{out}}, \omega)$ given a virtual detector at position \mathbf{r}_{out} , forming an output spatial gate; summing over frequency ω with an $e^{-i\omega(t-t_0)}$ phase creates an incident pulse that arrives at \mathbf{r}_{in} at time $t = t_0$, forming a temporal gate. Given a spatiotemporal focus arriving at \mathbf{r}_{in} at time t_0 , the scattered field is therefore $E_{\text{out}}(\mathbf{r}_{\text{out}}, t) = \sum_{\mathbf{k}_{\text{out}}, \mathbf{k}_{\text{in}}, \omega} S(\mathbf{k}_{\text{out}}, \mathbf{k}_{\text{in}}, \omega) e^{i\mathbf{k}_{\text{out}} \cdot \mathbf{r}_{\text{out}} - i\mathbf{k}_{\text{in}} \cdot \mathbf{r}_{\text{in}} - i\omega(t-t_0)}$. We then perform a virtual experiment with a confocal spatial focus ($\mathbf{r}_{\text{in}} = \mathbf{r}_{\text{out}} = \mathbf{r}$) and with the temporal focus aligned with the spatial one (evaluating E_{out} at time $t = t_0$), which yields the triply-gated scattering amplitude of the sample at position \mathbf{r} , denoted as

$$\psi_{\text{SMT}}(\mathbf{r}) = \sum_{\mathbf{k}_{\text{out}}, \mathbf{k}_{\text{in}}, \omega} e^{i(\mathbf{k}_{\text{out}} - \mathbf{k}_{\text{in}}) \cdot \mathbf{r}} S(\mathbf{k}_{\text{out}}, \mathbf{k}_{\text{in}}, \omega). \quad (1)$$

Digitally scanning \mathbf{r} (Fig. 1b) forms a phase-resolved image of the sample where the input spatial gate, output spatial gate, and temporal gate all align at every point in the absence of aberrations and scattering. The lateral spread of $\mathbf{k}_{\text{out}} - \mathbf{k}_{\text{in}}$ in the summation (typically set by the NA) determines the lateral resolution, with no degradation away from any particular focal plane. The axial spread (typically set by the spectral bandwidth) determines the axial resolution. The triple summation averages away random noises, providing a signal-to-noise ratio advantage akin to that of frequency-domain OCT over time-domain OCT.⁶¹ We use the non-uniform fast Fourier transform (NUFFT)⁶² to efficiently evaluate these summations and the 3D spatial scan. Eq. (1) is the minimal, optimization-free version of what we call “scattering matrix tomography” (SMT).

VRM used an object momentum conservation principle^{50,58} to reconstruct images at multiple en-face slices by performing time gating at one depth, summing over in-

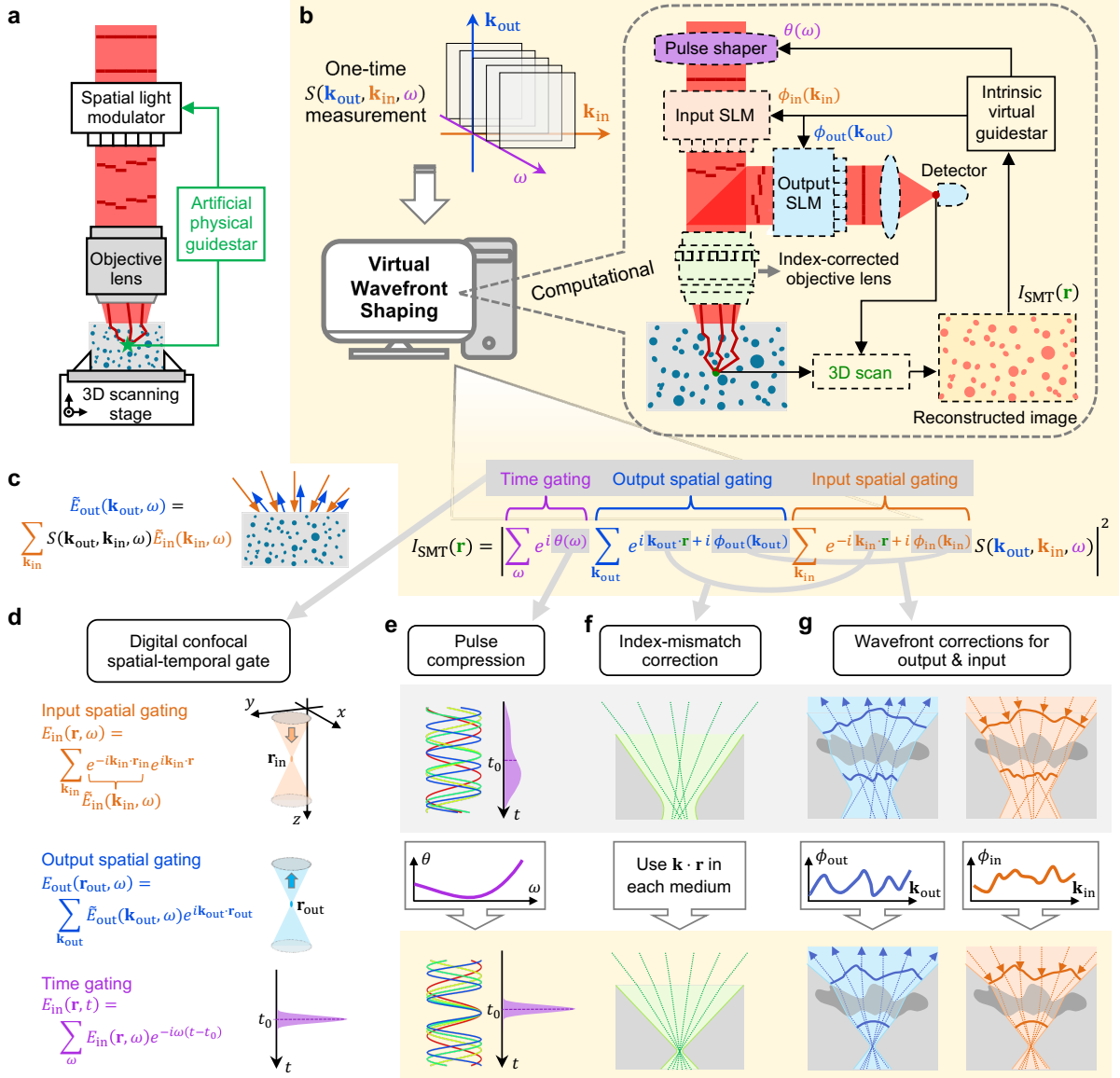


Fig. 1. Virtual spatiotemporal wavefront shaping and scattering matrix tomography (SMT). **a**, Imaging with wavefront modulated by physical lenses and a spatial light modulator (SLM) using feedback from artificially introduced physical guidestars. **b**, SMT imaging with virtual wavefront shaping that digitally performs spatiotemporal wavefront modulation, volumetric scanning, and optimization via Eqs. (2)–(3). The reconstructed image acts as virtual guidestars intrinsic to the sample, providing feedback noninvasively. **c**, The scattering matrix $S(\mathbf{k}_{out}, \mathbf{k}_{in}, \omega)$ relates any incident field $\vec{E}_{in}(\mathbf{k}_{in}, \omega)$ to the resulting scattered field $\vec{E}_{out}(\mathbf{k}_{out}, \omega)$. **d**, The scattering matrix can synthesize input spatial gating, output spatial gating, and time gating by summing over the incident momentum \mathbf{k}_{in} , outgoing momentum \mathbf{k}_{out} , and frequency ω respectively. **e–g**, Dispersion, refractive index mismatch at interfaces, and wavefront distortions (from both the optical system and the sample, including both aberrations and multiple scattering) degrade the gates. SMT corrects all of them digitally through a frequency-dependent phase $\theta(\omega)$ that acts as a virtual pulse shaper, appropriate momenta and phase coefficients for the medium that act as a virtual index-corrected objective lens, and angle-dependent phases $\phi_{in}(\mathbf{k}_{in})$ and $\phi_{out}(\mathbf{k}_{out})$ that act as two virtual SLMs.

cident angles while fixing the in-plane momentum transfer, performing a 2D inverse Fourier transform, and then looping over the depth.⁵⁸ In comparison, SMT uses a virtual scanning of a confocal spatiotemporal focus, which results in a simpler and more intuitive formalism, enables slicing in any orientation or direct volumetric reconstruction, generalizes the use of reflection matrix to

any subset of the scattering matrix (can also be transmission, remission,^{21,63} or a combination of them), adopts NUFFT which is much faster than brute-force summations and loops, and offers a rigorous basis for performing the index-mismatch correction and focus-quality-based spatiotemporal wavefront corrections below.

The triple gating suppresses multiple scattering. The

single-scattering field at output \mathbf{k}_{out} for an input from \mathbf{k}_{in} is given by the Born approximation as proportional to $\tilde{\eta}(\mathbf{q})$, namely the $\mathbf{q} = \mathbf{k}_{\text{out}} - \mathbf{k}_{\text{in}}$ component of the 3D Fourier transform of the sample's permittivity contrast profile $\eta(\mathbf{r})$.^{5,16,17,64} Such single-scattering contributions add up in phase in Eq. (1) to form the image, similar to an inverse Fourier transform from $\tilde{\eta}(\mathbf{q})$ to $\eta(\mathbf{r})$. The multiple-scattering contributions do not add up in phase. Therefore, the triple summations over \mathbf{k}_{out} , \mathbf{k}_{in} , and ω boost the single-to-multiple-scattering ratio in $\psi_{\text{SMT}}(\mathbf{r})$ compared to the raw measurement data $S(\mathbf{k}_{\text{out}}, \mathbf{k}_{\text{in}}, \omega)$.

To remove aberrations and scattering, we perform digital spatiotemporal wavefront corrections. The chromatic aberrations in the optical elements of the system and the frequency dependence of the refractive index in the sample create a frequency-dependent phase that misaligns and broadens the temporal gate. In SMT, we digitally compensate for such dispersion using a spectral phase $\theta(\omega)$ acting as a virtual pulse shaper (Fig. 1e), similar to the dispersion compensation in spectral-domain OCT.⁶⁵ The refractive index mismatch between the sample medium (*e.g.*, biological tissue), the far field (*e.g.*, air), and the coverslip (if there is one) refracts the rays, degrades the input and output spatial gates,⁶⁶ and misaligns the spatial gates and the temporal gate. By using the appropriate propagation phase shift $(\mathbf{k}_{\text{out}} - \mathbf{k}_{\text{in}}) \cdot \mathbf{r}$ in each medium and the appropriate arrival time, SMT achieves an ideal spatiotemporal focus at all depths even in the presence of refraction, effectively creating a virtual dry objective lens that reverses both the spatial and the chromatic aberrations arising from the index mismatch (Fig. 1f) without liquid immersion (Supplementary Sect. III C). Importantly, we also digitally introduce angle-dependent phase profiles $\phi_{\text{in}}(\mathbf{k}_{\text{in}})$ and $\phi_{\text{out}}(\mathbf{k}_{\text{out}})$ that act as two virtual SLMs, one for the incident wave and one for the outgoing wave (Fig. 1g), which can adopt any wavefront to compensate for scattering and additional aberrations. This yields the general form of SMT,

$$I_{\text{SMT}}(\mathbf{r}) = \left| \sum_{\omega} e^{i\theta(\omega)} \sum_{\mathbf{k}_{\text{out}}} e^{i\mathbf{k}_{\text{out}} \cdot \mathbf{r} + i\phi_{\text{out}}(\mathbf{k}_{\text{out}})} \sum_{\mathbf{k}_{\text{in}}} e^{-i\mathbf{k}_{\text{in}} \cdot \mathbf{r} + i\phi_{\text{in}}(\mathbf{k}_{\text{in}})} S(\mathbf{k}_{\text{out}}, \mathbf{k}_{\text{in}}, \omega) \right|^2. \quad (2)$$

By measuring the reflection from a mirror, we remove the dispersion and aberrations in the input path of the optical system (Supplementary Sect. III B).

To find the digital corrections $\theta(\omega)$, $\phi_{\text{in}}(\mathbf{k}_{\text{in}})$, and $\phi_{\text{out}}(\mathbf{k}_{\text{out}})$, we recognize that a good spatiotemporal focus at \mathbf{r} enhances the scattering intensity from targets at that position, so $I_{\text{SMT}}(\mathbf{r})$ acts as a virtual noninvasive guidestar at \mathbf{r} (Fig. 1b). Therefore, we maximize an image quality metric M ,

$$\{\theta, \phi_{\text{in}}, \phi_{\text{out}}\} = \arg \max_{\theta, \phi_{\text{in}}, \phi_{\text{out}}} M, \quad M = \sum_{\mathbf{r}} I_{\text{SMT}}(\mathbf{r}) \ln \frac{I_{\text{SMT}}(\mathbf{r})}{I_0} \quad (3)$$

with I_0 being a constant; the logarithm factor promotes image sharpness.^{12,67} Image-metric-based optimizations have long been used in adaptive optics^{8–13} and more recently with wavefront shaping without a time gate;^{37,46,48} motivated by the versatility of optimization problems, here we generalize this approach to perform double-path spatiotemporal digital wavefront correction. We derive the gradient of M with respect to the parameters and adopt a quasi-Newton method, the low-storage Broyden–Fletcher–Goldfarb–Shanno (L-BFGS) method,⁶⁸ in the NLOpt library.⁶⁹ Since a wavefront $\phi_{\text{in}}(\mathbf{k}_{\text{in}})$ or $\phi_{\text{out}}(\mathbf{k}_{\text{out}})$ can only remain optimal within an isoplanatic volume,^{8,42,43} we divide the space into zones (both axially and laterally) and use different $\phi_{\text{in/out}}$ for different zones.

A direct optimization, however, performs poorly when the scattering is sufficiently strong that signals from the target are initially buried under the speckled multiple-scattering background (Fig. 2a–f). This happens because (1) the problem is high-dimensional and nonconvex with numerous poor local optima, (2) the large number of parameters in $\theta(\omega)$, $\phi_{\text{in}}(\mathbf{k}_{\text{in}})$, and $\phi_{\text{out}}(\mathbf{k}_{\text{out}})$ in the many zones can lead to overfitting, and (3) the optimization may inadvertently enhance unintended contributions like the speckled background instead of signals from a target at the specified position \mathbf{r} . To overcome these challenges, we employ five strategies to regularize the problem, lower its dimension, and guide the search away from poor local optima associated with unintended contributions (Supplementary Sect. III E–F): (i) Restrict $\theta(\omega)$ to a third-order polynomial.^{12,65} (ii) Expand $\phi_{\text{in}}(\mathbf{k}_{\text{in}})$ and $\phi_{\text{out}}(\mathbf{k}_{\text{out}})$ in Zernike polynomials.^{8,10–13,70} (iii) First optimize $\phi_{\text{in/out}}$ over the full volume and then progressively optimize over smaller zones while using the previous $\phi_{\text{in/out}}$ as the initial guess. (iv) Truncate the scattering matrix to within the respective spatial zone to avoid overfitting. (v) Increase the number of Zernike terms as we progress to smaller zones, since the low-order terms correct for slowly varying aberrations with a large isoplanatic volume, while the high-order terms correct for the sharp variations from localized scattering with a small isoplanatic volume. These strategies work together to enable an effective optimization (Fig. 2g–k).

Since all targets within an isoplanatic volume share the same optimal wavefront while the speckled backgrounds do not, the summation over space \mathbf{r} in Eq. (3) promotes the target-to-speckle weight in the gradient and makes the optimization landscape smoother. As discussed earlier, the triple gating through summations over \mathbf{k}_{out} , \mathbf{k}_{in} , and ω in Eq. (2) also promotes the target-to-speckle ratio. Without one of these quadruple summations in $\{\mathbf{r}, \mathbf{k}_{\text{out}}, \mathbf{k}_{\text{in}}, \omega\}$ and when scattering is sufficiently strong, the optimization landscape may not reflect the target contribution and may exhibit many local optima associated with the multiple-scattering background (Supplementary Fig. 14).

Previous matrix-based imaging methods used singular value decomposition⁵² or iterative phase conjugation^{53–58} to perform angular wavefront corrections. They were not

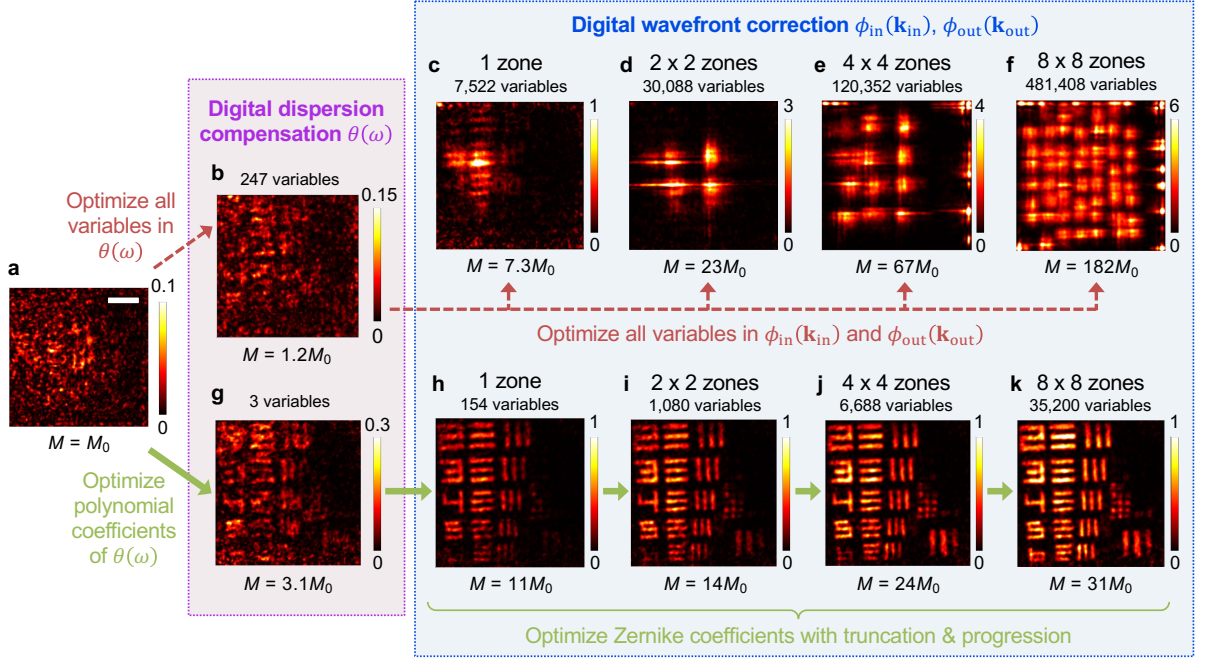


Fig. 2. SMT digital dispersion compensation and wavefront corrections. SMT finds the digital corrections $\theta(\omega)$, $\phi_{\text{in}}(\mathbf{k}_{\text{in}})$, and $\phi_{\text{out}}(\mathbf{k}_{\text{out}})$ by optimizing an image quality metric M , Eq. (3). Different spatial zones of the image use different $\phi_{\text{in/out}}$. Each panel shows the SMT image $I_{\text{SMT}}(\mathbf{r})$ of the USAF-target-under-tissue sample of Fig. 4 in this process, at the depth where M is maximized. A direct optimization (red dashed arrows) leads to overfitting and gets trapped in poor local optima. Through regularization and progression strategies described in the text (green solid arrows), SMT finds the digital corrections that restore the spatiotemporal focus and achieve a good image quality. Note that the image before optimization in (a) already incorporates triple (temporal, input spatial, and output spatial) gating, index-mismatch correction, and removal of the dispersion and aberrations in the input path of the optical system. Scale bar: 10 μm .

formulated as an image-metric optimization like Eq. (3) and did not have the above-mentioned regularization and progression strategies, which limited their performance when scattering is strong. The VRM method⁵⁸ also employed dispersion compensation, but it did so using an iterative phase conjugation scheme with a single angular summation instead of quadruple summations, which further restricted it to situations with less scattering.

III. EXPERIMENTAL DEMONSTRATION

We use off-axis holography⁷¹ to measure the field $\tilde{E}_{\text{out}}(\mathbf{k}_{\text{out}}, \omega)$ scattered from the sample to the incident side (Fig. 3) through a dry objective lens (Mitutoyo M Plan Apo NIR 100X, NA = 0.5). Here, $S(\mathbf{k}_{\text{out}}, \mathbf{k}_{\text{in}}, \omega)$ reduces to the reflection matrix $R(\mathbf{k}_{\text{out}}, \mathbf{k}_{\text{in}}, \omega)$. A CMOS camera (Photron Fastcam Nova S6) captures 64,000 columns of the reflection matrix per second, a dual-axis galvo scanner (ScannerMAX Saturn 5B) scans the incident angle \mathbf{k}_{in} , and a tunable laser (M Squared SolsTiS 1600) scans the frequency ω . The data acquisition here is two to three orders of magnitude faster than previous measurements of broadband scattering matrices.^{58,60,72} The power onto the sample ranges from 0.02 mW to 0.2 mW. We measure around 250 wavelengths λ from

740 nm to 940 nm, 2,900 outgoing angles, and 3,900 incident angles within the NA, over a $51 \times 51 \mu\text{m}^2$ area. The detection sensitivity, currently limited by the residual reflection from the objective lens, is 90 dB. See Supplementary Sects. I–II for details.

A. Planar Imaging

We first image the 8th group (whose 6th element has a bar width and separation of 1.1 μm) of a 1951 USAF resolution target underneath a 0.98-mm-thick tissue slice from the cerebral cortex of a mouse brain (Fig. 4a). A standard bright-field microscope image (with incoherent white-light illumination) shows no feature (Fig. 4b).

Using the measured hyperspectral reflection matrix, we first mimic existing reflection-based imaging methods virtually (Supplementary Sect. IV): restricting the frequency summation of Eq. (2) to one frequency yields a synthetic RCM image where time gating is absent (Fig. 4c); restricting the angular summations of Eq. (2) to small angles (we use NA = 0.1 here) and fixing the depth of the spatial focus yields a synthetic OCT image (Fig. 4d); for OCM (Fig. 4e), we sum over all frequencies and all angles. The depth of the focal plane is chosen to maximize the total signal. All of these images include corrections for the input aberrations of the optical system. For OCT and OCM, we also perform digital disper-

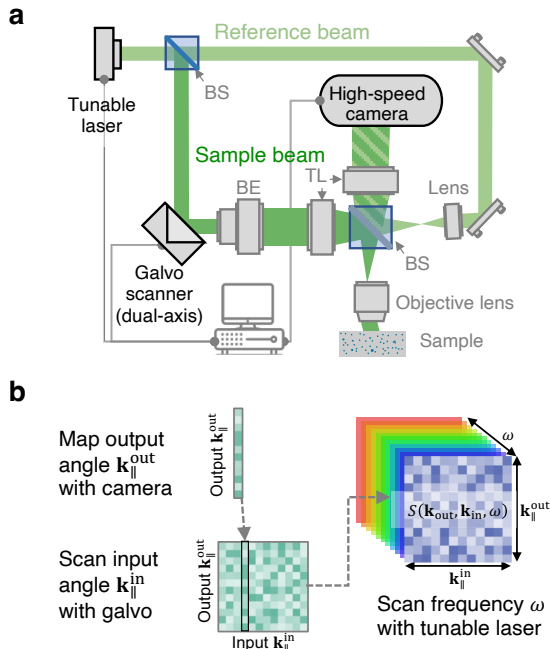


Fig. 3. Measurement of the hyperspectral reflection matrix. **a**, We use off-axis holography to measure the phase and amplitude of fields scattered by the sample. BS: beam splitter; BE: beam expander; TL: tube lens. See Supplementary Fig. 1 for a detailed schematic. **b**, Construction of the data cube by mapping the output angles with the camera, scanning the input angle with the galvo, and scanning the frequency with the tunable laser.

sion compensation (following the same steps as in SMT). Despite the confocal spatial gate, temporal gate, corrections, and even computational adaptive optics (Supplementary Sect. IV C), none of these methods reveals any group-8 element due to the overwhelming scattering from the tissue. To compare to the most state-of-the-art, we also implement the VRM method.⁵⁸ VRM fails (Fig. 4f) and performs worse than SMT without the five regularization and progression strategies (Fig. 2c) because its dispersion compensation is determined through a single angular summation without time gating and without confocal gating (Supplementary Sect. IV D).

The SMT image resolves the 8th group of the USAF target with near perfection down to the smallest 6th element (Fig. 4g). Here, the progression goes down to 8×8 zones, with up to 22 Zernike radial orders (275 Zernike polynomials) per zone in both ϕ_{in} and ϕ_{out} , for a total of 35,200 wavefront correction variables. The optimized correction patterns $\phi_{\text{in}}(\mathbf{k}_{\parallel}^{\text{in}})$ and $\phi_{\text{out}}(\mathbf{k}_{\parallel}^{\text{out}})$ are shown in Fig. 4h. Here, $\phi_{\text{out}}(\mathbf{k}_{\parallel}) \neq \phi_{\text{in}}(-\mathbf{k}_{\parallel})$ because the former includes the optical-system aberration. The wavefronts vary faster at larger angles due to the longer propagation length through the medium and subsequently more severe scattering. These large-angle fast-oscillation patterns correct for the strongest scattering and are key to the wavefront correction (Supplementary Fig. 12).

The triple gating is essential. Supplementary Sects. V–VI show that when one of the three gates is removed, the image reconstruction would completely fail even after the optimizations. It is also crucial to perform corrections for both the incident path and the return path; Supplementary Sect. IV C shows that in the reciprocal space $\mathbf{q} = \mathbf{k}_{\text{out}} - \mathbf{k}_{\text{in}}$ of the image, only low-order aberrations can be corrected because high-order terms require double-path wavefront corrections in both \mathbf{k}_{in} and \mathbf{k}_{out} .¹³ No existing computational adaptive optics methods^{9–13} performs double-path corrections, so they would not be able to handle a strongly scattering system like this even if they adopt the optimization strategies here.

To quantify the imaging performance, we obtain the point spread function (PSF) by evaluating Eq. (2) with a variable output position $\mathbf{r} = \mathbf{r}_{\text{in}} + \Delta\mathbf{r}$ given a fixed input position \mathbf{r}_{in} on the sixth element: $\text{PSF}(\mathbf{r}) = I(\mathbf{r}, \mathbf{r}_{\text{in}})$; see Supplementary Sect. VII. The PSFs of RCM, OCT, OCM, and VRM (Fig. 4i–l) have no discernible peak near $\Delta\mathbf{r} = 0$, indicating a complete failure to image. The speckled OCM PSF averages to be 70 dB below the peak PSF of a mirror without the brain tissue (Fig. 4n), so the signal (which is buried beneath the speckled background and not visible here) has been reduced by at least ten-million-fold due to multiple scattering. The PSF of SMT (Fig. 4m) exhibits a sharp peak at $\Delta\mathbf{r} = 0$ with 7-times the height of the tallest speckle in the background, showing we have not reached the depth limit (where the signal strength equals the background strength) of SMT yet. The SMT peak’s full width at half maximum (FWHM) is $1.08 \mu\text{m}$, close to the mirror PSF’s $0.93 \mu\text{m}$ FWHM, demonstrating diffraction-limited resolution despite the overwhelming multiple scattering. To our knowledge, the depth-over-FWHM ratio of 910 here is the highest reported in the literature for imaging high-contrast targets inside or behind ex vivo biological tissue, which scatters about twice as much as in vivo tissue.⁷³

B. Volumetric Imaging

We next perform 3D tomography of a dense colloid consisting of high-index titanium dioxide (TiO_2 , refractive index 2.5) nanoparticles dispersed in polydimethylsiloxane (PDMS, refractive index 1.4). The nanoparticles (Sigma-Aldrich, 914320) have a typical diameter of 500 nm, and we use Mie theory to estimate the scattering and transport mean free paths to be $\ell_{\text{sca}} = 0.19 \text{ mm}$ and $\ell_{\text{tr}} = 0.47 \text{ mm}$ at $\lambda = 840 \text{ nm}$ (Supplementary Sect. VIII). We measure the reflection matrix over a $51 \times 51 \mu\text{m}^2$ field of view with the reference plane at depth $z_0 = 1.525 \text{ mm}$. Using the reflection matrix, we reconstruct SMT image over a $50 \times 50 \times 110 \mu\text{m}^3$ volume inside the colloid by dividing the depth of field (DOF) $\Delta z = 110 \mu\text{m}$ into 16 sub-volumes vertically.

SMT creates a detailed 3D image of all the nanoparticles in this volume (Fig. 5a), with zoom-ins and cross sections of individual particles shown in Fig. 5f,k,l. A statistical analysis of these particles finds the lateral FWHM to vary from $0.7 \mu\text{m}$ to $1.0 \mu\text{m}$ within the $110 \mu\text{m}$

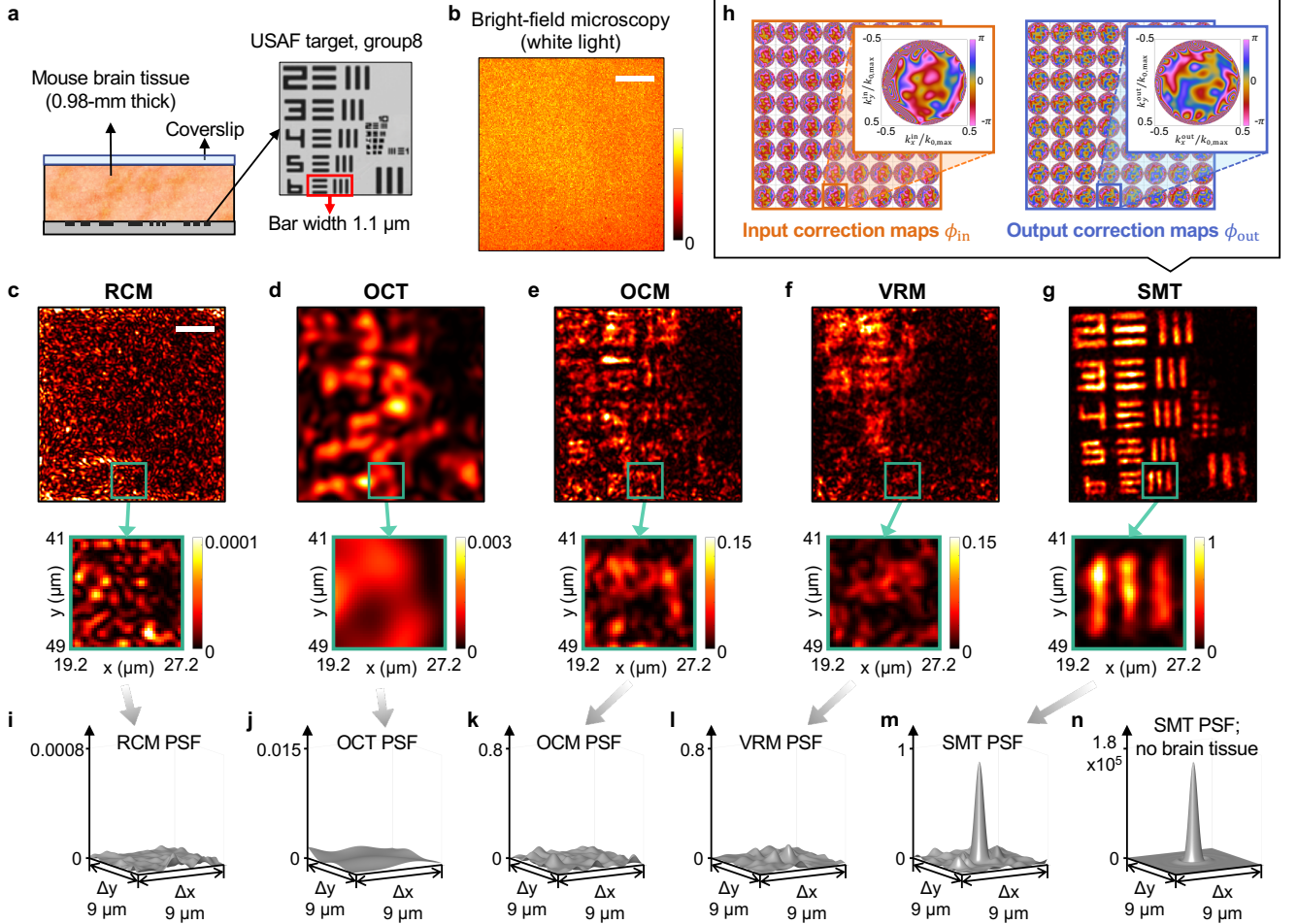


Fig. 4. Noninvasive imaging through thick tissue. **a**, Schematic of the sample—a USAF resolution target underneath 0.98 mm of mouse brain tissue—and a scanning electron microscope image of the USAF target before covered by the tissue. **b**, A standard bright-field microscope image of the sample (with white-light illumination). **c–f**, Reflectance confocal microscopy (RCM), optical coherence tomography (OCT), optical coherence microscopy (OCM), and volumetric reflection-matrix microscopy (VRM) images at the USAF target plane, synthesized from the measured hyperspectral reflection matrix. **g**, SMT image, $I_{\text{SMT}}(\mathbf{r})$, from Eqs. (2)–(3). Each pair of full view and zoom-in uses the same colorbar, and all images share the same normalization, with scales indicated on the colorbars. Scale bar in **b–c**: 10 μm . **h**, The wavefront correction phase maps for the 8×8 zones in SMT. **i–n**, Corresponding point spread function $\text{PSF}(\mathbf{r})$ of the sample (**i–m**) and of a mirror in air (**n**), centered at $(x_{\text{in}}, y_{\text{in}}) = (23.4, 45.0)$ μm .

DOF and the axial FWHM very close to the theoretical estimate of 1.42 μm given the spectral bandwidth of $\Delta\lambda = 187$ nm here (Supplementary Sect. IX). Fig. 5m,n shows examples of SMT images of nearby particle pairs, with one pair separated horizontally by 0.94 μm and one pair separated vertically by 1.48 μm . The SMT DOF covers approximately the volume of overlap among the input/output beams in the scattering matrix measurement; it grows with the field of view and is not restricted by the Rayleigh range z_{R} (Supplementary Sect. IX B). Here, $z_{\text{R}} = n_{\text{sam}}\lambda_0/(\pi\text{NA}^2) \approx 1.5$ μm (with center wavelength $\lambda_0 = 840$ nm and $n_{\text{sam}} = 1.4$ for PDMS), while the SMT DOF is 73 times larger.

We also construct VRM (generalized from multi-slice to volumetric) and synthetic OCM, OCT, and RCM im-

ages (Fig. 5b–e) for comparison, with longitudinal and transverse slices shown in Fig. 5g–j,l. For OCM and OCT, the depth of the spatial gate is fixed on one focal plane at $z_0 = 1.525$ mm when the temporal gate is scanned in z (Supplementary Sect. IV B). All of these methods fail and cannot identify any of the nanoparticles at these depths. The VRM image exhibits bright artifacts at several constant- z slices because its dispersion compensation maximizes the intensity at those isolated slices (Supplementary Sect. IV D).

IV. DISCUSSION

SMT provides a conceptually and mathematically simple framework that combines the advantages of existing methods while offering versatile capabilities. The main

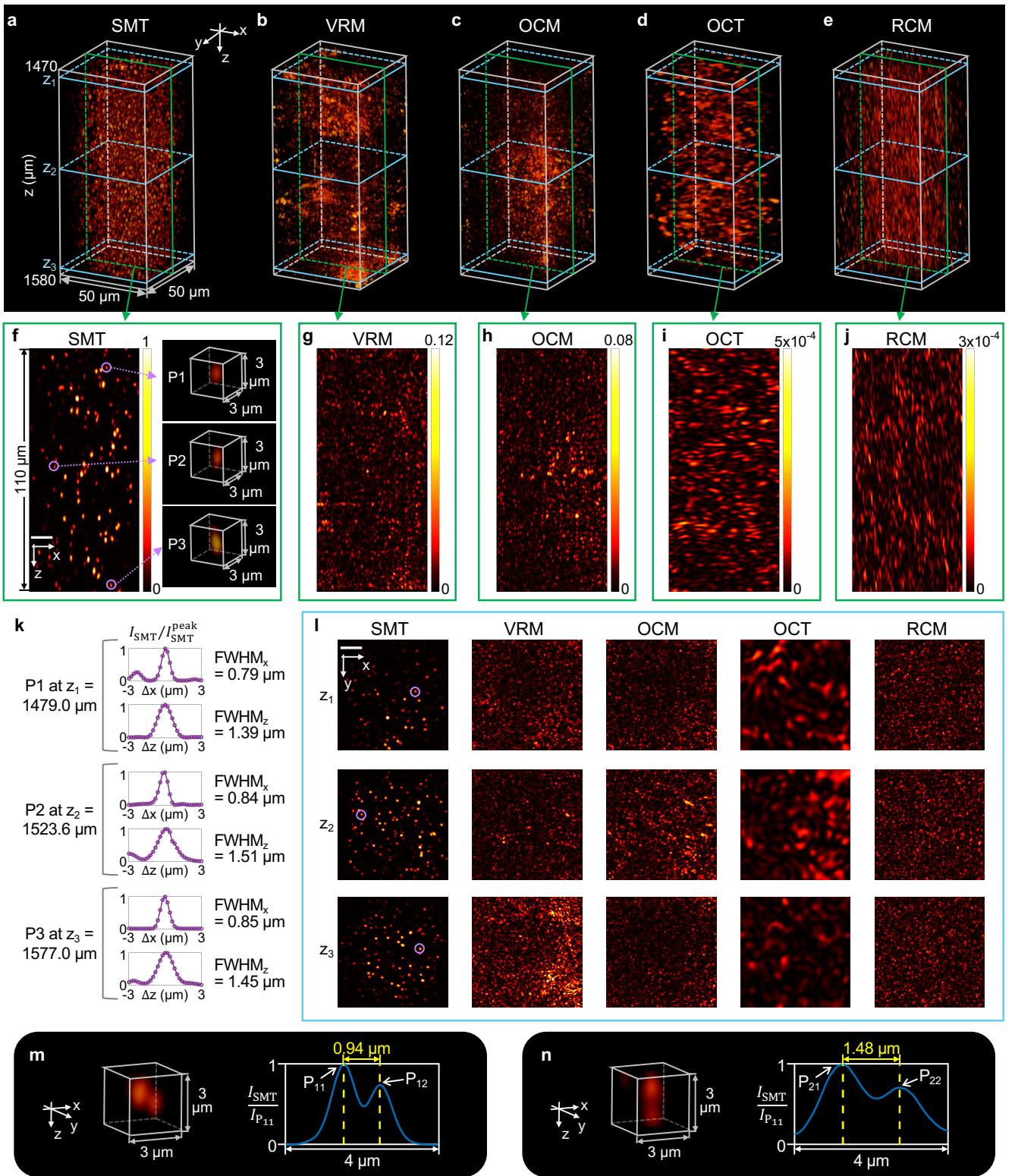


Fig. 5. Volumetric imaging inside a dense colloid. The sample consists of 500-nm-diameter TiO_2 nanoparticles dispersed in PDMS, with an estimated transport mean free path of 0.47 mm. **a–e**, SMT, VRM, OCM, OCT, and RCM images built from the measured hyperspectral reflection matrix. **f–j**, A longitudinal slice of the images at $y = 23.2 \mu\text{m}$ and close-up views of three particles at different depths in the SMT image. **k**, Cross sections of the three particles; $\Delta \mathbf{r} = \mathbf{r} - \mathbf{r}_{\text{peak}}$. **l**, Transverse slices at the depths of the three particles. **m, n**, SMT images of particles separated horizontally (**m**) and vertically (**n**), with center-to-center cross sections. $\mathbf{r}_{P_{11}} = (46.39, 31.29, 1487.31) \mu\text{m}$, $\mathbf{r}_{P_{12}} = (46.90, 31.96, 1487.74) \mu\text{m}$, $\mathbf{r}_{P_{21}} = (44.04, 39.12, 1569.56) \mu\text{m}$, and $\mathbf{r}_{P_{22}} = (44.18, 38.92, 1571.02) \mu\text{m}$. Scale bars in **f** and **l**: 10 μm . All images share the same normalization. Volumetric images and 2D slices use the same colorbar.

aspect not considered in this work is the frequency dependence of the wavefront correction. It is well known that the optimal wavefront for focusing behind scattering media depends sensitively on the frequency.⁷⁴ Future work can explore optimization strategies that incorporate the frequency dependence in ϕ_{in} and ϕ_{out} while avoiding overfitting due to the additional degrees of freedom. One may also adopt a progressive increase of the NA¹² to utilize the deeper penetration of the forward scattered photons,^{21,22} and/or a progressive increase of the depth.⁵⁸ Global optimization can be used when the scattering is so strong that a local optimization loses its consistency. Future work may also explore other optimization schemes beyond using an image quality metric.

Validation against the ground truth is nontrivial for volumetric imaging.⁷⁵ Using the recent “augmented partial factorization” simulation method,⁷⁶ we have validated SMT through full-wave numerical simulations.⁷⁷

One can interpret RCM, OCT, and OCM as measuring the diagonal elements of the reflection matrix in a spatial basis. SMT utilizes the additional off-diagonal elements to digitally refocus to different planes and to enable double-path wavefront corrections. The price is having to measure those off-diagonal elements.

Motion artifacts make wavefront shaping *in vivo* a challenge.⁷⁸ While the virtual wavefront shaping of SMT dispenses with slow SLMs, a coherent synthesis still requires measuring the matrix elements before the scatterer arrangement changes substantially. The speckle decorrelation time, primarily limited by the blood flow, is estimated as 5 ms at $\lambda = 633$ nm wavelength 1 mm deep inside the mouse brain where blood is rich⁷⁹ but can go beyond 30 seconds for the skull where there is less blood.⁵⁵ Currently, our total measurement time for the USAF-target-under-tissue sample is three minutes, with the majority of which spent on the mechanical acceleration and deceleration of a birefringent filter during a scan-and-stop operation of the tunable laser. Scanning the filter continuously can reduce the measurement time to 5 seconds (Supplementary Sec. ID). One can further accelerate by orders of magnitude through truncating the spatial measurement,⁵⁷ parallelizing the spectral acquisition,⁸⁰ and reducing the number of frequencies or incident angles (Supplementary Sect. V–VI).

While SMT uses contrasts in the scattering strength,

digital staining^{81,82} may be used to infer other contrasts. The phase information in ψ_{SMT} can help detect sub-mm displacements.^{83,84} One may incorporate polarization gating to select birefringent objects such as directionally oriented tissues. The hyperspectral scattering matrix can additionally resolve spectral information of the sample, such as the oxygenation of the hemoglobin. Applications that require feedback to identify the region of interest can use a subset of the matrix data to reconstruct a coarse image in real time.

Note: After we posted a preprint of this paper,⁸⁵ a related preprint was posted by an independent group.⁸⁶

Data availability: The datasets generated and analyzed during the current study are available on Zenodo.⁸⁷

Code availability: The codes used to produce the results of the study are available on GitHub.⁸⁸

Acknowledgments: We thank B. Applegate, S. Fraser, O. D. Miller, F. Xia, and B. Flanagan for helpful discussions. This work was supported by the Chan Zuckerberg Initiative, the National Science Foundation CAREER award (ECCS-2146021), and the University of Southern California.

Author contributions: Y.Z. and C.W.H. designed the experimental setup. Y.Z. built the setup, prepared the samples, and carried out the measurements with help from M.D. M.D. and Y.Z. developed and carried out the dispersion compensation. M.D. developed and carried out the SMT wavefront optimization with regularization and progression. Z.W. developed fast 3D reconstruction using the non-uniform fast Fourier transform. Y.Z. and Z.W. developed the index-mismatch correction. Y.Z., T.Z., and T.C. developed the control and automation of the instruments. M.D. and Y.Z. implemented the synthesis of RCM, OCT, and OCM. M.D. implemented VRM. Y.Z. performed the 3D visualization and the analyses on phase stability, sensitivity, and resolution. C.W.H. conceived the project and supervised research. C.W.H., Y.Z., and M.D. wrote the manuscript with inputs from the other coauthors. All authors discussed the results.

Competing interests: C.W.H, Z.W., Y.Z., and M.D. are inventors of US patent applications 17/972,073 and 63/472,900 titled “Multi-spectral scattering-matrix tomography” filed by the University of Southern California.

-
- [1] Yoon, S. *et al.* Deep optical imaging within complex scattering media. *Nat. Rev. Phys.* **2**, 141–158 (2020).
- [2] Bertolotti, J. & Katz, O. Imaging in complex media. *Nat. Phys.* **18**, 1008–1017 (2022).
- [3] Calzavara-Pinton, P., Longo, C., Venturini, M., Sala, R. & Pellacani, G. Reflectance confocal microscopy for *in vivo* skin imaging. *Photochem. Photobiol.* **84**, 1421–1430 (2008).
- [4] Xia, F. *et al.* *In vivo* label-free confocal imaging of the deep mouse brain with long-wavelength illumination. *Biomed. Opt. Express* **9**, 6545–6555 (2018).
- [5] Fercher, A. F., Drexler, W., Hitzinger, C. K. & Lasser, T. Optical coherence tomography—principles and applications. *Rep. Prog. Phys.* **66**, 239 (2003).
- [6] Aguirre, A. D., Zhou, C., Lee, H.-C., Ahsen, O. O. & Fujimoto, J. G. Optical coherence microscopy. In Drexler, W. & Fujimoto, J. G. (eds.) *Optical Coherence Tomography: Technology and Applications*, chap. 28, 865–911 (Springer, Cham, 2015).
- [7] Ralston, T. S., Marks, D. L., Scott Carney, P. & Boppart,

- S. A. Interferometric synthetic aperture microscopy. *Nat. Phys.* **3**, 129–134 (2007).
- [8] Hampson, K. M. *et al.* Adaptive optics for high-resolution imaging. *Nat. Rev. Methods Primers* **1**, 68 (2021).
- [9] Tippie, A. E., Kumar, A. & Fienup, J. R. High-resolution synthetic-aperture digital holography with digital phase and pupil correction. *Opt. Express* **19**, 12027–12038 (2011).
- [10] Adie, S. G., Graf, B. W., Ahmad, A., Carney, P. S. & Boppart, S. A. Computational adaptive optics for broadband optical interferometric tomography of biological tissue. *Proc. Natl. Acad. Sci. U.S.A.* **109**, 7175–7180 (2012).
- [11] Shemonski, N. D. *et al.* Computational high-resolution optical imaging of the living human retina. *Nat. Photon.* **9**, 440–443 (2015).
- [12] Hillmann, D. *et al.* Aberration-free volumetric high-speed imaging of in vivo retina. *Sci. Rep.* **6**, 35209 (2016).
- [13] Liu, S. *et al.* Closed-loop wavefront sensing and correction in the mouse brain with computed optical coherence microscopy. *Biomed. Opt. Express* **12**, 4934–4954 (2021).
- [14] Horton, N. G. *et al.* In vivo three-photon microscopy of subcortical structures within an intact mouse brain. *Nat. Photon.* **7**, 205–209 (2013).
- [15] Streich, L. *et al.* High-resolution structural and functional deep brain imaging using adaptive optics three-photon microscopy. *Nat. Methods* **18**, 1253–1258 (2021).
- [16] Jin, D., Zhou, R., Yaqoob, Z. & So, P. T. Tomographic phase microscopy: principles and applications in bioimaging. *J. Opt. Soc. Am. B* **34**, B64–B77 (2017).
- [17] Park, Y., Depeursinge, C. & Popescu, G. Quantitative phase imaging in biomedicine. *Nat. Photon.* **12**, 578–589 (2018).
- [18] Tahir, W., Kamilov, U. S. & Tian, L. Holographic particle localization under multiple scattering. *Adv. Photonics* **1**, 036003 (2019).
- [19] Lim, J., Ayoub, A. B., Antoine, E. E. & Psaltis, D. High-fidelity optical diffraction tomography of multiple scattering samples. *Light Sci. Appl.* **8**, 82 (2019).
- [20] Chen, M., Ren, D., Liu, H.-Y., Chowdhury, S. & Waller, L. Multi-layer Born multiple-scattering model for 3D phase microscopy. *Optica* **7**, 394–403 (2020).
- [21] Zhao, Y. *et al.* Dual-axis optical coherence tomography for deep tissue imaging. *Opt. Lett.* **42**, 2302–2305 (2017).
- [22] Cua, M., Blochet, B. & Yang, C. Speckle-resolved optical coherence tomography for mesoscopic imaging within scattering media. *Biomed. Opt. Express* **13**, 2068–2081 (2022).
- [23] Wang, L. V. & Hu, S. Photoacoustic tomography: in vivo imaging from organelles to organs. *Science* **335**, 1458–1462 (2012).
- [24] Pian, Q. *et al.* Multimodal biomedical optical imaging review: towards comprehensive investigation of biological tissues. *Curr. Mol. Imaging* **3**, 72–87 (2014).
- [25] Lal, C. & Leahy, M. J. An updated review of methods and advancements in microvascular blood flow imaging. *Microcirculation* **23**, 345–363 (2016).
- [26] Gigan, S. Optical microscopy aims deep. *Nat. Photon.* **11**, 14–16 (2017).
- [27] Rotter, S. & Gigan, S. Light fields in complex media: Mesoscopic scattering meets wave control. *Rev. Mod. Phys.* **89**, 015005 (2017).
- [28] Cao, H., Mosk, A. P. & Rotter, S. Shaping the propagation of light in complex media. *Nat. Phys.* **18**, 994–1007 (2022).
- [29] Horstmeyer, R., Ruan, H. & Yang, C. Guidestar-assisted wavefront-shaping methods for focusing light into biological tissue. *Nat. Photon.* **9**, 563–571 (2015).
- [30] Vellekoop, I. M. & Mosk, A. Focusing coherent light through opaque strongly scattering media. *Opt. Lett.* **32**, 2309–2311 (2007).
- [31] Popoff, S., Lerosey, G., Fink, M., Boccaro, A. C. & Gigan, S. Image transmission through an opaque material. *Nat. Commun.* **1**, 81 (2010).
- [32] Yaqoob, Z., Psaltis, D., Feld, M. S. & Yang, C. Optical phase conjugation for turbidity suppression in biological samples. *Nat. Photon.* **2**, 110–115 (2008).
- [33] Cheng, Z., Li, C., Khadira, A., Zhang, Y. & Wang, L. V. High-gain and high-speed wavefront shaping through scattering media. *Nat. Photon.* **17**, 299–305 (2023).
- [34] Tang, J., Germain, R. N. & Cui, M. Superpenetration optical microscopy by iterative multiphoton adaptive compensation technique. *Proc. Natl. Acad. Sci. U.S.A.* **109**, 8434–8439 (2012).
- [35] Papadopoulos, I. N., Jouhanneau, J.-S., Poulet, J. F. & Judkewitz, B. Scattering compensation by focus scanning holographic aberration probing (F-SHARP). *Nat. Photon.* **11**, 116–123 (2017).
- [36] May, M. A. *et al.* Fast holographic scattering compensation for deep tissue biological imaging. *Nat. Commun.* **12**, 4340 (2021).
- [37] Aizik, D. & Levin, A. Non-invasive and noise-robust light focusing using confocal wavefront shaping. Preprint at <https://arxiv.org/abs/2301.11421> (2023).
- [38] Xu, X., Liu, H. & Wang, L. V. Time-reversed ultrasonically encoded optical focusing into scattering media. *Nat. Photon.* **5**, 154–157 (2011).
- [39] Wang, Y. M., Judkewitz, B., DiMarzio, C. A. & Yang, C. Deep-tissue focal fluorescence imaging with digitally time-reversed ultrasound-encoded light. *Nat. Commun.* **3**, 928 (2012).
- [40] Ma, C., Xu, X., Liu, Y. & Wang, L. V. Time-reversed adapted-perturbation (TRAP) optical focusing onto dynamic objects inside scattering media. *Nat. Photon.* **8**, 931–936 (2014).
- [41] Zhou, E. H., Ruan, H., Yang, C. & Judkewitz, B. Focusing on moving targets through scattering samples. *Optica* **1**, 227–232 (2014).
- [42] Judkewitz, B., Horstmeyer, R., Vellekoop, I. M., Papadopoulos, I. N. & Yang, C. Translation correlations in anisotropically scattering media. *Nat. Phys.* **11**, 684–689 (2015).
- [43] Osnabrugge, G., Horstmeyer, R., Papadopoulos, I. N., Judkewitz, B. & Vellekoop, I. M. Generalized optical memory effect. *Optica* **4**, 886–892 (2017).
- [44] Bertolotti, J. *et al.* Non-invasive imaging through opaque scattering layers. *Nature* **491**, 232–234 (2012).
- [45] Katz, O., Heidmann, P., Fink, M. & Gigan, S. Non-invasive single-shot imaging through scattering layers and around corners via speckle correlations. *Nat. Photon.* **8**, 784–790 (2014).
- [46] Yeminy, T. & Katz, O. Guidestar-free image-guided wavefront shaping. *Sci. Adv.* **7**, eabf5364 (2021).
- [47] Feng, B. Y. *et al.* NeuWS: Neural wavefront shaping for guidestar-free imaging through static and dynamic scattering media. *Sci. Adv.* **9**, eadg4671 (2023).
- [48] Haim, O., Boger-Lombard, J. & Katz, O. Image-guided computational holographic wavefront shaping. Preprint

- at <https://arxiv.org/abs/2305.12232> (2023).
- [49] Weinberg, G., Sunray, E. & Katz, O. Noninvasive megapixel fluorescence microscopy through scattering layers by a virtual reflection-matrix. Preprint at <https://arxiv.org/abs/2312.16065> (2023).
- [50] Kang, S. *et al.* Imaging deep within a scattering medium using collective accumulation of single-scattered waves. *Nat. Photon.* **9**, 253–258 (2015).
- [51] Badon, A. *et al.* Smart optical coherence tomography for ultra-deep imaging through highly scattering media. *Sci. Adv.* **2**, e1600370 (2016).
- [52] Badon, A. *et al.* Distortion matrix concept for deep optical imaging in scattering media. *Sci. Adv.* **6**, eaay7170 (2020).
- [53] Kang, S. *et al.* High-resolution adaptive optical imaging within thick scattering media using closed-loop accumulation of single scattering. *Nat. Commun.* **8**, 2157 (2017).
- [54] Yoon, S., Lee, H., Hong, J. H., Lim, Y.-S. & Choi, W. Laser scanning reflection-matrix microscopy for aberration-free imaging through intact mouse skull. *Nat. Commun.* **11**, 5721 (2020).
- [55] Kwon, Y. *et al.* Computational conjugate adaptive optics microscopy for longitudinal through-skull imaging of cortical myelin. *Nat. Commun.* **14**, 105 (2023).
- [56] Li, B. *et al.* Efficient framework of solving time-gated reflection matrix for imaging through turbid medium. *Opt. Express* **31**, 15461–15473 (2023).
- [57] Najar, U. *et al.* Non-invasive retrieval of the time-gated transmission matrix for optical imaging deep inside a multiple scattering medium. Preprint at <https://arxiv.org/abs/2303.06119> (2023).
- [58] Lee, Y.-R., Kim, D.-Y., Jo, Y., Kim, M. & Choi, W. Exploiting volumetric wave correlation for enhanced depth imaging in scattering medium. *Nat. Commun.* **14**, 1878 (2023).
- [59] Popoff, S. M. *et al.* Measuring the transmission matrix in optics: an approach to the study and control of light propagation in disordered media. *Phys. Rev. Lett.* **104**, 100601 (2010).
- [60] Mounaix, M. *et al.* Spatiotemporal coherent control of light through a multiple scattering medium with the multispectral transmission matrix. *Phys. Rev. Lett.* **116**, 253901 (2016).
- [61] De Boer, J. F., Leitgeb, R. & Wojtkowski, M. Twenty-five years of optical coherence tomography: the paradigm shift in sensitivity and speed provided by Fourier domain OCT. *Biomed. Opt. Express* **8**, 3248–3280 (2017).
- [62] Barnett, A. H., Magland, J. & af Klinteberg, L. A parallel nonuniform fast Fourier transform library based on an “exponential of semicircle” kernel. *SIAM J. Sci. Comput.* **41**, C479–C504 (2019).
- [63] Bender, N. *et al.* Coherent enhancement of optical remission in diffusive media. *Proc. Natl. Acad. Sci. U.S.A.* **119**, e2207089119 (2022).
- [64] Wolf, E. Three-dimensional structure determination of semi-transparent objects from holographic data. *Opt. Commun.* **1**, 153–156 (1969).
- [65] Wojtkowski, M. *et al.* Ultrahigh-resolution, high-speed, Fourier domain optical coherence tomography and methods for dispersion compensation. *Opt. Express* **12**, 2404–2422 (2004).
- [66] Hell, S., Reiner, G., Cremer, C. & Stelzer, E. H. Aberrations in confocal fluorescence microscopy induced by mismatches in refractive index. *J. Microsc.* **169**, 391–405 (1993).
- [67] Muller, R. A. & Buffington, A. Real-time correction of atmospherically degraded telescope images through image sharpening. *J. Opt. Soc. Am.* **64**, 1200–1210 (1974).
- [68] Liu, D. C. & Nocedal, J. On the limited memory BFGS method for large scale optimization. *Math. Program.* **45**, 503–528 (1989).
- [69] Johnson, S. G. The NLOpt nonlinear-optimization package. <http://github.com/stevengj/nlopt>.
- [70] Noll, R. J. Zernike polynomials and atmospheric turbulence. *J. Opt. Soc. Am.* **66**, 207–211 (1976).
- [71] Verrier, N. & Atlan, M. Off-axis digital hologram reconstruction: some practical considerations. *Appl. Opt.* **50**, H136–H146 (2011).
- [72] Xiong, W., Hsu, C. W. & Cao, H. Long-range spatio-temporal correlations in multimode fibers for pulse delivery. *Nat. Commun.* **10**, 2973 (2019).
- [73] Kobat, D. *et al.* Deep tissue multiphoton microscopy using longer wavelength excitation. *Opt. Express* **17**, 13354–13364 (2009).
- [74] Van Beijnum, F., Van Putten, E. G., Lagendijk, A. & Mosk, A. P. Frequency bandwidth of light focused through turbid media. *Opt. Lett.* **36**, 373–375 (2011).
- [75] Krauze, W. *et al.* 3D scattering microphantom sample to assess quantitative accuracy in tomographic phase microscopy techniques. *Sci. Rep.* **12**, 19586 (2022).
- [76] Lin, H.-C., Wang, Z. & Hsu, C. W. Fast multi-source nanophotonic simulations using augmented partial factorization. *Nat. Comput. Sci.* **2**, 815–822 (2022).
- [77] Wang, Z., Zhang, Y. & Hsu, C. W. Full-wave simulations of tomographic optical imaging inside scattering media. Preprint at <https://arxiv.org/abs/2308.07244> (2023).
- [78] Liu, Y., Ma, C., Shen, Y., Shi, J. & Wang, L. V. Focusing light inside dynamic scattering media with millisecond digital optical phase conjugation. *Optica* **4**, 280–288 (2017).
- [79] Qureshi, M. M. *et al.* In vivo study of optical speckle decorrelation time across depths in the mouse brain. *Biomed. Opt. Express* **8**, 4855–4864 (2017).
- [80] Gao, L. & Smith, R. T. Optical hyperspectral imaging in microscopy and spectroscopy – a review of data acquisition. *J. Biophotonics* **8**, 441–456 (2015).
- [81] Rivenson, Y. *et al.* PhaseStain: the digital staining of label-free quantitative phase microscopy images using deep learning. *Light Sci. Appl.* **8**, 23 (2019).
- [82] Chen, X. *et al.* Artificial confocal microscopy for deep label-free imaging. *Nat. Photon.* **17**, 250–258 (2023).
- [83] Akkin, T., Davé, D. P., Milner, T. E. & Rylander III, H. G. Detection of neural activity using phase-sensitive optical low-coherence reflectometry. *Opt. Express* **12**, 2377–2386 (2004).
- [84] Kim, W., Kim, S., Huang, S., Oghalai, J. S. & Applegate, B. E. Picometer scale vibrometry in the human middle ear using a surgical microscope based optical coherence tomography and vibrometry system. *Biomed. Opt. Express* **10**, 4395–4410 (2019).
- [85] Zhang, Y. *et al.* Deep imaging inside scattering media through virtual spatiotemporal wavefront shaping. Preprint at <https://arxiv.org/abs/2306.08793> (2023).
- [86] Balondrade, P. *et al.* Multi-spectral reflection matrix for ultra-fast 3D label-free microscopy. Preprint at <https://arxiv.org/abs/2309.10951> (2023).
- [87] <https://doi.org/10.5281/zenodo.8231064>.
- [88] <https://github.com/complexphoton/SMTexperiment>.

CONTENTS

List of Figures	2
List of Tables	2
I. Measurement details	3
A. Optical setup	3
B. Control and automation	4
C. Off-axis holography	5
D. Data acquisition time	7
II. Characterization of raw data	7
A. Spectrum	7
B. Phase stability and noise	7
C. Sensitivity of SMT	8
III. Digital corrections and calibrations	9
A. Incident angle calibration	9
B. Reference plane and corrections for input aberrations and dispersion in the optical system	10
C. Correction for refractive index mismatch	10
1. Single-interface index mismatch	12
2. Double-interface index mismatch	13
D. Layer-thickness measurement and depth calibration	14
E. Compensation for sample dispersion	14
F. Input and output wavefront corrections	16
G. Metric landscape without the quadruple summation	21
H. Digital correction flowchart	23
I. Time usage and memory consumption	23
IV. Synthesis of RCM, OCT, OCM/CASS, CAO-OCM, and VRM images	23
A. RCM	23
B. OCT/OCM/CASS	23
C. CAO-OCM	25
D. Volumetric reflection-matrix microscopy (VRM)	26
1. VRM spectral dispersion compensation	26
2. VRM angular wavefront correction and reconstruction	29
V. SMT with fewer frequencies	31
VI. SMT with fewer incident angles	31
VII. Point spread function (PSF)	32
VIII. Sample preparation	33
IX. Resolution and depth of field of SMT	34
A. Theoretical axial resolution	34
B. Theoretical lateral resolution and depth of field	34
C. Experimental FWHM resolution	36
References	36

LIST OF FIGURES

1	Detailed experimental setup	3
2	Flow chart of the automated measurement	4
3	Complex field retrieval with off-axis holography	6
4	Angle-averaged reflection matrix spectra	7
5	Phase stability and noise	8
6	Sensitivity of SMT	9
7	Mirror reflection data	10
8	Correction for refractive index mismatches	11
9	Dispersion compensation for USAF target under tissue	15
10	Wavefront correction and progression	17
11	Evolution of the image quality metric during wavefront optimization	18
12	Large-angle wavefront correction	19
13	Volumetric dispersion compensation and wavefront correction	20
14	Effect of the quadruple summation on the image metric landscape.	21
15	Flowchart of SMT digital corrections and image construction.	22
16	CAO-OCM images of USAF target in air	26
17	CAO-OCM images of USAF target under tissue	26
18	VRM images with and without temporal truncation	29
19	SMT images with fewer frequencies	32
20	SMT images with fewer incident angles	33
21	Sample preparation	33
22	Theoretical lateral resolution, signal strength, and depth of field	35
23	Depth of field with expanded field of view	36
24	Experimental FWHM resolution of nanoparticle colloid	37

LIST OF TABLES

1	Time and memory usage of SMT digital correction and reconstruction	22
---	--	----

I. MEASUREMENT DETAILS

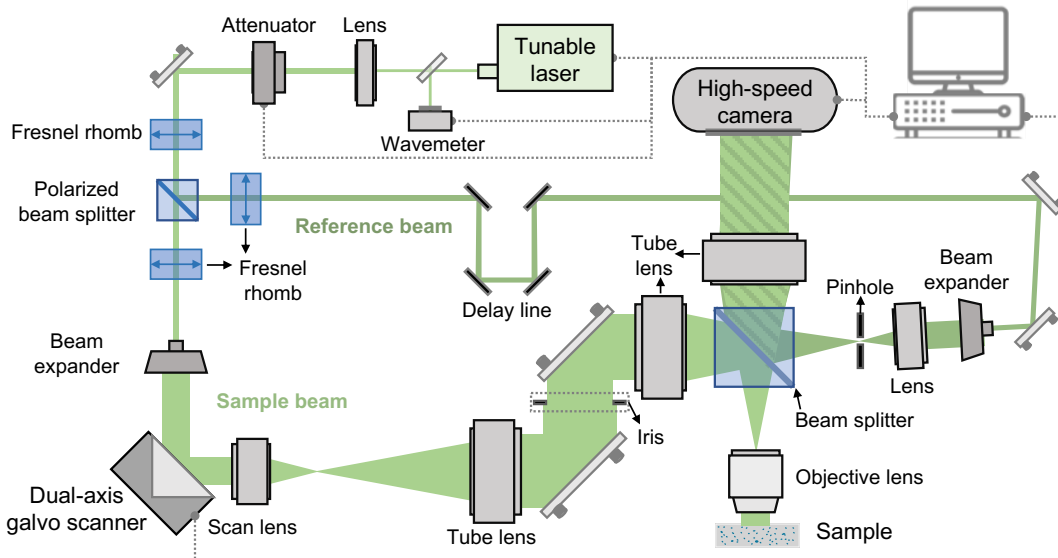
A. Optical setup

In this section, we describe the detailed experimental setup for measuring the hyperspectral reflection matrix (**Supplementary Fig. 1**). We use off-axis holography in the Mach-Zehnder configuration [1, 2] to measure the complex field information including amplitude and phase. The light source is generated by a tunable Ti:Sapphire laser (M Squared SolsTiS 1600) and is polarized, the frequency of which can be scanned and is monitored by a wavemeter (HighFinesse Wavemeter WS6-600). To balance the power at different frequencies, we use a motorized attenuator (Newport Motorized Variable Beam Splitter VA-CB-2-CONEX) to produce a frequency-dependent attenuation.

The laser beam is split into a sample beam and a reference beam through a polarized beam splitter (Newport Polarizing Cube Beamsplitter 05FC16PB.5). The sample beam is focused onto the back focal plane of an objective lens (Mitutoyo M Plan Apo NIR 100X) to create a plane-wave-like directional illumination onto the sample, with the reference plane being the focal plane of the objective lens. The angle of illumination is scanned by a dual-axis galvo scanner (ScannerMAX Saturn 5B). After the galvo scanner, we use a telecentric system composed of one scan lens (Thorlabs Scan Lens SL50-2P2) and two tube lenses (Thorlabs Tube Lens TTL200MP) to create a sharp focus on the back focal plane of the objective lens. Between the two tube lenses, there is a plane conjugate to the focal plane of the objective lens, where we place an iris diaphragm to control the illumination area on the sample. The scattered light from the sample is measured by a microscope imaging system composed of the objective lens, another tube lens (Thorlabs Tube Lens TTL200-S8), and a high-speed camera (Photron FASTCAM NOVA S6). The camera sensor is located on a plane that is also conjugate to the objective focal plane. When the objective lens focuses light on a mirror or a sample surface, the iris in the incidence path can be clearly imaged on the camera. The numerical aperture of the objective lens is $NA = 0.5$. With a magnification of 100X and a camera pixel size of $20\ \mu\text{m}$, the detection system provides a pixel resolution of $\delta x_{\text{pixel}} = 0.2\ \mu\text{m}$; this pixel resolution is smaller than the diffraction limit in order to resolve the interference fringes in off-axis holography (Supplementary Sect. I C). The camera sensor has a pixel count of 1024×1024 . In this work, we use a region of interest of 256×256 pixels, corresponding to a field of view (FOV) of $51.2 \times 51.2\ \mu\text{m}^2$.

By using plane-wave-like (unfocused) illumination in momentum space $\mathbf{k}_{\parallel}^{\text{in}}$, we avoid nonlinear response or photo-damage of the sample. By using a real-space detection $\mathbf{r}_{\parallel}^{\text{out}}$, we avoid localized saturation of the camera, allowing us to tune the power to optimize the signal-to-noise ratio.

The sample is mounted on a 3-axis (XYZ) translation stage, with a motorized actuator (Newport Motorized Actuator TRA6CC) for controlling and monitoring the z position of the sample. A separate camera (Edmund EO-0514) images the sample from the other side to facilitate selecting the region of interest in the sample. We use a switchable sample holder (Thorlabs Multi-Position Sliders ELL9K) to switch between samples and/or a mirror. For an accurate calibration of the incident angles (Supplementary Sect. III A), the mirror is placed perpendicular to the optical axis



Supplementary Fig. 1. Detailed experimental setup.

of the system. To this end, we first adjust the galvo scanner so that the part of the incident beam reflected by the back end of the objective lens follows the optical axis and reaches the center of the camera sensor. This indicates that the incident beam aligns with the optical axis and is focused at the center of the objective lens. Another portion of the beam passes through the objective lens and is reflected by the mirror. The camera captures the resulting interference between reflections from the objective lens and the mirror. When the mirror’s reflection deviates from the optical axis, interference manifests as a striped pattern. Adjustments are made to the mirror’s tilting angle to maximize interference fringe spacing, aligning the mirror reflection with the optical axis. When the mirror plane is perpendicular to the optical axis, the interference pattern transitions into concentric circles, characterized by a maximum fringe spacing.

The scattered light from the sample is combined with the reference beam at an angle to create interference patterns which are recorded by the camera (Supplementary Sect. IC). The reference beam arrives at the camera as a collimated beam, the size of which is matched with the sample beam size. To produce a clean and spatially uniform reference beam profile, we place a pinhole on the focal plane of the tube lens.

A delay line in the reference arm is used to match the optical path lengths of the two interfering beams. To set the delay, we first use a ruler to do a rough measurement of the optical path length difference ΔL between the two beams with an accuracy of a few centimeters. For finer tuning, we examine the reflection phase of a mirror measured by off-axis holography (Supplementary Sect. IC). The residual path length difference ΔL produces a linear frequency-dependent phase $e^{i(\omega/c)\Delta L}$ where c is the speed of light, which we measure with a fine frequency spacing (with the etalon scan mode of the laser).

The reflected sample beam and the reference beam are combined via a non-polarized beam splitter. Some incident light in the sample beam is internally reflected on the surfaces of the beam splitter and may enter the camera without arriving at the sample. To remove such unwanted signal, we slightly rotate the beam splitter by about 4 degrees to create a misalignment [3] so that internal reflections from its surfaces do not enter the camera sensor.

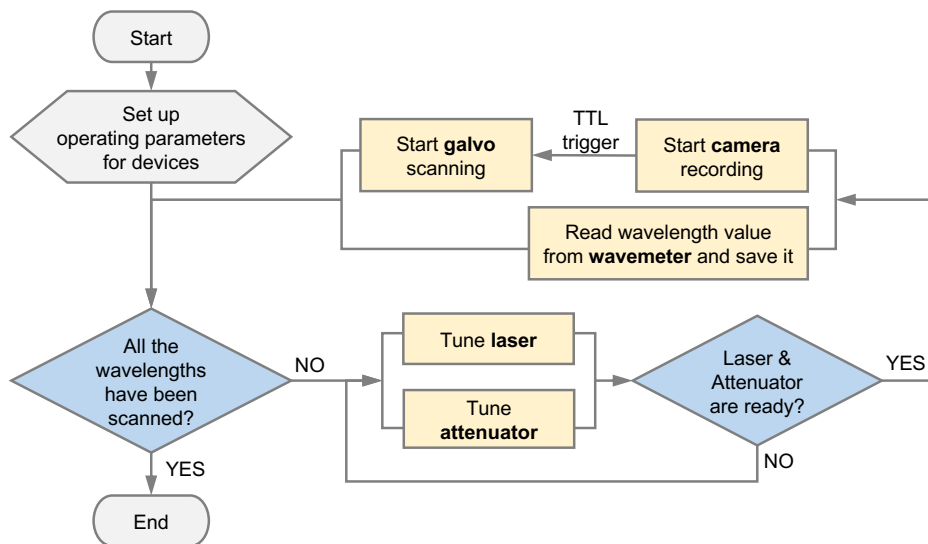
To balance the power between the two interfering beams, we adjust the Fresnel rhomb before the polarized beam splitter so that the reference beam intensity is comparable to the scattered light intensity from a piece of white paper.

The two Fresnel rhombs after the polarized beam splitter are used to control the polarization of the reflection matrix: the one on the sample beam adjusts the incident polarization, and the one on the reference beam adjusts the detected polarization. In this work, both polarization states are set to horizontal.

To improve the phase stability (characterized in Supplementary Sect. IIB), we enclose the setup to reduce air flow and to block acoustic noises. We control the setup remotely, which also avoids vibrations caused by onsite operations.

B. Control and automation

We automate the measurement with a LabVIEW program that controls the laser, attenuator, wavemeter, galvo scanner, and camera. The flow chart of this process is shown in **Supplementary Fig. 2**.



Supplementary Fig. 2. Flow chart of the automated measurement.

A while loop traverses all frequencies. In each iteration of the loop, we first tune the laser and the attenuator simultaneously. Currently, we scan the laser frequency by mechanically tuning a birefringent filter in a scan-and-stop mode. The filter position is set based on a lookup table, and we use the wavemeter to verify the actual output frequency (with an accuracy of 600 MHz). It is also possible to scan the birefringent filter continuously without stopping, in which case the laser output will jump between discrete frequencies with 0.286-THz spacing at a scanning rate of about 20 msec per frequency. Note that SMT adopts a non-uniform discrete Fourier transform, so it is not necessary to have the frequencies equally spaced.

The recorded image intensity can change substantially across frequencies due to frequency dependencies of the laser power and of the camera sensor efficiency. To maximize the signal-to-noise ratio, it is best to balance the measured intensity across frequencies such that the camera photon count is close to uniformly high but does not saturate the sensors. Therefore, we use an attenuator (Newport Motorized Variable Beam Splitter VA-CB-2-CONEX) to provide a frequency-dependent attenuation by rotating a half wave plate.

We operate the camera with a frame rate of 64,000 Hz and a region of interest of 256×256 pixels (corresponding to a FOV of $51.2 \times 51.2 \mu\text{m}^2$ on the sample). To avoid saturating the camera, we use an exposure time of $1/300,000$ second, smaller than the inverse frame rate. At each frequency, the camera records 5030 frames (corresponding to 5030 incident angles). The camera sends a TTL signal to trigger the galvo and start the angular scan, with a delay of less than 0.2 msec. To operate the dual-axis galvo scanner, we use a multi-function data acquisition device (DAQ) (Measurement Computing DAQ USB-1608GX-2AO). One analog input of the DAQ receives the trigger signal from the camera, and two analog outputs of the DAQ controls the operating voltages for the x and y scanner heads with a sample rate of 400,000 points per second. We use a triangular waveform for the fast x -axis scan and a step-shaped waveform with 80 steps for the slower y -axis scan, with a bidirectional raster pattern over a circular region in the angular space that is slightly larger than the back focal plane of the objective lens.

C. Off-axis holography

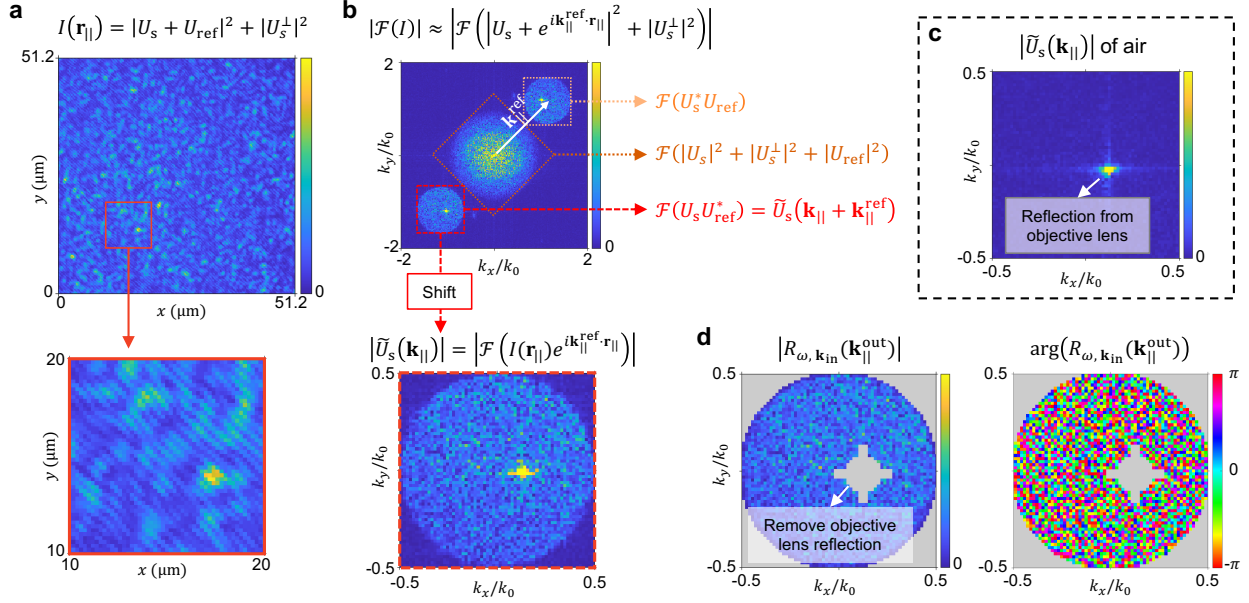
We use digital off-axis holography [1] to retrieve the complex-valued reflected fields of the sample beam, containing both amplitude and phase information. The interference pattern $I(\mathbf{r}_{\parallel})$ (\mathbf{r}_{\parallel} is the transverse position) recorded by the camera is a superposition of the reference beam $U_{\text{ref}}(\mathbf{r}_{\parallel})\hat{e}_{\text{ref}}$ in \hat{e}_{ref} polarization and the sample beam $U_s(\mathbf{r}_{\parallel})\hat{e}_{\text{ref}} + U_s^{\perp}(\mathbf{r}_{\parallel})\hat{e}_{\perp}$ which may contain both \hat{e}_{ref} and its orthogonal \hat{e}_{\perp} polarization. The reference beam is close to a plane wave propagating along \mathbf{k}_{ref} direction, so that $I(\mathbf{r}_{\parallel}) \approx \left| U_s(\mathbf{r}_{\parallel}) + e^{i\mathbf{k}_{\parallel}^{\text{ref}} \cdot \mathbf{r}_{\parallel}} \right|^2 + \left| U_s^{\perp}(\mathbf{r}_{\parallel}) \right|^2$. **Supplementary Fig. 3a** shows an example of $I(\mathbf{r}_{\parallel})$ with the sample being a piece of white paper; the interference fringes show up as the anti-diagonal stripes in the zoom-in. We take the 2D Fourier transform of $I(\mathbf{r}_{\parallel})$ with respect to $\mathbf{r}_{\parallel} = (x, y)$,

$$\begin{aligned} \mathcal{F}(I) &= \mathcal{F}\left(|U_s|^2 + |U_s^{\perp}|^2 + |U_{\text{ref}}|^2\right) + \mathcal{F}(U_s^*U_{\text{ref}}) + \mathcal{F}(U_sU_{\text{ref}}^*) \\ &\approx \mathcal{F}\left(|U_s|^2 + |U_s^{\perp}|^2 + |U_{\text{ref}}|^2\right) + \tilde{U}_s^*(\mathbf{k}_{\parallel} - \mathbf{k}_{\parallel}^{\text{ref}}) + \tilde{U}_s(\mathbf{k}_{\parallel} + \mathbf{k}_{\parallel}^{\text{ref}}), \end{aligned} \quad (\text{S1})$$

where $\mathbf{k}_{\parallel} = (k_x, k_y) = \mathbf{k}_{\parallel}^{\text{out}}$ is the in-plane components of the outgoing momentum. The first term of Eq. (S1) forms the zeroth-order signal. The latter two terms (which contain the complex field of the sample beam \tilde{U}_s in momentum space) form the $\pm 1^{\text{st}}$ -order signal and are shifted by $\pm \mathbf{k}_{\parallel}^{\text{ref}}$ in the \mathbf{k}_{\parallel} space. When $|\mathbf{k}_{\parallel}^{\text{ref}}|$ is sufficiently large, the $\pm 1^{\text{st}}$ -order signals will be separated from the zeroth-order signal in \mathbf{k}_{\parallel} space (upper figure of **Supplementary Fig. 3b**), and we can obtain \tilde{U}_s by truncating the -1^{st} -order signal and shifting it back to the center of the Fourier space.

An opaque medium generally scatters light toward all possible outgoing directions, so the sample field $\mathcal{F}(U_s)$ covers a disk with radius $k_0 \cdot \text{NA}$ in the momentum space (where $k_0 = 2\pi/\lambda$ and λ is the vacuum wavelength), limited only by the NA of the objective lens. Similarly, $\mathcal{F}\left(|U_s|^2 + |U_s^{\perp}|^2\right)$ covers a disk with radius $k_0 \cdot 2\text{NA}$ in the momentum space. To separate the zeroth-order and the $\pm 1^{\text{st}}$ -order terms, the angle of the reference beam must be large enough that $|\mathbf{k}_{\parallel}^{\text{ref}}| > k_0 \cdot 3\text{NA}$. An angle much larger than this threshold is not desirable since it makes the interference fringes narrower and harder to resolve. Specifically, the maximal $|k_x|$ and $|k_y|$ components of $\mathcal{F}(I)$ must be smaller than $\pi/\delta x_{\text{pixel}}$ to be resolved by pixel resolution δx_{pixel} . Here, we set $|\mathbf{k}_{\parallel}^{\text{ref}}| \approx 1.65k_0$ (corresponding to a reference beam angle of about 1° prior to the 100X magnification), while $3\text{NA} = 1.5$. To reduce the maximal $|k_x|$ and $|k_y|$, we use an azimuthal angle of $\angle \mathbf{k}_{\parallel}^{\text{ref}} \approx 45^\circ$. In this case, $\max|k_x| = k_0\text{NA} + |\mathbf{k}_{\parallel}^{\text{ref}}|/\sqrt{2}$.

From $\pi/\delta x_{\text{pixel}} > \max|k_x|$ and $|\mathbf{k}_{\parallel}^{\text{ref}}| > k_0 \cdot 3\text{NA}$, we get the largest pixel resolution one may use for off-axis holography is $\delta x_{\text{pixel}} < \lambda/[2(1 + \frac{3}{\sqrt{2}})\text{NA}] \approx \lambda/(6.24\text{NA})$.



Supplementary Fig. 3. Complex field retrieval with off-axis holography. **a.** The interference pattern $I(\mathbf{r}_{\parallel})$ formed by the scattered light from a piece of white paper $U_s \hat{e}_{\text{ref}} + U_s^{\perp} \hat{e}_{\perp}$ and the reference beam $U_{\text{ref}} \hat{e}_{\text{ref}}$. **b.** 2D Fourier spectrum $\mathcal{F}(I)$. There are three circular bright regions: the middle one contains the zeroth order and the other two are the $\pm 1^{\text{st}}$ orders, $\mathcal{F}(U_s^* U_{\text{ref}})$ and $\mathcal{F}(U_s U_{\text{ref}}^*)$. With a plane-wave-like reference beam $U_{\text{ref}}(\mathbf{r}_{\parallel}) \approx e^{i\mathbf{k}_{\parallel}^{\text{ref}} \cdot \mathbf{r}_{\parallel}}$, the minus one order is approximately the sample field \tilde{U}_s shifted by $-\mathbf{k}_{\parallel}^{\text{ref}}$. Thus, \tilde{U}_s can be obtained by shifting the minus one order back to the center of Fourier space. **c.** The retrieved field when the sample is removed (*i.e.*, measuring the reflection of air) shows a peak that comes from reflection by the objective lens. **d.** The retrieved complex scattered field from the sample. Data outside the NA range and near the objective lens reflection are excluded (gray regions).

A white-paper sample produces sufficient large-angle scattered light that the perimeter and the center of the $\pm 1^{\text{st}}$ -order terms can be accurately identified, from which we obtain $\mathbf{k}_{\parallel}^{\text{ref}}$. When using discrete Fourier transforms, the pixel size in momentum space is $\delta k = 2\pi/\text{FOV}$. To obtain a \tilde{U}_s centered at $\mathbf{k}_{\parallel}^{\text{out}} = 0$ without restriction of the discrete δk , we multiply $I(\mathbf{r})$ with $e^{i\mathbf{k}_{\parallel}^{\text{ref}} \cdot \mathbf{r}_{\parallel}}$ before taking the 2D discrete Fourier transform.

For the reflection matrix, we only keep data points of $\tilde{U}_s(\mathbf{k}_{\parallel}^{\text{out}})$ with $|\mathbf{k}_{\parallel}^{\text{out}}| < k_0 \cdot \text{NA}$. Within the NA range, the sample beam also includes unwanted reflected light from the objective lens. For an incident plane wave at direction \mathbf{k}_{in} , such objective lens reflection shows up mainly near $\mathbf{k}_{\parallel}^{\text{out}} = -\mathbf{k}_{\parallel}^{\text{in}}$ in Fourier space; we can clearly see it when we remove the sample (*i.e.*, measure air only) as shown in **Supplementary Fig. 3c**. For the reflection matrix data, we exclude $\mathbf{k}_{\parallel}^{\text{out}}$ near such objective lens reflection angles. We obtain the location of the objective lens reflection by searching for the maximum in the region near $\mathbf{k}_{\parallel}^{\text{out}} = -\mathbf{k}_{\parallel}^{\text{in}}$. Such objective lens reflection signal spreads more in the Fourier space when the incident angle is closer to normal incidence, so we also exclude more $\mathbf{k}_{\parallel}^{\text{out}}$ there. Note that such exclusion does not fully remove the reflection from objective lens; the residual objective lens reflection is currently the main limiting factor on the sensitivity of our detection (Supplementary Sect. II C). **Supplementary Fig. 3d** shows the amplitude and phase of $\tilde{U}_s(\mathbf{k}_{\parallel}^{\text{out}})$, with the excluded data points shown in gray.

This $\tilde{U}_s(\mathbf{k}_{\parallel}^{\text{out}}) = R(\mathbf{k}_{\parallel}^{\text{out}}, \mathbf{k}_{\parallel}^{\text{in}}, \omega)$ forms one column of the hyperspectral reflection matrix. Note that $|R(\mathbf{k}_{\parallel}^{\text{out}}, \mathbf{k}_{\parallel}^{\text{in}}, \omega)|^2$ is proportional to the detected power but not the reflected power since the camera sensor efficiency varies with the wavelength. The incident power also varies with both the wavelength and the incident angle. We do not normalize $R(\mathbf{k}_{\parallel}^{\text{out}}, \mathbf{k}_{\parallel}^{\text{in}}, \omega)$ by the incident power and sensor efficiency since doing so increases both noise and acquisition time.

Because we scan incident angles across a range that is slightly larger than the NA of the objective lens (Supplementary Sect. I B), some incident angles do not go through the objective lens. To exclude such incident angles, we exclude inputs where the mirror reflection does not show a strong peak. We also exclude the first 10 inputs at each wavelength where the galvo scanning has not yet started.

After the above exclusions, the number of input angles averages to around 3900 (ranging between 3830 to 3900 at different frequencies), and the number of output angles averages to around 2900 (ranging between 2210 to 3590). Note that the incident angles are slightly over-sampled, with spacing finer than $2\pi/\text{FOV}$.

D. Data acquisition time

It takes 180 seconds to complete the data acquisition across the 250 frequencies \times 5030 input angles for the USAF target under tissue sample, with data captured at a resolution of 256×256 pixels for each incident angle. This speed is sufficient since the phase drift in the system (Supplementary Sect. IIB) is only $\pi/8$ radian per minute and can be removed during dispersion compensation. The angular scan (running at the camera frame rate of 64 kHz; Supplementary Sect. IB) took 79 msec per frequency, totaling 20 seconds for the 250 frequencies. The remaining 160 seconds are used for the laser frequency tuning. To simplify the control, we currently separate the frequency scan and the angular scan: the camera recording starts only after the laser and the attenuator report back as having completed their tuning, and the next frequency tuning starts only after the previous angular scan completes. The birefringent filter used for the frequency tuning needs to accelerate and decelerate for every frequency requested, which contributes to most of the overall measurement time.

As mentioned in Supplementary Sect. IIB, one can also continuously scan the birefringent filter without stopping, which results in the laser output jumping between discrete frequencies with 0.286-THz spacing at a scan rate of 20 msec per frequency. If one has a camera that operates at 250 kHz frame rate (*e.g.*, Phantom TMX-5010 with 640×320 pixels [4]) and scans the camera, galvo, and laser concurrently, the data acquisition across the 250 frequencies \times 5030 input angles can complete in 5 seconds.

II. CHARACTERIZATION OF RAW DATA

A. Spectrum

From the measured hyperspectral reflection matrix $R(\mathbf{k}_{\parallel}^{\text{out}}, \mathbf{k}_{\parallel}^{\text{in}}, \omega)$, we calculate the angle-averaged detected power as a function of the wavelength,

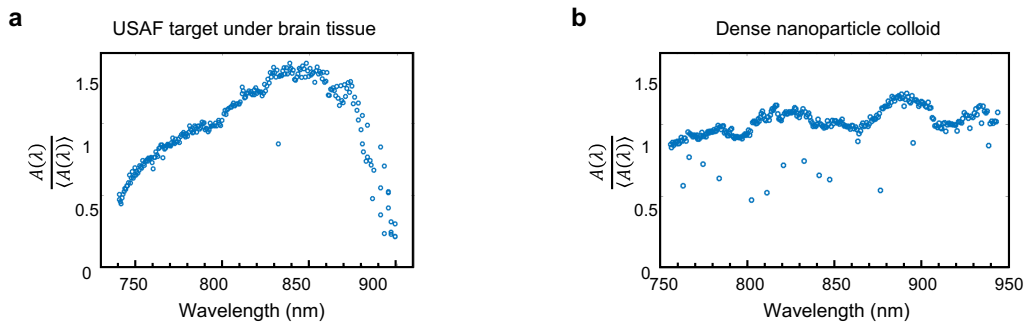
$$A(\lambda) = \sqrt{\frac{1}{N_{\text{in}} N_{\text{out}}} \sum_{\mathbf{k}_{\parallel}^{\text{in}}, \mathbf{k}_{\parallel}^{\text{out}}} \left| R\left(\mathbf{k}_{\parallel}^{\text{out}}, \mathbf{k}_{\parallel}^{\text{in}}, \omega = \frac{2\pi}{\lambda}\right) \right|^2}. \quad (\text{S2})$$

Supplementary Fig. 4 shows the normalized $A(\lambda)$ for the USAF target under mouse brain tissue and the dense nanoparticle colloid studied in this work. The former was measured at 247 frequencies with λ from 741 nm to 899 nm, and the latter was measured at 275 frequencies from 756 nm to 943 nm. Both were measured with a frequency spacing of $\delta f = 0.286$ THz. The two spectra differ because the laser output changes between the two measurements.

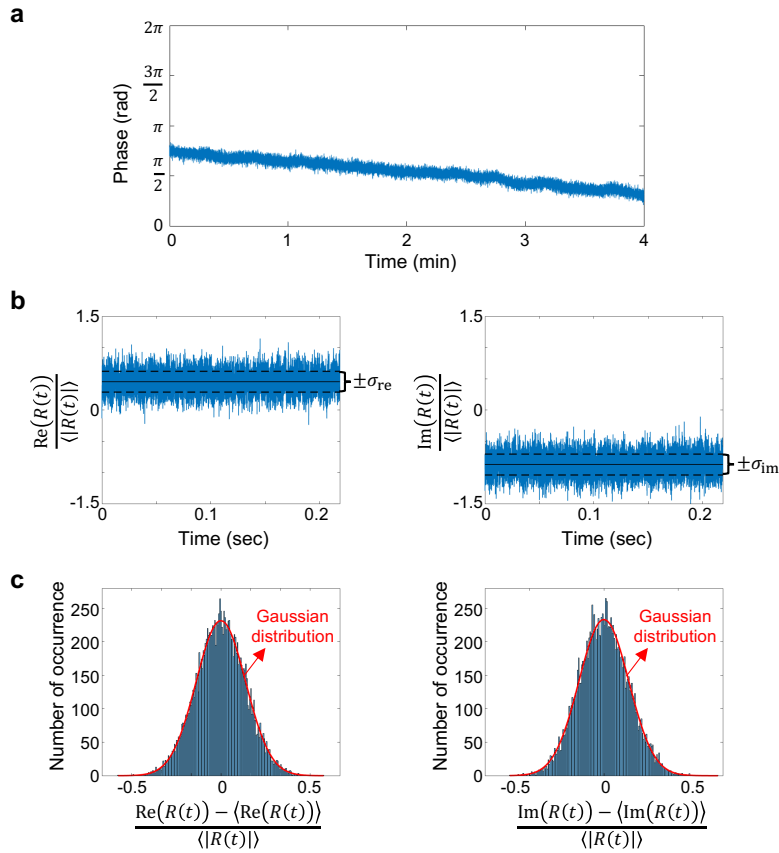
The power incident on the sample, measured with a power meter at the sample position, ranges from 0.02 mW and 0.2 mW depending on the wavelength.

B. Phase stability and noise

To evaluate the phase stability, we monitor how the measured reflection phase of a mirror changes over time (**Supplementary Fig. 5a**). In the short term, the phase fluctuates with a standard deviation of 0.09 radian. In the long term, the phase drifts slowly at a pace of about $\pi/8$ radian per minute, likely due to temperature change.



Supplementary Fig. 4. Angle-averaged reflection matrix spectra given by Eq. (S2).



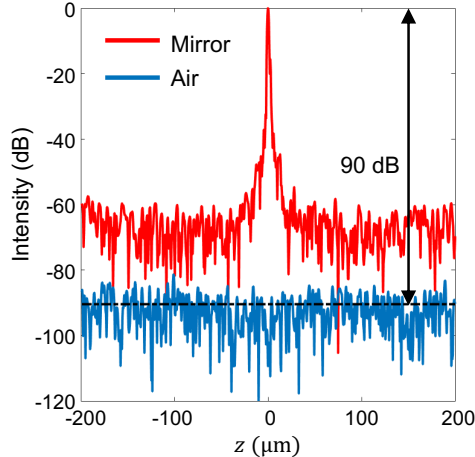
Supplementary Fig. 5. Phase stability and noise. **a.** Long-term evolution of the measured reflection phase of a static mirror, with $x = y = 25 \mu\text{m}$. **b.** Measured reflected field from a static white-paper sample at $\mathbf{k}_{\parallel} = (-0.28k_0, -0.24k_0)$. **c.** Histogram of the measured field in **b**, showing a Gaussian distribution.

To quantify the noise, we examine the short-term fluctuations of the reflected fields from a white-paper sample (**Supplementary Fig. 5b**). These short-term fluctuations come from a combination of vibrations, air flow, dither noise in the galvo scanner, dark current and read noise and photon shot noise at the camera sensor, and phase and amplitude noise from the laser. Both the real part and the imaginary part follow a Gaussian distribution (**Supplementary Fig. 5c**). The averaged standard deviation, $\frac{1}{N_{\text{out}}} \sum_{\text{out}} \frac{1}{2}(\sigma_{\text{real}} + \sigma_{\text{imaginary}})$, is around 1% of the averaged amplitude $\sqrt{\frac{1}{N_{\text{out}}} \sum_{\text{out}} \langle |R|^2 \rangle}$. Note that this is the noise per element of the reflection matrix. The SMT image is built by summing over many (around two billion in our experiment) matrix elements, after which the signal-to-noise ratio (SNR) is boosted significantly. We quantify the SNR of the SMT image in the next section.

C. Sensitivity of SMT

The sensitivity is defined as one over the smallest reflectivity at which $\text{SNR} = 1$. It is common to assume the SNR to be proportional to the sample reflectivity, under which the sensitivity equals the SNR when the sample is a mirror with unity reflectivity; we use this approach here. We take three hyperspectral reflection matrix measurements under the same condition: the first two are performed for two different mirror samples and the third one is performed for air with no sample. We use the first mirror measurement to correct for the dispersion and aberrations in the optical system (Supplementary Sect. III B) and perform SMT reconstructions using each of the three data sets to obtain a self-corrected mirror image $I_{\text{SMT}}^{\text{mirror, self}}$, a cross-corrected mirror image $I_{\text{SMT}}^{\text{mirror, cross}}$, and an air image $I_{\text{SMT}}^{\text{air}}$. Comparing the peak of $I_{\text{SMT}}^{\text{mirror, cross}}$ and the average of $I_{\text{SMT}}^{\text{air}}$, we find the sensitivity to be 90 dB (**Supplementary Fig. 6**).

The SMT sensitivity may be limited by both measurement noises (as characterized in the previous section) and the residual reflection from the objective lens. In the self-corrected mirror image, most of the phase noises are removed during the correction stage to yield a constant phase, so $I_{\text{SMT}}^{\text{mirror, self}}$ provides an estimate of the would-be peak intensity



Supplementary Fig. 6. Sensitivity of SMT. Normalized axial intensity of SMT images of a mirror with cross-correction $I_{\text{SMT}}^{\text{mirror,cross}}$ and of air $I_{\text{SMT}}^{\text{air}}$. The intensities are evaluated at the center of the FOV, at $x = y = 25 \mu\text{m}$. The peak of $I_{\text{SMT}}^{\text{mirror,cross}}$ is 90 dB higher than the averaged air intensity (which comes primarily from the residual reflection of the objective lens).

in the absence of noises. We find the peak of $I_{\text{SMT}}^{\text{mirror,self}}$ to be 2.5 dB higher than that of $I_{\text{SMT}}^{\text{mirror,cross}}$, indicating that noises misalign the phases to reduce the SMT signal by roughly a factor of 2.

If reflection matrix data with \mathbf{k}_{\parallel} near the peak of the objective lens reflection signal is not excluded (Supplementary Sect. IC), $I_{\text{SMT}}^{\text{air}}$ would be 12 dB higher, showing the importance of such exclusion. However, such exclusion does not fully remove the objective’s reflection because the signal from the objective’s reflection also exists at other \mathbf{k}_{\parallel} points; several factors contribute: the incident beam does not form a point focus on the back focal plane of the objective lens due to aberrations of the optical system and the laser beam profile, and reflection from the objective lens can come from multiple interfaces beyond the back focal plane. In the absence of noise and the objective’s reflection, $I_{\text{SMT}}^{\text{air}}$ would be zero. Therefore, to estimate the contribution of the residual objective lens reflection, we perform a fourth reflection matrix measurement with the laser turned off, which fully removes the objective’s reflection while preserving the camera’s dark current and read noise. The resulting laser-off SMT image is 9 dB lower than $I_{\text{SMT}}^{\text{air}}$. This indicates that the residual reflection from the objective lens contributes more to our SMT sensitivity than noises do. In our current measurement, the objective lens reflection shows up as a coherent background because the coherence length of our tunable CW laser is far greater than the path difference between the objective lens and the sample. If a sensitivity much larger than 90 dB is necessary, one may reduce the coherence length of the laser and/or clean the incident beam to make the objective-lens-reflection exclusion more complete.

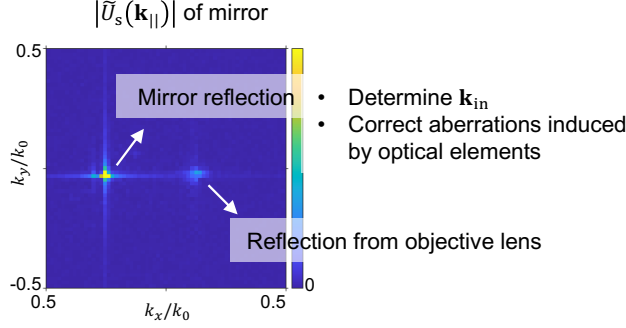
III. DIGITAL CORRECTIONS AND CALIBRATIONS

A. Incident angle calibration

In addition to the sample of interest, we also measure the hyperspectral reflection matrix of a mirror (Thorlabs Protected Silver Mirror PF10-03-P01). The specular reflection from the mirror produces a strong peak in Fourier space (**Supplementary Fig. 7**) located at $\mathbf{k}_{\parallel}^{\text{out}} = \mathbf{k}_{\parallel}^{\text{in}}$, which we use to calibrate the incident angle $\mathbf{k}_{\parallel}^{\text{in}}$.

We also use the mirror data to determine the precise location of the reflection from the objective lens in the momentum space (the weaker peak in **Supplementary Fig. 7**) so we can exclude data points at those $\mathbf{k}_{\parallel}^{\text{out}}$ from our sample reflection matrix as described in Supplementary Sect. IC.

After such calibration, the input momentum and the output momentum of the reflection matrix both lie on the same grid points with spacing $\delta k = 2\pi/\text{FOV}$ (Supplementary Sect. IC), for all frequencies. But the number of inputs and the number of outputs both depend on the frequency. Recall that the incident angles are slightly over-sampled (Supplementary Sect. IC), so some incident angles share the same mirror-reflection peak location. For the convenience of further processing, we average over data points with the same $\mathbf{k}_{\parallel}^{\text{in}}$ and pad zeros at the excluded $\mathbf{k}_{\parallel}^{\text{out}}$ and at large $\mathbf{k}_{\parallel}^{\text{in/out}}$ such that the size of matrix $R(\mathbf{k}_{\parallel}^{\text{out}}, \mathbf{k}_{\parallel}^{\text{in}}, \omega)$ is 3761 x 3761 at all frequencies and that all frequencies share the same list of $\mathbf{k}_{\parallel}^{\text{in}}$ (which equals the list of $\mathbf{k}_{\parallel}^{\text{out}}$).



Supplementary Fig. 7. Mirror reflection data. The specular mirror reflection gives a strong peak in Fourier space located at $\mathbf{k}_{\parallel} = \mathbf{k}_{\parallel}^{\text{in}}$. Subtracting the peak phase from the sample reflection matrix corrects the dispersion and most of the input aberrations in the optical system. The reflection from the objective lens shows up as a much weaker peak than the mirror peak.

B. Reference plane and corrections for input aberrations and dispersion in the optical system

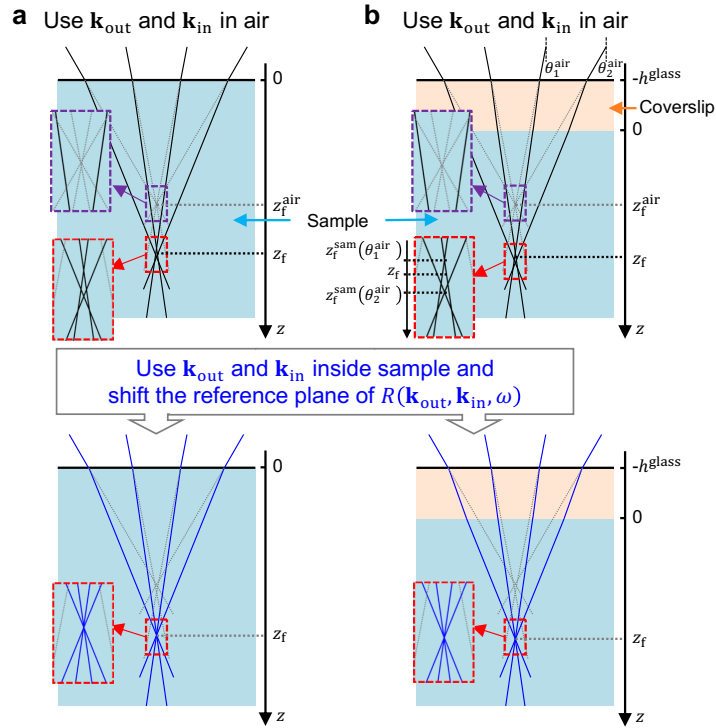
With the off-axis holography (Supplementary Sect. IC), the reflection matrix is associated with outgoing plane waves in air, $e^{i\mathbf{k}_{\text{out}}^{\text{air}} \cdot (\mathbf{r} - \mathbf{r}_{\text{ref}}^{\text{air}})}$, such that different $\mathbf{k}_{\text{out}}^{\text{air}}$ share the same reference point $\mathbf{r}_{\text{ref}}^{\text{air}} = (0, 0, z_{\text{ref}}^{\text{air}})$ with $z_{\text{ref}}^{\text{air}}$ being the focal plane of the objective lens in air. It will be convenient if the incident plane waves also have the same reference plane, $e^{i\mathbf{k}_{\text{in}}^{\text{air}} \cdot (\mathbf{r} - \mathbf{r}_{\text{ref}}^{\text{air}})}$. However, the galvo scanning introduces an additional propagation phase shift $\Delta\phi_{\text{scan}}(\mathbf{k}_{\parallel}^{\text{in}}, \omega)$ that varies with the incident angle $\mathbf{k}_{\parallel}^{\text{in}}$ and frequency ω . Since the reflection matrix of the sample and that of the mirror share the same $\Delta\phi_{\text{scan}}(\mathbf{k}_{\parallel}^{\text{in}}, \omega)$, we record the phase $\phi_{\text{mirror}}(\mathbf{k}_{\parallel}^{\text{in}}, \omega) \equiv \arg \left[R_{\text{mirror}}(\mathbf{k}_{\parallel}^{\text{out}} = \mathbf{k}_{\parallel}^{\text{in}}, \mathbf{k}_{\parallel}^{\text{in}}, \omega) \right]$ at the specular reflection peak $\mathbf{k}_{\parallel}^{\text{out}} = \mathbf{k}_{\parallel}^{\text{in}}$ of the mirror reflection matrix, and subtract $\phi_{\text{mirror}}(\mathbf{k}_{\parallel}^{\text{in}}, \omega)$ from the phase of the sample reflection matrix for all $\mathbf{k}_{\parallel}^{\text{in}}$ and all ω . Hereafter, we use $R'(\mathbf{k}_{\parallel}^{\text{out}}, \mathbf{k}_{\parallel}^{\text{in}}, \omega)$ to denote the sample reflection matrix after this subtraction. This $R'(\mathbf{k}_{\parallel}^{\text{out}}, \mathbf{k}_{\parallel}^{\text{in}}, \omega)$ has its input reference plane and output reference plane both at the focal plane of the objective lens, which equals the z position of the calibration mirror, $z_{\text{ref}}^{\text{air}} = z_{\text{mirror}}$.

In addition to the propagation phase shift $\Delta\phi_{\text{scan}}(\mathbf{k}_{\parallel}^{\text{in}}, \omega)$ from galvo scanning, the mirror reflection matrix also contains the aberrations and dispersion in the input path $\Delta\phi_{\text{in}}^{\text{sys}}(\mathbf{k}_{\parallel}^{\text{in}}, \omega)$ and those in the output path $\Delta\phi_{\text{out}}^{\text{sys}}(\mathbf{k}_{\parallel}^{\text{out}}, \omega)$. Therefore, $\phi_{\text{mirror}}(\mathbf{k}_{\parallel}^{\text{in}}, \omega) = \Delta\phi_{\text{scan}}(\mathbf{k}_{\parallel}^{\text{in}}, \omega) + \Delta\phi_{\text{in}}^{\text{sys}}(\mathbf{k}_{\parallel}^{\text{in}}, \omega) + \Delta\phi_{\text{out}}^{\text{sys}}(\mathbf{k}_{\parallel}^{\text{out}} = \mathbf{k}_{\parallel}^{\text{in}}, \omega)$. When we subtract $\phi_{\text{mirror}}(\mathbf{k}_{\parallel}^{\text{in}}, \omega)$ from the phase of the sample reflection matrix, we not only remove $\Delta\phi_{\text{scan}}(\mathbf{k}_{\parallel}^{\text{in}}, \omega)$; we also correct for the aberrations and dispersion in the input path $\Delta\phi_{\text{in}}^{\text{sys}}(\mathbf{k}_{\parallel}^{\text{in}}, \omega)$. However, $\Delta\phi_{\text{out}}^{\text{sys}}(\mathbf{k}_{\parallel}^{\text{out}}, \omega)$ got subtracted along the input angles $\mathbf{k}_{\parallel}^{\text{in}}$ instead of along the output angles $\mathbf{k}_{\parallel}^{\text{out}}$. Therefore, the phase of the calibrated reflection matrix $\arg \left[R'(\mathbf{k}_{\parallel}^{\text{out}}, \mathbf{k}_{\parallel}^{\text{in}}, \omega) \right]$ still contains aberrations and dispersion in the output path in the form of $\Delta\phi_{\text{out}}^{\text{sys}}(\mathbf{k}_{\parallel}^{\text{out}}, \omega) - \Delta\phi_{\text{out}}^{\text{sys}}(\mathbf{k}_{\parallel}^{\text{out}} = \mathbf{k}_{\parallel}^{\text{in}}, \omega)$.

C. Correction for refractive index mismatch

The objective lens provides a sharp focus only in the designed background medium. Dry lenses designed to operate in air without an immersion liquid are the most commonly available and the most convenient to use. But because of refraction, dry lenses focus poorly inside media with other refractive indices such as water. As illustrated in **Supplementary Fig. 8a**, a perfect focus to $(x_f, y_f, z_f^{\text{air}})$ in air gets diffracted to an imperfect focus at (x_f, y_f, z_f) . The focus becomes poorer at deeper depths, and the situation is even more severe when a coverslip is used (**Supplementary Fig. 8b**). Correction for such degradation typically requires expensive specially designed objective lenses or additional hardware like spatial light modulators. In SMT, we correct for it digitally.

In the presence of refractive index mismatches, Eqs. (1–2) of the main text continue to hold, but we need to be careful in specifying the reference planes of the reflection matrix, the momenta $\mathbf{k}_{\text{in/out}}$, and the relative coordinates. To find the correct formalism, we start with a generalized framework. The incident and the outgoing waves are still



Supplementary Fig. 8. Correction for refractive index mismatches. **a.** A system with a single air-sample interface. When a dry objective lens is used, incident light from different angles can focus in air but do not focus well inside the medium due to refraction at the air-sample interface. **b.** A sample covered by a coverslip with thickness h^{glass} , where there is an air-glass interface and another glass-sample interface. When light is focused to z_f^{air} in air, the focal plane in the sample z_f^{sam} varies with the incident angle θ^{air} , leading to an elongated focus at z_f . SMT corrects the refractive index mismatches by converting the input/output momenta from those in the air to those in the sample medium and shifting the reference plane of the reflection matrix to the sample surface at $z = 0$, as in Eqs. (S13), (S18).

written as superpositions of plane waves

$$E_{\text{in}}(\mathbf{r}, t) = \sum_{\mathbf{k}_{\parallel}^{\text{in}}, \omega} \tilde{E}_{\text{in}}(\mathbf{k}_{\parallel}^{\text{in}}, \omega) u_{\text{in}}(\mathbf{r}; \mathbf{k}_{\parallel}^{\text{in}}, \omega) e^{-i\omega t}, \quad (\text{S3})$$

$$E_{\text{out}}(\mathbf{r}, t) = \sum_{\mathbf{k}_{\parallel}^{\text{out}}, \omega} \tilde{E}_{\text{out}}(\mathbf{k}_{\parallel}^{\text{out}}, \omega) u_{\text{out}}(\mathbf{r}; \mathbf{k}_{\parallel}^{\text{out}}, \omega) e^{-i\omega t}, \quad (\text{S4})$$

with the reflection matrix R' relating the amplitudes

$$\tilde{E}_{\text{out}}(\mathbf{k}_{\parallel}^{\text{out}}, \omega) = \sum_{\mathbf{k}_{\parallel}^{\text{in}}} R'(\mathbf{k}_{\parallel}^{\text{out}}, \mathbf{k}_{\parallel}^{\text{in}}, \omega) \tilde{E}_{\text{in}}(\mathbf{k}_{\parallel}^{\text{in}}, \omega). \quad (\text{S5})$$

The $R'(\mathbf{k}_{\parallel}^{\text{out}}, \mathbf{k}_{\parallel}^{\text{in}}, \omega)$ here has its input reference plane and output reference plane both at the z position of the calibration mirror, as described in Supplementary Sect. III B above. The measurements here use a dry objective lens, so these reference planes are with respect to the would-be propagation of the incident and reflected waves in air. We denote such “in-air reference plane” by $z_{\text{ref}}^{\text{air}} = z_{\text{mirror}}$ and the in-air reference point by $\mathbf{r}_{\text{ref}}^{\text{air}} = (0, 0, z_{\text{ref}}^{\text{air}})$. The plane wave profiles $u_{\text{in}}(\mathbf{r}; \mathbf{k}_{\parallel}^{\text{in}}, \omega)$ and $u_{\text{out}}(\mathbf{r}; \mathbf{k}_{\parallel}^{\text{out}}, \omega)$ include refraction at interfaces, and their relative phases are chosen such that their in-air reference point is at $\mathbf{r}_{\text{ref}}^{\text{air}}$.

When there is no interface and when $z_{\text{mirror}} = 0$, we have $\mathbf{r}_{\text{ref}}^{\text{air}} = \mathbf{0}$, $u_{\text{in}}(\mathbf{r}; \mathbf{k}_{\parallel}^{\text{in}}, \omega) = e^{i\mathbf{k}_{\text{in}} \cdot \mathbf{r}}$, $u_{\text{out}}(\mathbf{r}; \mathbf{k}_{\parallel}^{\text{out}}, \omega) = e^{i\mathbf{k}_{\text{out}} \cdot \mathbf{r}}$, with $\mathbf{k}_{\text{in}} = (\mathbf{k}_{\parallel}^{\text{in}}, \sqrt{(\omega/c)^2 - |\mathbf{k}_{\parallel}^{\text{in}}|^2})$ and $\mathbf{k}_{\text{out}} = (\mathbf{k}_{\parallel}^{\text{out}}, -\sqrt{(\omega/c)^2 - |\mathbf{k}_{\parallel}^{\text{out}}|^2})$, and we directly obtain Eqs. (1–2) of the main text with $R = R'$.

When there are interfaces, we need more careful definitions for \mathbf{k}_{in} , \mathbf{k}_{out} , and R , as we describe below.

1. Single-interface index mismatch

Consider a single air-sample interface at $z = 0$ (**Supplementary Fig. 8a**) with refractive indices $n_{\text{air}} = 1$ and n_{sam} . Here,

$$u_{\text{in}}(\mathbf{r}; \mathbf{k}_{\parallel}^{\text{in}}, \omega) = \begin{cases} e^{i\mathbf{k}_{\text{in}}^{\text{air}} \cdot (\mathbf{r} - \mathbf{r}_{\text{ref}}^{\text{air}})}, & z \leq 0 \\ e^{i(\mathbf{k}_{\text{in}}^{\text{sam}} \cdot \mathbf{r} - k_{z,\text{in}}^{\text{air}} z_{\text{ref}}^{\text{air}})}, & z > 0 \end{cases} \quad (\text{S6})$$

with $k_{z,\text{in}}^{\text{air}} = \sqrt{(\omega/c)^2 - |\mathbf{k}_{\parallel}^{\text{in}}|^2}$, $k_{z,\text{in}}^{\text{sam}} = \sqrt{(n_{\text{sam}}\omega/c)^2 - |\mathbf{k}_{\parallel}^{\text{in}}|^2}$, $\mathbf{k}_{\text{in}}^{\text{air}} = (\mathbf{k}_{\parallel}^{\text{in}}, k_{z,\text{in}}^{\text{air}})$, and $\mathbf{k}_{\text{in}}^{\text{sam}} = (\mathbf{k}_{\parallel}^{\text{in}}, k_{z,\text{in}}^{\text{sam}})$. Eq. (S6) ensures that the in-air reference point is placed at $\mathbf{r} = \mathbf{r}_{\text{ref}}^{\text{air}}$ and that $u_{\text{in}}(\mathbf{r}; \mathbf{k}_{\parallel}^{\text{in}}, \omega)$ is continuous across the air-sample interface at $z = 0$. Since we are not interested in imaging the interface, we ignore the interface reflection at $z = 0$ and the resulting amplitude change (*i.e.*, Fresnel coefficients) in u_{in} . Similarly,

$$u_{\text{out}}(\mathbf{r}; \mathbf{k}_{\parallel}^{\text{out}}, \omega) = \begin{cases} e^{i\mathbf{k}_{\text{out}}^{\text{air}} \cdot (\mathbf{r} - \mathbf{r}_{\text{ref}}^{\text{air}})}, & z \leq 0 \\ e^{i(\mathbf{k}_{\text{out}}^{\text{sam}} \cdot \mathbf{r} - k_{z,\text{out}}^{\text{air}} z_{\text{ref}}^{\text{air}})}, & z > 0 \end{cases} \quad (\text{S7})$$

with $k_{z,\text{out}}^{\text{air}} = -\sqrt{(\omega/c)^2 - |\mathbf{k}_{\parallel}^{\text{out}}|^2}$, $k_{z,\text{out}}^{\text{sam}} = -\sqrt{(n_{\text{sam}}\omega/c)^2 - |\mathbf{k}_{\parallel}^{\text{out}}|^2}$, $\mathbf{k}_{\text{out}}^{\text{air}} = (\mathbf{k}_{\parallel}^{\text{out}}, k_{z,\text{out}}^{\text{air}})$, and $\mathbf{k}_{\text{out}}^{\text{sam}} = (\mathbf{k}_{\parallel}^{\text{out}}, k_{z,\text{out}}^{\text{sam}})$.

A dry objective lens that focuses to point $\mathbf{r}_{\text{in}}^{\text{air}} = (x_f, y_f, z_f^{\text{air}})$ in air produces an input wavefront

$$\tilde{E}_{\text{in}}^{\text{air}}(\mathbf{k}_{\parallel}^{\text{in}}, \omega) = e^{-i\mathbf{k}_{\text{in}}^{\text{air}} \cdot (\mathbf{r}_{\text{in}}^{\text{air}} - \mathbf{r}_{\text{ref}}^{\text{air}})}, \quad (\text{S8})$$

such that the incident wave is

$$E_{\text{in}}^{\text{air}}(\mathbf{r}, t) = \sum_{\mathbf{k}_{\parallel}^{\text{in}}, \omega} \tilde{E}_{\text{in}}^{\text{air}}(\mathbf{k}_{\parallel}^{\text{in}}, \omega) u_{\text{in}}(\mathbf{r}; \mathbf{k}_{\parallel}^{\text{in}}, \omega) e^{-i\omega t} = \begin{cases} \sum_{\mathbf{k}_{\parallel}^{\text{in}}, \omega} e^{i\mathbf{k}_{\text{in}}^{\text{air}} \cdot (\mathbf{r} - \mathbf{r}_{\text{in}}^{\text{air}}) - i\omega t}, & z \leq 0 \\ \sum_{\mathbf{k}_{\parallel}^{\text{in}}, \omega} e^{i\mathbf{k}_{\text{in}}^{\text{sam}} \cdot \mathbf{r} - i\mathbf{k}_{\text{in}}^{\text{air}} \cdot \mathbf{r}_{\text{in}}^{\text{air}} - i\omega t}. & z > 0 \end{cases} \quad (\text{S9})$$

When $z_f^{\text{air}} \leq 0$, $E_{\text{in}}^{\text{air}}(\mathbf{r}, t)$ forms a perfect spatiotemporal focus at $\mathbf{r} = \mathbf{r}_{\text{in}}^{\text{air}}$, $t = 0$, since all terms in the double summation $\sum_{\mathbf{k}_{\parallel}^{\text{in}}, \omega}$ add up in phase. But when the desired focus is in the medium (with $z_f^{\text{air}} > 0$), such a dry objective lens no longer focuses well. At $\mathbf{r} = \mathbf{r}_{\text{in}}^{\text{air}}$, $t = 0$, the different terms in the double summation have relative phase $e^{i(k_{z,\text{in}}^{\text{sam}} - k_{z,\text{in}}^{\text{air}})z_f^{\text{air}}}$, no longer in phase. As illustrated geometrically in the top panel of **Supplementary Fig. 8a**, the spatial focus is now shifted to $\mathbf{r}_{\text{in}} = (x_f, y_f, z_f)$, where the nearby angular components (but not all angular components) add up in phase. For small NA (where $|\mathbf{k}_{\parallel}^{\text{in}}| \ll \omega/c$), $z_f \approx (n_{\text{sam}}/n_{\text{air}})z_f^{\text{air}}$, and the pulse arrives at \mathbf{r}_{in} at time $t = t_f = (n_{\text{sam}}z_f - n_{\text{air}}z_f^{\text{air}})/c$, which compensates for the slower propagation in the medium and the longer distance it needs to propagate (to z_f instead of z_f^{air}). So, $E_{\text{in}}^{\text{air}}(\mathbf{r}, t)$ forms an imperfect spatiotemporal focus at $\mathbf{r} = \mathbf{r}_{\text{in}}$, $t = t_f$. Note that to align the temporal gate with the imperfect spatial gate, the necessary pulse arrival time t_f depends on the depth z_f of the focus.

To form an ideal spatiotemporal focus at $\mathbf{r}_{\text{in}} = (x_f, y_f, z_f)$ inside the medium, we digitally adopt a modified input wavefront

$$\tilde{E}_{\text{in}}(\mathbf{k}_{\parallel}^{\text{in}}, \omega) = e^{-i(\mathbf{k}_{\text{in}}^{\text{sam}} \cdot \mathbf{r}_{\text{in}} - k_{z,\text{in}}^{\text{air}} z_{\text{ref}}^{\text{air}})}. \quad (\text{S10})$$

When focusing inside the medium ($z_f > 0$), the resulting incident wave

$$E_{\text{in}}(\mathbf{r}, t) = \sum_{\mathbf{k}_{\parallel}^{\text{in}}, \omega} \tilde{E}_{\text{in}}(\mathbf{k}_{\parallel}^{\text{in}}, \omega) u_{\text{in}}(\mathbf{r}; \mathbf{k}_{\parallel}^{\text{in}}, \omega) e^{-i\omega t} = \sum_{\mathbf{k}_{\parallel}^{\text{in}}, \omega} e^{i\mathbf{k}_{\text{in}}^{\text{sam}} \cdot (\mathbf{r} - \mathbf{r}_{\text{in}}) - i\omega t} \quad (\text{S11})$$

has all of its angular and spectral components add up perfectly in phase at $\mathbf{r} = \mathbf{r}_{\text{in}}$, $t = t_f = 0$. The pulse arrival time $t_f = 0$ here is independent of the focal depth z_f .

Combining Eqs. (S4, S5, S7, S10), the outgoing field in the sample region (when $z > 0$) is

$$E_{\text{out}}(\mathbf{r}, t; \mathbf{r}_{\text{in}}) = \sum_{\mathbf{k}_{\parallel}^{\text{out}}, \mathbf{k}_{\parallel}^{\text{in}}, \omega} R'(\mathbf{k}_{\parallel}^{\text{out}}, \mathbf{k}_{\parallel}^{\text{in}}, \omega) e^{i[\mathbf{k}_{\text{out}}^{\text{sam}} \cdot \mathbf{r} - \mathbf{k}_{\text{in}}^{\text{sam}} \cdot \mathbf{r}_{\text{in}} - (k_{z,\text{out}}^{\text{air}} - k_{z,\text{in}}^{\text{air}})z_{\text{ref}}^{\text{air}} - i\omega t]}. \quad (\text{S12})$$

We align the input spatial gate with the output spatial gate by setting $\mathbf{r}_{\text{in}} = \mathbf{r}$, and then align the temporal gate with the spatial gates by evaluating E_{out} at time $t = t_f = 0$. The resulting index-mismatch-corrected SMT image is

$$\psi_{\text{SMT}}(\mathbf{r}) = E_{\text{out}}(\mathbf{r}, t = 0; \mathbf{r}_{\text{in}} = \mathbf{r}) = \sum_{\mathbf{k}_{\parallel}^{\text{out}}, \mathbf{k}_{\parallel}^{\text{in}}, \omega} e^{i(\mathbf{k}_{\text{out}}^{\text{sam}} - \mathbf{k}_{\text{in}}^{\text{sam}}) \cdot \mathbf{r}} R(\mathbf{k}_{\parallel}^{\text{out}}, \mathbf{k}_{\parallel}^{\text{in}}, \omega), \quad (\text{S13a})$$

$$R(\mathbf{k}_{\parallel}^{\text{out}}, \mathbf{k}_{\parallel}^{\text{in}}, \omega) \equiv e^{-i(k_{z,\text{out}}^{\text{air}} - k_{z,\text{in}}^{\text{air}})z_{\text{ref}}^{\text{air}}} R'(\mathbf{k}_{\parallel}^{\text{out}}, \mathbf{k}_{\parallel}^{\text{in}}, \omega). \quad (\text{S13b})$$

This recovers Eq. (1) of the main text. Eq. (S13b) shifts the reference plane of the reflection matrix: the original R' has its in-air reference plane at $z = z_{\text{ref}}^{\text{air}} = z_{\text{mirror}}$, and the new R has its in-medium reference plane at the air-sample interface at $z = 0$. We also see explicitly that SMT uses momenta $\mathbf{k}_{\text{in}/\text{out}}^{\text{sam}}$ inside the sample to focus inside the sample medium.

2. Double-interface index mismatch

For a sample under a coverslip with thickness h^{glass} , there are two interfaces: an air-glass interface at $z = -h^{\text{glass}}$ and a glass-sample interface at $z = 0$ (**Supplementary Fig. 8b**). We choose the zero of the coordinate such that z is the depth into the sample. Here,

$$u_{\text{in}}(\mathbf{r}; \mathbf{k}_{\parallel}^{\text{in}}, \omega) = \begin{cases} e^{i\mathbf{k}_{\text{in}}^{\text{air}} \cdot (\mathbf{r} - \mathbf{r}_{\text{ref}}^{\text{air}})}, & z \leq -h^{\text{glass}} \\ e^{i[\mathbf{k}_{\text{in}}^{\text{glass}} \cdot \mathbf{r} - k_{z,\text{in}}^{\text{air}}(h^{\text{glass}} + z_{\text{ref}}^{\text{air}}) + k_{z,\text{in}}^{\text{glass}} h^{\text{glass}}]}, & -h^{\text{glass}} < z \leq 0 \\ e^{i[\mathbf{k}_{\text{in}}^{\text{sam}} \cdot \mathbf{r} - k_{z,\text{in}}^{\text{air}}(h^{\text{glass}} + z_{\text{ref}}^{\text{air}}) + k_{z,\text{in}}^{\text{glass}} h^{\text{glass}}]}, & z > 0 \end{cases} \quad (\text{S14})$$

and

$$u_{\text{out}}(\mathbf{r}; \mathbf{k}_{\parallel}^{\text{out}}, \omega) = \begin{cases} e^{i\mathbf{k}_{\text{out}}^{\text{air}} \cdot (\mathbf{r} - \mathbf{r}_{\text{ref}}^{\text{air}})}, & z \leq -h^{\text{glass}} \\ e^{i[\mathbf{k}_{\text{out}}^{\text{glass}} \cdot \mathbf{r} - k_{z,\text{out}}^{\text{air}}(h^{\text{glass}} + z_{\text{ref}}^{\text{air}}) + k_{z,\text{out}}^{\text{glass}} h^{\text{glass}}]}, & -h^{\text{glass}} < z \leq 0 \\ e^{i[\mathbf{k}_{\text{out}}^{\text{sam}} \cdot \mathbf{r} - k_{z,\text{out}}^{\text{air}}(h^{\text{glass}} + z_{\text{ref}}^{\text{air}}) + k_{z,\text{out}}^{\text{glass}} h^{\text{glass}}]}, & z > 0 \end{cases} \quad (\text{S15})$$

which ensure that the in-air reference point is at $\mathbf{r} = \mathbf{r}_{\text{ref}}^{\text{air}}$ and continuity across the interfaces. The definitions are the same as in the previous section, and we additionally introduce the momentum in the coverslip as $k_{z,\text{in}}^{\text{glass}} = \sqrt{(n_{\text{glass}}\omega/c)^2 - |\mathbf{k}_{\parallel}^{\text{in}}|^2}$, $\mathbf{k}_{\text{in}}^{\text{glass}} = (\mathbf{k}_{\parallel}^{\text{in}}, k_{z,\text{in}}^{\text{glass}})$, $k_{z,\text{out}}^{\text{glass}} = -\sqrt{(n_{\text{glass}}\omega/c)^2 - |\mathbf{k}_{\parallel}^{\text{out}}|^2}$, and $\mathbf{k}_{\text{out}}^{\text{glass}} = (\mathbf{k}_{\parallel}^{\text{out}}, k_{z,\text{out}}^{\text{glass}})$.

When computing k_z^{glass} and k_z^{sam} , a rough estimate of n_{glass} and n_{sam} will suffice since we also perform dispersion compensation and wavefront optimizations later. Here, we take $n_{\text{glass}}(\omega)$ to be that of SCHOTT D263T Thin Glass [5] and we take $n_{\text{sam}}(\omega)$ to be that of water [6] and polydimethylsiloxane (PDMS) [7] respectively for the USAF-target-under-tissue sample and the nanoparticle colloid sample, with data from refractiveindex.info [8]. If the material is unknown, one can carry out an image metric optimization (similar to the dispersion compensation in Supplementary Sect. III E below) to estimate its average refractive index.

To create an ideal spatiotemporal focus at $\mathbf{r}_{\text{in}} = (x_f, y_f, z_f)$ inside the sample (with $z_f > 0$), we digitally generate an input wavefront

$$\tilde{E}_{\text{in}}(\mathbf{k}_{\parallel}^{\text{in}}, \omega) = e^{-i[\mathbf{k}_{\text{in}}^{\text{sam}} \cdot \mathbf{r}_{\text{in}} - k_{z,\text{in}}^{\text{air}}(h^{\text{glass}} + z_{\text{ref}}^{\text{air}}) + k_{z,\text{in}}^{\text{glass}} h^{\text{glass}}]}. \quad (\text{S16})$$

Like Eq. (S11), the resulting incident field $E_{\text{in}}(\mathbf{r}, t)$ forms an ideal spatiotemporal focus at $\mathbf{r} = \mathbf{r}_{\text{in}}$, $t = 0$. The corresponding output field inside the sample ($z > 0$) is

$$E_{\text{out}}(\mathbf{r}, t; \mathbf{r}_{\text{in}}) = \sum_{\mathbf{k}_{\parallel}^{\text{out}}, \mathbf{k}_{\parallel}^{\text{in}}, \omega} R'(\mathbf{k}_{\parallel}^{\text{out}}, \mathbf{k}_{\parallel}^{\text{in}}, \omega) e^{i[\mathbf{k}_{\text{out}}^{\text{sam}} \cdot \mathbf{r} - \mathbf{k}_{\text{in}}^{\text{sam}} \cdot \mathbf{r}_{\text{in}} - (k_{z,\text{out}}^{\text{air}} - k_{z,\text{in}}^{\text{air}})(h^{\text{glass}} + z_{\text{ref}}^{\text{air}}) + (k_{z,\text{out}}^{\text{glass}} - k_{z,\text{in}}^{\text{glass}})h^{\text{glass}} - i\omega t]}. \quad (\text{S17})$$

As before, we align the three gates to obtain

$$\psi_{\text{SMT}}(\mathbf{r}) = E_{\text{out}}(\mathbf{r}, t = 0; \mathbf{r}_{\text{in}} = \mathbf{r}) = \sum_{\mathbf{k}_{\parallel}^{\text{out}}, \mathbf{k}_{\parallel}^{\text{in}}, \omega} e^{i(\mathbf{k}_{\text{out}}^{\text{sam}} - \mathbf{k}_{\text{in}}^{\text{sam}}) \cdot \mathbf{r}} R(\mathbf{k}_{\parallel}^{\text{out}}, \mathbf{k}_{\parallel}^{\text{in}}, \omega), \quad (\text{S18a})$$

$$R(\mathbf{k}_{\parallel}^{\text{out}}, \mathbf{k}_{\parallel}^{\text{in}}, \omega) \equiv e^{-i(k_{z,\text{out}}^{\text{air}} - k_{z,\text{in}}^{\text{air}})(h^{\text{glass}} + z_{\text{ref}}^{\text{air}})} e^{i(k_{z,\text{out}}^{\text{glass}} - k_{z,\text{in}}^{\text{glass}})h^{\text{glass}}} R'(\mathbf{k}_{\parallel}^{\text{out}}, \mathbf{k}_{\parallel}^{\text{in}}, \omega), \quad (\text{S18b})$$

which again recovers Eq. (1) of the main text. The original R' has an in-air reference plane at $z = z_{\text{ref}}^{\text{air}} = z_{\text{mirror}}$. The new R has its in-medium reference plane at the glass-sample interface at $z = 0$ [by shifting the reference plane to the air-glass interface with the first factor of Eq. (S18b) and then to the glass-sample interface with the second factor of Eq. (S18b)].

D. Layer-thickness measurement and depth calibration

Accurately correcting the refractive index mismatches requires accurate knowledge of the coverslip thickness h^{glass} and of the reference plane location $z_{\text{ref}}^{\text{air}} = z_{\text{mirror}}$. They are also needed for us to determine the precise imaging depth.

To determine h^{glass} and $z_{\text{ref}}^{\text{air}}$, we first place the air-glass interface at the objective lens focal plane, which makes the iris in the incidence path clearly imaged on the camera (Supplementary Sect. IA). We then use the motorized translation stage to shift the sample backward along the axial z direction by $70 \mu\text{m}$ (so that $z_{\text{ref}}^{\text{air}}$ is known) and then perform SMT to image the glass-sample interface, using the single-interface index mismatch correction of Sect. III C 1. The SMT image gives $h^{\text{glass}} = 141.5 \mu\text{m}$ for the USAF-target-under-tissue sample and $h^{\text{glass}} = 154 \mu\text{m}$ for the nanoparticle colloid sample. This procedure can be repeated if multiple layers are present.

Then, we move the sample forward to place the air-glass interface at the objective lens focal plane again, shift the sample backward in z by $h^{\text{glass}} + z_{\text{ref}}^{\text{air}}$, and perform SMT imaging there. Given the depth range of interest, we use geometric optics to estimate the $z_{\text{ref}}^{\text{air}}$ to set: $(h^{\text{glass}} + z_{\text{ref}}^{\text{air}}) \tan \theta^{\text{air}} = h^{\text{glass}} \tan \theta^{\text{glass}} + z_{\text{f}}^{\text{sam}}(\theta^{\text{air}}) \tan \theta^{\text{sam}}$. Here, $z_{\text{f}}^{\text{sam}}(\theta^{\text{air}})$ is the depth of the focal plane in the sample (illustrated in **Supplementary Fig. 8b**), which depends on the incident angle. θ^{air} , θ^{glass} , and θ^{sam} are incident angles in air, glass, and the sample, respectively, related through Snell's law: $\sin \theta^{\text{air}} = n_{\text{glass}} \sin \theta^{\text{glass}} = n_{\text{sam}} \sin \theta^{\text{sam}}$. For the data in this paper, we set $z_{\text{ref}}^{\text{air}} = 678.5 \mu\text{m}$ for the USAF target under brain tissue, resulting in the single-angle focal-plane depth ranging from $z_{\text{f}}^{\text{sam}}(0^\circ) = 965 \mu\text{m}$ to $z_{\text{f}}^{\text{sam}}(30^\circ) = 1044 \mu\text{m}$ (with $n_{\text{glass}} = 1.5$ and $n_{\text{sam}} = 1.33$) for the angular range (NA = 0.5) being considered. For the nanoparticle colloid sample, we use $z_{\text{ref}}^{\text{air}} = 996 \mu\text{m}$, leading to a $z_{\text{f}}^{\text{sam}}(0^\circ) = 1466 \mu\text{m}$ and $z_{\text{f}}^{\text{sam}}(30^\circ) = 1594 \mu\text{m}$ (with $n_{\text{sam}} = 1.4$). Note that the depth of field of the SMT image can go beyond the range of $z_{\text{f}}^{\text{sam}}$, as described in Supplementary Sect. IX B.

In SMT, the absolute image depth z is quantitatively determined by the other variables thanks to the index-mismatch correction. Given the frequency ω measured by the wavemeter, $\mathbf{k}_{\parallel}^{\text{out}}$ from off-axis holography (Supplementary Sect. I C), $\mathbf{k}_{\parallel}^{\text{in}}$ from incident angle calibration (Supplementary Sect. III A), h^{glass} measured through imaging the glass-sample interface, $z_{\text{ref}}^{\text{air}}$ set by the motorized translation stage, and the estimated refractive indices, we can reconstruct the image $\psi_{\text{SMT}}(x, y, z)$ with a quantitative depth coordinate z .

E. Compensation for sample dispersion

Next, we correct the dispersion of the sample and the output path of the optical system by introducing a frequency-dependent phase shift $\theta(\omega)$ to the scattering matrix. We assume the dispersion is spatially invariant and only depends on the frequency. Since the angles do not affect dispersion, we pre-compute the angular summations as

$$\tilde{\psi}_{\text{SMT}}(\mathbf{r}, \omega) \equiv \sum_{\mathbf{k}_{\parallel}^{\text{out}}, \mathbf{k}_{\parallel}^{\text{in}}} e^{i(\mathbf{k}_{\text{out}} - \mathbf{k}_{\text{in}}) \cdot \mathbf{r}} R(\mathbf{k}_{\parallel}^{\text{out}}, \mathbf{k}_{\parallel}^{\text{in}}, \omega) \quad (\text{S19})$$

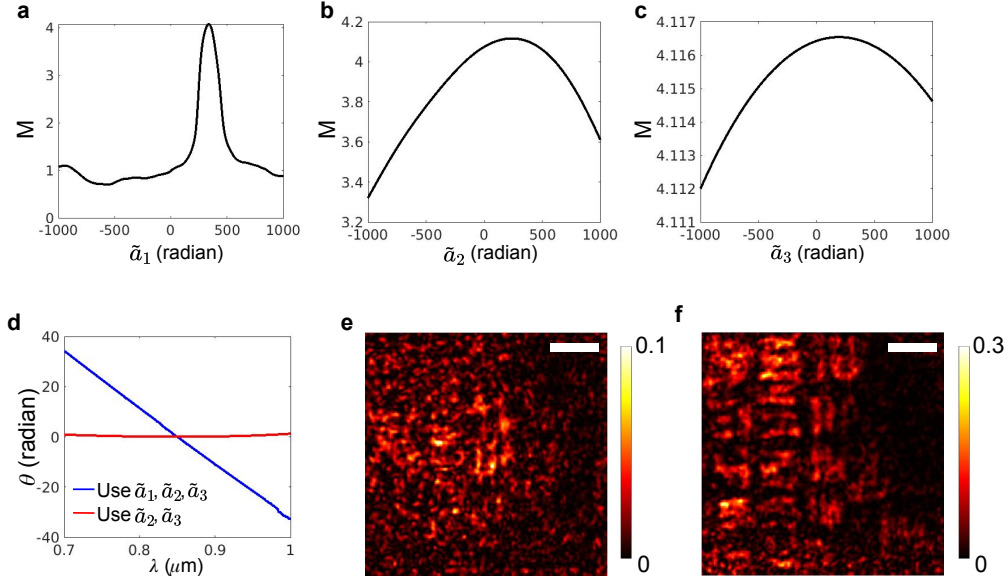
such that $\psi_{\text{SMT}}(\mathbf{r}) = \sum_{\omega} e^{i\theta(\omega)} \tilde{\psi}_{\text{SMT}}(\mathbf{r}, \omega)$ and $I_{\text{SMT}}(\mathbf{r}) = |\psi_{\text{SMT}}(\mathbf{r})|^2$ before we perform wavefront corrections [when $\phi_{\text{out}}(\mathbf{k}_{\parallel}^{\text{out}}) = \phi_{\text{in}}(\mathbf{k}_{\parallel}^{\text{in}}) = 0$], following Eq. (2) of the main text. Hereafter, we abbreviate $\mathbf{k}_{\text{out}}^{\text{sam}}$ and $\mathbf{k}_{\text{in}}^{\text{sam}}$ as \mathbf{k}_{out} and \mathbf{k}_{in} for conciseness. To determine $\theta(\omega)$, we maximize an image quality metric (also referred to as the ‘‘objective function’’ or ‘‘figure of merit’’ of the optimization)

$$M \equiv \sum_{\mathbf{r}} I_{\text{SMT}}(\mathbf{r}) \ln \frac{I_{\text{SMT}}(\mathbf{r})}{I_0}. \quad (\text{S20})$$

The precise choice of the image quality metric is not crucial. For example, we have found similar performances with $M' \equiv \sum_{\mathbf{r}} I_{\text{SMT}}(\mathbf{r})$ and $M'' \equiv \sum_{\mathbf{r}} I_{\text{SMT}}^2(\mathbf{r})$.

For the sample of USAF target under mouse brain tissue, we first scan z and record M for the 2D *en-face* image at each depth. We found $z_1 = 994.5 \mu\text{m}$ is the depth where M is maximized before dispersion compensation. We then perform dispersion compensation with M summed over positions \mathbf{r} in a 3D volume containing z_1 : $x, y \in [0, 50] \mu\text{m}$ and $z \in [970, 1030] \mu\text{m}$. The axial range allows the dispersion compensation to sharpen the axial resolution through the temporal gate. For the sample of dense nanoparticle colloid, we sum over positions \mathbf{r} in a volume spanning $x, y \in [0, 50] \mu\text{m}$ and $z \in [1470, 1580] \mu\text{m}$. A relatively coarse $0.7 \times 0.7 \times 1 \mu\text{m}^3$ voxel size is used to speed up the summation. We choose the normalization constant I_0 to be 10^{-3} times the maximal I_{SMT} before optimization. Our experience is that the value of I_0 does not change the result as long as it is not too large.

While it may be tempting to allow the phase $\theta(\omega)$ at every frequency to be an independent variable in the optimization, doing so will lead to overfitting and make it easier for the optimization to get trapped in a poor local optimum given the very high dimensionality of the parameter space (see Fig. 2b of the main text). To regularize the



Supplementary Fig. 9. Dispersion compensation for USAF target under tissue. **a–c** Normalized SMT image quality metric $M = \sum_{\mathbf{r}} I_{\text{SMT}}(\mathbf{r}) \ln I_{\text{SMT}}(\mathbf{r})$ as a function of the dispersion coefficients \tilde{a}_j . **d** The optimized $\theta(\omega)$. **e** The USAF target image at $z = z_1 = 994.5 \mu\text{m}$ before dispersion compensation. **f** The USAF target image at $z = z_{\text{target}} = 977.5 \mu\text{m}$ after dispersion compensation. Scale bar: $10 \mu\text{m}$. Note that prior to this sample dispersion compensation, we have already removed the dispersion in the input path of the optical system through a calibration mirror (Supplementary Sect. III B) and removed the dispersion from refractive index mismatch (Supplementary Sect. III C).

optimization while reducing the dimensionality, we express $\theta(\omega)$ as a third-order polynomial [9],

$$\theta(\omega) = \tilde{a}_1 \frac{\omega - \omega_0}{\omega_0} + \tilde{a}_2 \left(\frac{\omega - \omega_0}{\omega_0} \right)^2 + \tilde{a}_3 \left(\frac{\omega - \omega_0}{\omega_0} \right)^3, \quad (\text{S21})$$

where ω_0 is the central frequency, and \tilde{a}_j ($j = 1, 2, 3$) are dimensionless dispersion coefficients corresponding to the inverse group velocity (correcting for axial shifts of the temporal gate), group velocity dispersion (correcting for symmetric pulse broadening), and third-order dispersion (correcting for asymmetric pulse distortion), respectively.

To maximize the image metric M while avoiding poor local optima, we optimize one variable at a time. We first align the temporal gate with the spatial gates by scanning \tilde{a}_1 to obtain \tilde{a}_1^{max} while keeping $\tilde{a}_2 = \tilde{a}_3 = 0$. Then, we perform symmetric pulse compression by scanning \tilde{a}_2 to obtain \tilde{a}_2^{max} while keeping $\tilde{a}_1 = \tilde{a}_1^{\text{max}}$ and $\tilde{a}_3 = 0$. Finally, we perform asymmetric pulse compression by scanning \tilde{a}_3 to obtain \tilde{a}_3^{max} while keeping $\tilde{a}_1 = \tilde{a}_1^{\text{max}}$, $\tilde{a}_2 = \tilde{a}_2^{\text{max}}$. This process is shown in **Supplementary Fig. 9** for the sample of USAF target under mouse brain tissue. The scanning is the most important for \tilde{a}_1 as its objective function landscape is the most nonconvex.

To further push the performance, we additionally perform a local gradient-based optimization to optimize all three variables simultaneously, using $(\tilde{a}_1^{\text{max}}, \tilde{a}_2^{\text{max}}, \tilde{a}_3^{\text{max}})$ as the initial guess. The gradient of M with respect to \tilde{a}_j is

$$\frac{\partial M}{\partial \tilde{a}_j} = -2 \sum_{\mathbf{r}, \omega} \text{Im} \left\{ \left[1 + \ln \frac{I_{\text{SMT}}(\mathbf{r})}{I_0} \right] \psi_{\text{SMT}}^*(\mathbf{r}) \tilde{\psi}_{\text{SMT}}(\mathbf{r}, \omega) e^{i\theta(\omega)} \right\} \left(\frac{\omega - \omega_0}{\omega_0} \right)^j. \quad (\text{S22})$$

To compute this gradient efficiently in MATLAB, we use vector-matrix multiplications to perform the spatial and frequency summations. Specifically, $I_{\text{SMT}}(\mathbf{r}_i)$, $\psi_{\text{SMT}}^*(\mathbf{r}_i)$, and $\theta(\omega_k)$ are each stored in a row vector, \mathbf{I} , $\boldsymbol{\psi}^*$, and $\boldsymbol{\theta}$. $\tilde{\psi}_{\text{SMT}}(\mathbf{r}_i, \omega_k)$ is stored in the ik element of a matrix $\tilde{\boldsymbol{\psi}}$, and $(\frac{\omega_k - \omega_0}{\omega_0})^j$ in the kj element of matrix $\boldsymbol{\Omega}$. We then compute the gradient as a row vector by

$$\frac{\partial M}{\partial \tilde{\mathbf{a}}} = -2 \text{Im} \left\{ \left[\left(\left(1 + \ln \frac{\mathbf{I}}{I_0} \right) \otimes \boldsymbol{\psi}^* \right) \tilde{\boldsymbol{\psi}} \right] \otimes e^{i\boldsymbol{\theta}} \right\} \boldsymbol{\Omega}, \quad (\text{S23})$$

where \otimes denotes the Hadamard (element-wise) product between row vectors, and the other products are vector-matrix products. Note that the matrices $\tilde{\boldsymbol{\psi}}$ and $\boldsymbol{\Omega}$ are both pre-computed and fixed; only the vectors \mathbf{I} , $\boldsymbol{\psi}^*$, and $\boldsymbol{\theta}$ are updated during the optimization. We use the NLOpt library [10] for the optimization, adopting the low-storage

Broyden–Fletcher–Goldfarb–Shanno (L-BFGS) algorithm [11]. L-BFGS is a second-order quasi-Newton method that uses the gradient and an approximation of the Hessian matrix of the objective function to determine the search direction and estimates a step size. We set the upper and lower bounds of $\tilde{\mathbf{a}}$ to be $(\tilde{a}_1^{\max} \pm 100, \tilde{a}_2^{\max} \pm 100, \tilde{a}_3^{\max} \pm 100)$ in the optimization, with the stopping criterion being when both the objective function M and the variables $\tilde{\mathbf{a}}$ change less than 0.01%.

Supplementary Fig. 9e–f and **Supplementary Fig. 13a–b** show the images before and after dispersion compensation for the USAF target under mouse brain tissue and the nanoparticle colloid samples respectively. We then determine the depth $z_{\text{target}} = 977.5 \mu\text{m}$ of the USAF target as the depth z at which the *en-face* image quality metric M is the highest.

F. Input and output wavefront corrections

After dispersion compensation, we optimize angle-dependent phases $\phi_{\text{in}}(\mathbf{k}_{\parallel}^{\text{in}})$ and $\phi_{\text{out}}(\mathbf{k}_{\parallel}^{\text{out}})$ to correct for the output aberrations of the optical system and for the aberrations and multiple scatterings from the heterogeneous sample. We maximize the same image quality metric M as in Eq. (S20), with the spatial summation summing over one or several *en-face* x - y planes at depths z_j ($j = 1, 2, \dots$) inside the volume of interest. For the USAF target under mouse brain sample, we use one depth $z_1 = z_{\text{target}}$ since the target is planar. For the nanoparticle colloid sample, we divide the full volume (across $110 \mu\text{m}$ depth of field in z) into 16 overlapping sub-volumes, and pick five equally spaced slices z_1, z_2, \dots, z_5 within each sub-volume where z_1 and z_5 are the two ends of the sub-volume; the same wavefront correction is then applied to all slices within each sub-volume. We treat the wavefront corrections $\phi_{\text{in}}(\mathbf{k}_{\parallel}^{\text{in}})$ and $\phi_{\text{out}}(\mathbf{k}_{\parallel}^{\text{out}})$ to be frequency independent.

Since the spectral phase $\theta(\omega)$ has been determined and since $z = z_j$ is fixed, we pre-compute the frequency summation to obtain the depth-resolved “synthetic time-gated reflection matrix” at each depth z_j ,

$$\tilde{R}(\mathbf{k}_{\parallel}^{\text{out}}, \mathbf{k}_{\parallel}^{\text{in}}; z_j) \equiv \sum_{\omega} e^{i\theta(\omega)} e^{i(k_z^{\text{out}} - k_z^{\text{in}})z_j} R(\mathbf{k}_{\parallel}^{\text{out}}, \mathbf{k}_{\parallel}^{\text{in}}, \omega). \quad (\text{S24})$$

Recall that $\mathbf{k}_{\text{in}} = (\mathbf{k}_{\parallel}^{\text{in}}, k_z^{\text{in}})$, $\mathbf{k}_{\text{out}} = (\mathbf{k}_{\parallel}^{\text{out}}, k_z^{\text{out}})$. Note $k_z^{\text{in/out}} = \pm \sqrt{|\mathbf{k}_{\parallel}|^2 - (n_{\text{sam}}\omega/c)^2}$ depends on the frequency ω . For the optimization over $\phi_{\text{in}}(\mathbf{k}_{\parallel}^{\text{in}})$, we further pre-compute the summation over the outgoing angles for each j , as

$$\psi_{\text{SMT}}^{j,\text{in}}(\mathbf{r}_{\parallel}, \mathbf{k}_{\parallel}^{\text{in}}; z_j) \equiv \sum_{\mathbf{k}_{\parallel}^{\text{out}}} e^{i(\mathbf{k}_{\parallel}^{\text{out}} - \mathbf{k}_{\parallel}^{\text{in}}) \cdot \mathbf{r}_{\parallel} + i\phi_{\text{out}}(\mathbf{k}_{\parallel}^{\text{out}})} \tilde{R}(\mathbf{k}_{\parallel}^{\text{out}}, \mathbf{k}_{\parallel}^{\text{in}}; z_j), \quad (\text{S25})$$

where $\mathbf{r}_{\parallel} = (x, y)$, such that $\psi_{\text{SMT}}(\mathbf{r}_{\parallel}, z_j) = \sum_{\mathbf{k}_{\parallel}^{\text{in}}} e^{i\phi_{\text{in}}(\mathbf{k}_{\parallel}^{\text{in}})} \psi_{\text{SMT}}^{j,\text{in}}(\mathbf{r}_{\parallel}, \mathbf{k}_{\parallel}^{\text{in}}; z_j)$ on the j -th slice. For the $\phi_{\text{out}}(\mathbf{k}_{\parallel}^{\text{out}})$ optimization, we pre-compute

$$\psi_{\text{SMT}}^{j,\text{out}}(\mathbf{r}_{\parallel}, \mathbf{k}_{\parallel}^{\text{out}}; z_j) \equiv \sum_{\mathbf{k}_{\parallel}^{\text{in}}} e^{i(\mathbf{k}_{\parallel}^{\text{out}} - \mathbf{k}_{\parallel}^{\text{in}}) \cdot \mathbf{r}_{\parallel} + i\phi_{\text{in}}(\mathbf{k}_{\parallel}^{\text{in}})} \tilde{R}(\mathbf{k}_{\parallel}^{\text{out}}, \mathbf{k}_{\parallel}^{\text{in}}; z_j), \quad (\text{S26})$$

such that $\psi_{\text{SMT}}(\mathbf{r}_{\parallel}, z_j) = \sum_{\mathbf{k}_{\parallel}^{\text{out}}} e^{i\phi_{\text{out}}(\mathbf{k}_{\parallel}^{\text{out}})} \psi_{\text{SMT}}^{j,\text{out}}(\mathbf{r}_{\parallel}, \mathbf{k}_{\parallel}^{\text{out}}; z_j)$. We evaluate \mathbf{r}_{\parallel} on a relatively coarse $(0.7 \mu\text{m})^2$ spatial grid to speed up the computation.

Like the spectral phase optimization, here it is better to avoid overfitting and not to allow the angular phase at every incident angle and every outgoing angle to be an independent variable. To regularize the optimization, we expand the phase-correction maps in Zernike polynomials [12]

$$\phi_{\text{in}}(\mathbf{k}_{\parallel}^{\text{in}}) = \sum_n c_n^{\text{in}} Z_n \left(\frac{\mathbf{k}_{\parallel}^{\text{in}}}{k_0^{\text{maxNA}}} \right), \quad \phi_{\text{out}}(\mathbf{k}_{\parallel}^{\text{out}}) = \sum_n c_n^{\text{out}} Z_n \left(\frac{\mathbf{k}_{\parallel}^{\text{out}}}{k_0^{\text{maxNA}}} \right), \quad (\text{S27})$$

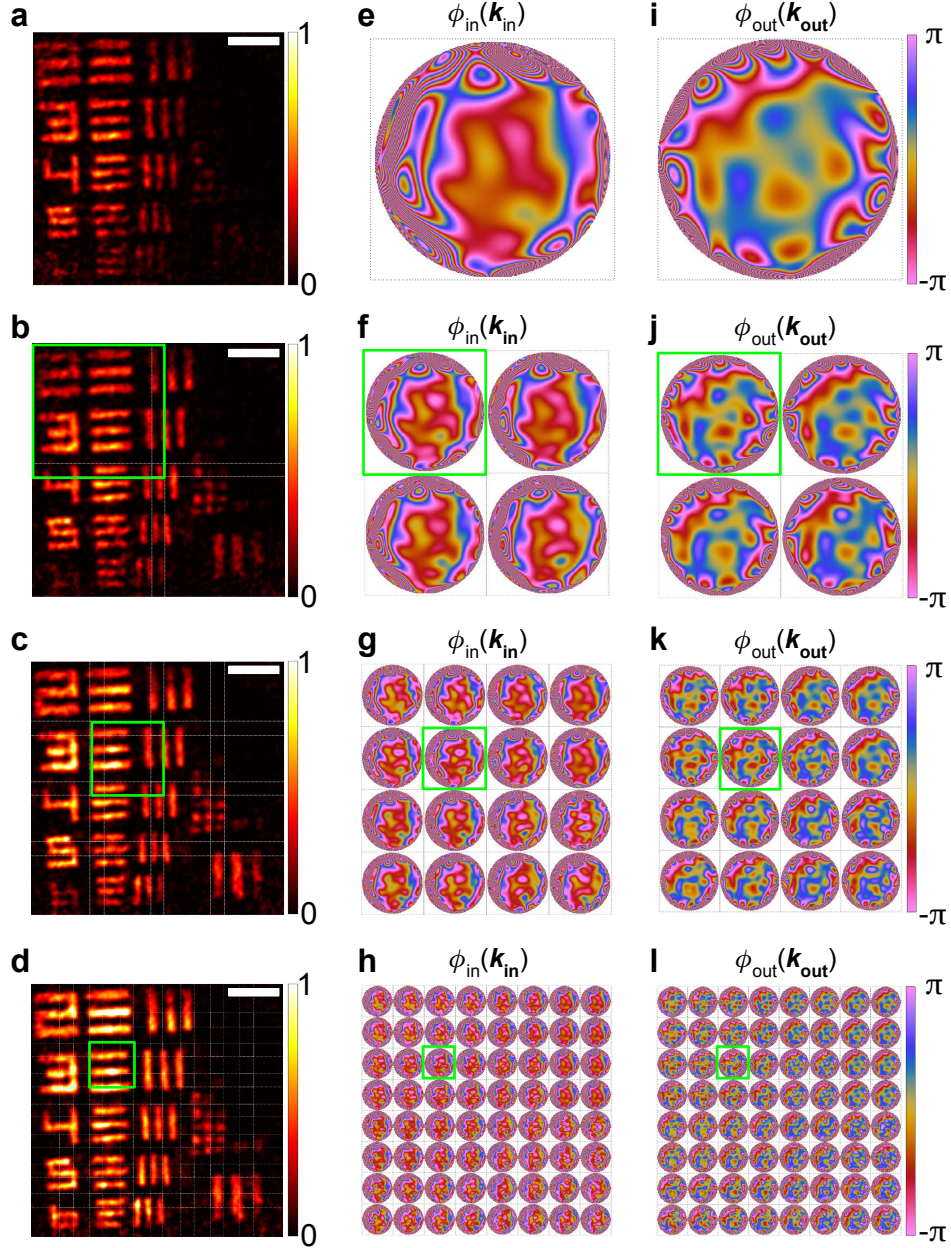
where $\{c_n^{\text{in}}\}$ and $\{c_n^{\text{out}}\}$ are the Zernike coefficients (weights), $k_0^{\text{max}} = \omega_{\text{max}}/c$ is the vacuum wave number for the highest frequency considered, and Z_n is the n -th Zernike polynomial. Note that the Zernike polynomials form a complete basis for functions on a disk, so they can incorporate both the slowly-varying distortions from aberrations and the fast-changing wavefronts caused by multiple scattering.

The gradient of the image metric M in Eq. (S20) with respect to $\{c_n^{\text{in}}\}$ is

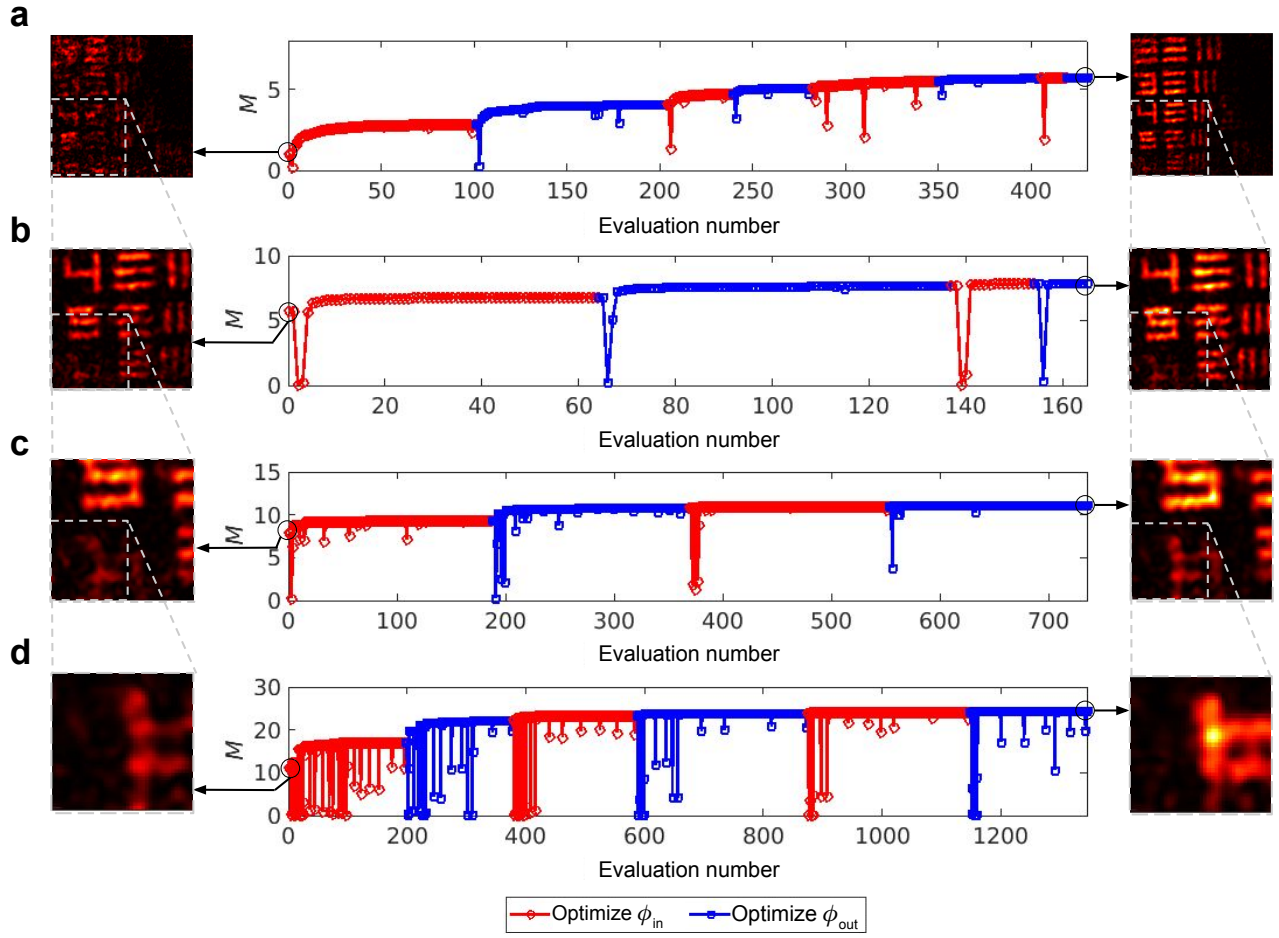
$$\frac{\partial M}{\partial c_n^{\text{in}}} = -2 \sum_{j, \mathbf{r}_{\parallel}, \mathbf{k}_{\parallel}^{\text{in}}} \text{Im} \left\{ \left[1 + \ln \frac{I_{\text{SMT}}(\mathbf{r}_{\parallel}, z_j)}{I_0} \right] \psi_{\text{SMT}}^*(\mathbf{r}_{\parallel}, z_j) \psi_{\text{SMT}}^{j,\text{in}}(\mathbf{r}_{\parallel}, \mathbf{k}_{\parallel}^{\text{in}}; z_j) e^{i\phi_{\text{in}}(\mathbf{k}_{\parallel}^{\text{in}})} \right\} Z_n \left(\frac{\mathbf{k}_{\parallel}^{\text{in}}}{k_0^{\text{maxNA}}} \right), \quad (\text{S28})$$

and similarly for the gradient with respect to $\{c_n^{\text{out}}\}$. Like Eqs. (S22)–(S23), these gradients can be evaluated efficiently using vector-matrix multiplications.

We first keep $c_n^{\text{out}} = 0$, pre-compute $\psi_{\text{SMT}}^{j,\text{in}}(\mathbf{r}_{\parallel}, \mathbf{k}_{\parallel}^{\text{in}}; z_j)$, and determine $\{c_n^{\text{in}}\}$ by maximizing the image quality metric with the L-BFGS algorithm and with $c_n^{\text{in}} = 0$ as the initial guess. We set the upper and lower bounds as ± 10 radians, with the stopping criterion being when both the objective function M and the variables c_n^{in} change less than 0.01%. This optimization is very fast since the most time-consuming step of computing $\psi_{\text{SMT}}^{j,\text{in}}(\mathbf{r}_{\parallel}, \mathbf{k}_{\parallel}^{\text{in}}; z_j)$ has already been done prior. Then, we fix $\{c_n^{\text{in}}\}$, pre-compute $\psi_{\text{SMT}}^{j,\text{out}}(\mathbf{r}_{\parallel}, \mathbf{k}_{\parallel}^{\text{in}}; z_j)$, and optimize $\{c_n^{\text{out}}\}$. We alternate between $\phi_{\text{in}}(\mathbf{k}_{\parallel}^{\text{in}})$ optimization and $\phi_{\text{out}}(\mathbf{k}_{\parallel}^{\text{out}})$ optimization until when M changes less than 5%, each time using the previous phase maps as the initial guess.



Supplementary Fig. 10. Progressive bisection and wavefront correction maps for the USAF target under mouse brain sample. a–d The wavefront-corrected image during a progression that bisects the area at each step. Scale bar: 10 μm . All images share the same normalization. White dotted lines indicate zone boundaries, with 2.4 μm of overlap between neighboring zones. e–l The input and output wavefront correction maps of the zones.



Supplementary Fig. 11. Evolution of the image quality metric M during the optimization process. Each panel shows the evolution for one zone as the zone size is reduced. The inset figures on the left and right are the images before and after optimization. All images share the same normalization as **Supplementary Fig. 10**.

Since the $50 \times 50 \mu\text{m}^2$ field of view is larger than the isoplanatic patch size at the depths we consider, the spatial variation of the wavefront corrections must be accounted for. A simple strategy would be directly performing wavefront optimizations within spatial zones smaller than the isoplanatic patch size. However, as described in Sec. II of the main text, summing over more spatial points inside the isoplanatic patch can boost the relative contribution of the target signals, making it less likely for the optimization to get stuck in a poor local optimum that corresponds to optimizing speckles. Therefore, the ideal zone size is the isoplanatic patch size—the maximal zone size within which the wavefront correction is invariant. As mentioned in the main text, the isoplanatic patch size depends on the order of the Zernike polynomials. This motivates us to adopt a progression strategy: first optimize the image over the full field of view with the low-order Zernike polynomials and with the whole image sharing the same phase map, then bisect the image into 2×2 zones and optimize the wavefronts for each zone while adding higher-order Zernike polynomials. The wavefronts obtained from the previous (larger-zone) optimization are used as the initial guess for the smaller zone; such “progression” ensures that the non-convex optimization ends up in a good local optimum. As we continue to bisect into smaller zones, we observe the image quality to converge, at which point we stop the bisection; this is where the zone size has become smaller than the isoplanatic patch size of the high-order corrections. After optimization, the zones are stitched together to yield the full image. To avoid image discontinuity at the zone boundaries, we let neighboring zones overlap by $2.4 \mu\text{m}$ and stitch them using a weighted average with a linear ramp.

Supplementary Figs. 10–11 show the evolution of the image, the phase maps, and the image quality metric during this progression process for the USAF target under mouse brain sample. Here, we use 11, 15, 19, and 22 radial orders of Zernike polynomials for the full image, 2×2 zones, 4×4 zones, and 8×8 zones respectively (corresponding to 77, 135, 209, and 275 Zernike polynomials). The number of Zernike polynomials can be relatively flexible, as long as it is not too small (insufficient to capture the higher-order wavefront distortions) or too large (which causes overfitting). Note that the x -axis of **Supplementary Fig. 11** is the number of objective function evaluations, not

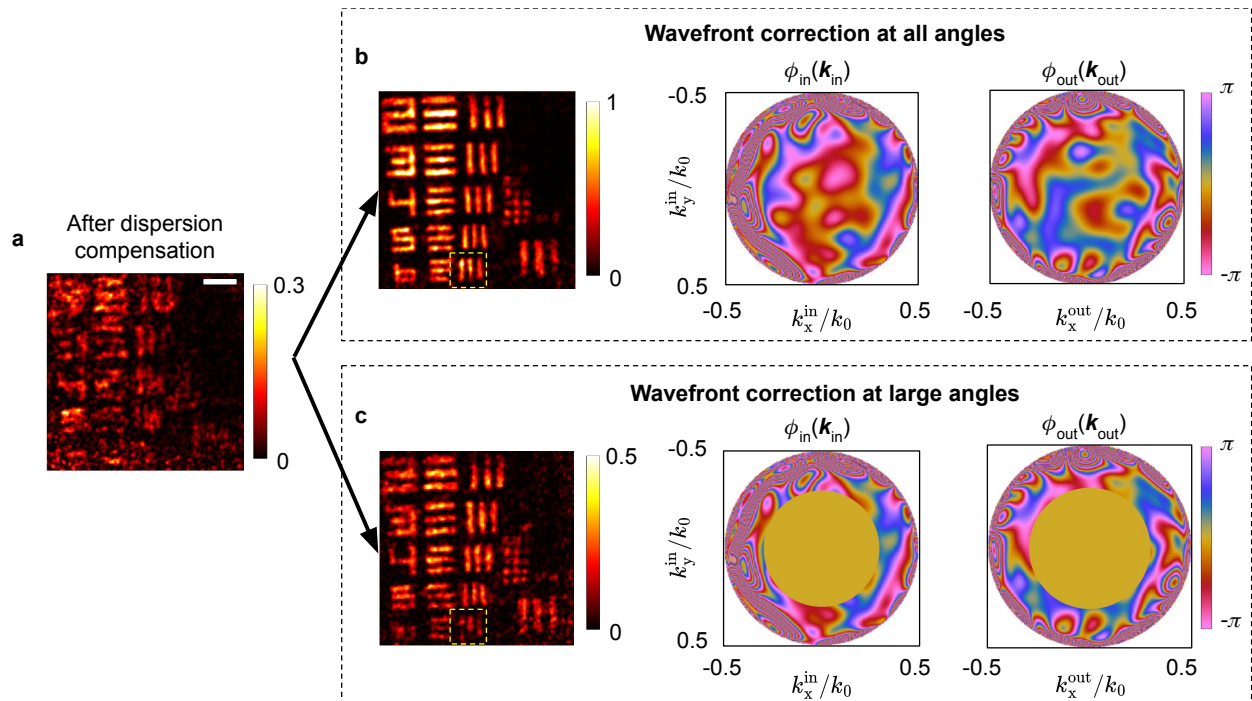
the L-BFGS iteration number. Within each L-BFGS iteration, there is a line search to refine the step size, during which the objective function may dip.

A caveat of such image-metric-based wavefront optimization is that when there are strong scatterers outside the volume considered in the \mathbf{r} summation of Eq. (S20), the optimization may overfit by distorting the wavefront to smear or to move such outside targets such that they contribute to the volume being optimized. Such a nuisance is particularly relevant for the progression strategy, where targets may lie on the zone boundaries. To address this issue, we Fourier transform the synthetic time-gated reflection matrix $\tilde{R}(\mathbf{k}_{\parallel}^{\text{out}}, \mathbf{k}_{\parallel}^{\text{in}}; z_j)$ in Eq. (S24) to spatial basis

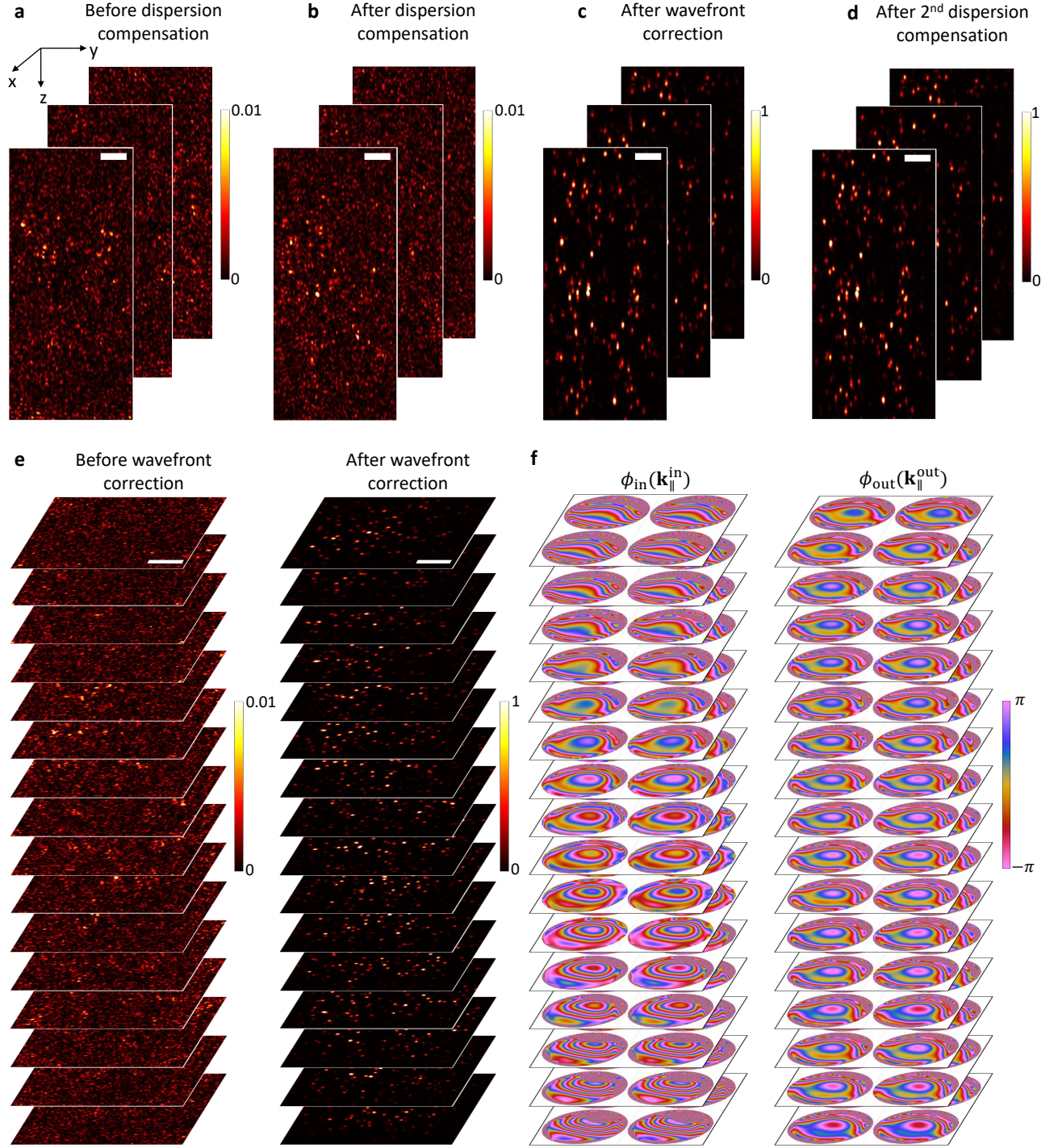
$$\bar{R}(\mathbf{r}_{\parallel}^{\text{out}}, \mathbf{r}_{\parallel}^{\text{in}}; z_j) \equiv \sum_{\mathbf{k}_{\parallel}^{\text{out}}} e^{i\mathbf{k}_{\parallel}^{\text{out}} \cdot \mathbf{r}_{\parallel}^{\text{out}}} \sum_{\mathbf{k}_{\parallel}^{\text{in}}} e^{-i\mathbf{k}_{\parallel}^{\text{in}} \cdot \mathbf{r}_{\parallel}^{\text{in}}} \tilde{R}(\mathbf{k}_{\parallel}^{\text{out}}, \mathbf{k}_{\parallel}^{\text{in}}; z_j), \quad (\text{S29})$$

set the matrix elements of $\bar{R}(\mathbf{r}_{\parallel}^{\text{out}}, \mathbf{r}_{\parallel}^{\text{in}}; z_j)$ outside the zone boundary to zero, and then Fourier transform back to the \mathbf{k}_{\parallel} basis before proceeding with the optimization. Doing so effectively prevents overfitting. In addition, since $\bar{R}(\mathbf{r}_{\parallel}^{\text{out}}, \mathbf{r}_{\parallel}^{\text{in}}; z_j)$ has been truncated to a smaller spatial region, we can use $\tilde{R}(\mathbf{k}_{\parallel}^{\text{out}}, \mathbf{k}_{\parallel}^{\text{in}}; z_j)$ with a larger angular spacing when we convert back to the \mathbf{k}_{\parallel} basis; doing so significantly reduces the computation time. Here, we set the input angular spacing and the output angular spacing of a divided zone both to $\delta k_x = \delta k_y = \sqrt{2}\pi/W_{\text{zone}}$ (slightly over-sampled above the Nyquist rate of $2\pi/W_{\text{zone}}$ but down-sampled compared to the original $\delta k = 2\pi/\text{FOV}$ spacing mentioned in Supplementary Sect. IC) where W_{zone} is the zone width. Note that the Zernike polynomials in Eq. (S27) can be evaluated at any set of angular grid points, so we can flexibly choose the angular spacing without affecting the optimization variables $\{c_n^{\text{in}}\}$ and $\{c_n^{\text{out}}\}$. This spatial-basis truncation and angular-basis down-sampling are only used during the optimization. We use the complete scattering matrix data for the image reconstruction (after the phase maps are determined).

As shown in Fig. 4h of the main text, the optimized wavefront correction patterns $\phi_{\text{in}}(\mathbf{k}_{\parallel}^{\text{in}})$ and $\phi_{\text{out}}(\mathbf{k}_{\parallel}^{\text{out}})$ exhibit faster oscillations at larger angles, corresponding to higher-order corrections. To assess the role of these large-angle higher-order corrections, we compare in **Supplementary Figs. 12** the SMT image with full-angle correction (top row) and with correction only for angles with $|\mathbf{k}_{\parallel}^{\text{in/out}}| > 0.3k_0$ (bottom row). We see that the fast-oscillation corrections at large angles provide significant image quality improvement.



Supplementary Fig. 12. Large-angle wavefront correction. SMT image with full-angle correction (top row) and with correction only for large angles (bottom row). In the latter case, the Zernike coefficients are reused from the first case but with $\phi_{\text{in/out}}(\mathbf{k}_{\parallel}^{\text{in/out}}) = 0$ for all $|\mathbf{k}_{\parallel}^{\text{in/out}}| < 0.3k_0$. Both wavefront-corrected images are divided into 8×8 zones, and we show the phase maps in the zone marked by a yellow dashed box. Scale bar: 10 μm .

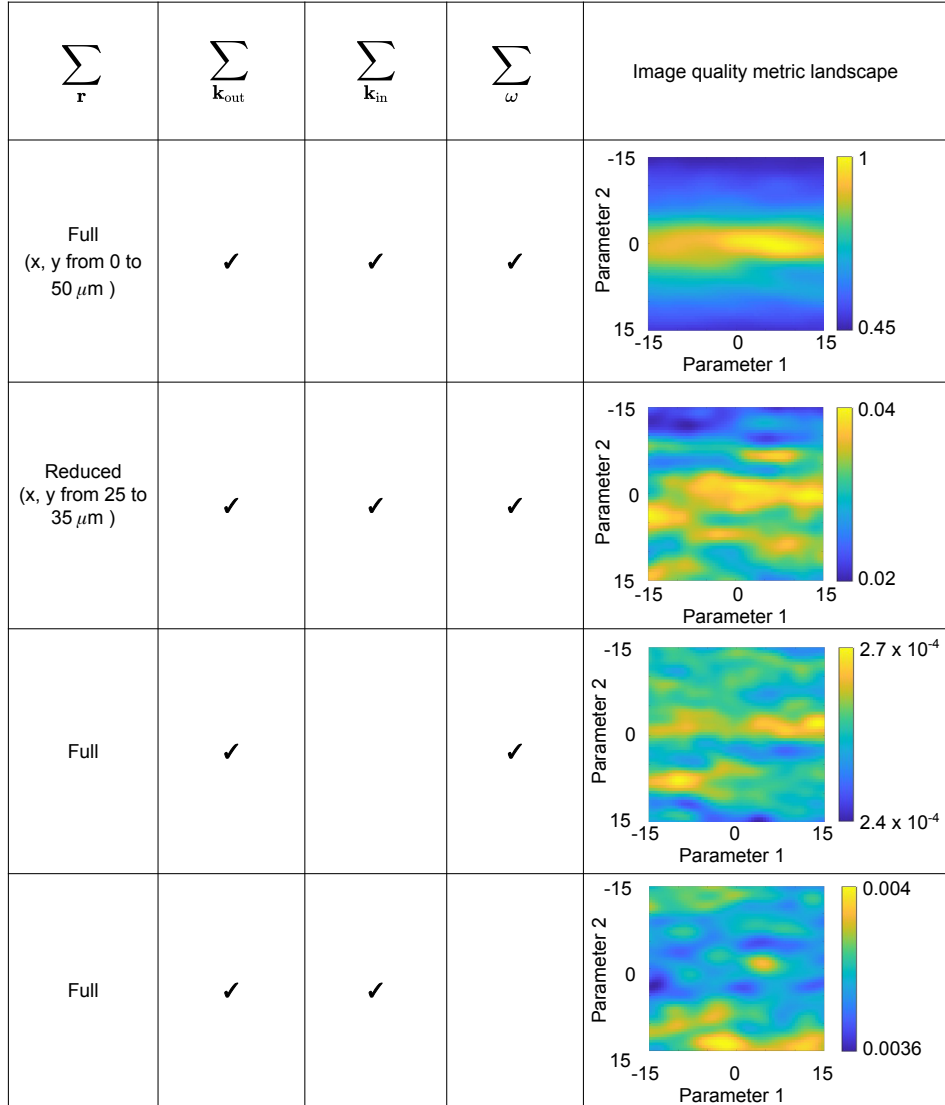


Supplementary Fig. 13. Volumetric dispersion compensation and wavefront correction for the nanoparticle colloid sample. **a–d**, YZ cross-section images at $x = 18$, 24 , and 30 μm before dispersion compensation (**a**), after dispersion compensation (**b**), after wavefront correction (**c**), and after the second dispersion compensation (**d**). **e**, XY *en face* images at $z = 1.476$, 1.483 , 1.490 , 1.496 , 1.502 , 1.509 , 1.515 , 1.522 , 1.528 , 1.535 , 1.541 , 1.548 , 1.554 , 1.561 , 1.567 , and 1.575 mm before and after wavefront correction. Scale bars: 10 μm . **f**, The corresponding input and output wavefront correction phase maps.

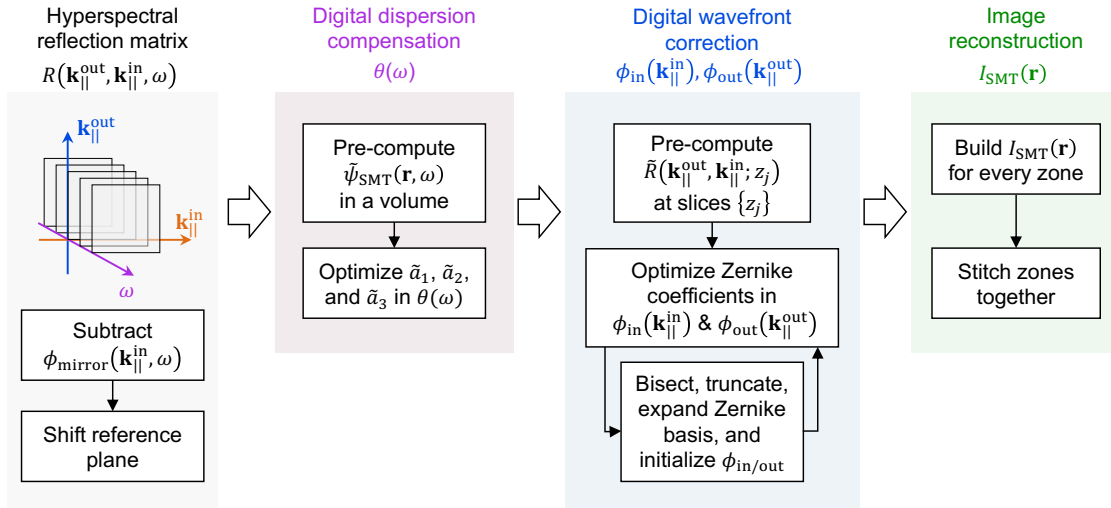
Supplementary Fig. 13 shows cross sections of the nanoparticle colloid sample before and after wavefront corrections and the associated phase maps. The images of the sub-volumes are stitched together similar to how the spatial zones in x - y are stitched. The aberrations are less severe in this sample, so we only use 11 radial orders of Zernike polynomials, dividing up to 2×2 zones. To maintain the axial resolution, after the wavefront correction, we optimize \tilde{a}_2 and \tilde{a}_3 in the dispersion compensation again for each sub-volume.

G. Metric landscape without the quadruple summation

Evaluation of the image quality metric M in Eq. (S20) [Eq. (3) of the main text] involves a quadruple summation: summation over space \mathbf{r} in Eq. (S20) and the triple gating through summations over \mathbf{k}_{out} , \mathbf{k}_{in} , and ω in the evaluation of I_{SMT} [Eq. (2) of the main text]. As discussed in the main text, all four of these summations are crucial in ensuring that the landscape of the image-quality metric reflects contributions from the target rather than from the multiple-scattering background or other unintended contributions. **Supplementary Fig. 14** shows the metric landscape as a function of two of the Zernike coefficients of $\phi_{\text{out}}(\mathbf{k}_{\text{out}})$ in the presence of the full quadruple summation and when one of the summations are skipped or reduced. We see that with the full quadruple summation, the metric landscape in this case exhibits only one local optima, so the outcome of the optimization is not sensitive to the initial guess. Without the quadruple summation, the landscape exhibits many local optima, and the optimization may end up in any of these local optima depending on the initial guess. The multitude of local optima arises because each speckle in the multiple-scattering background may be maximized by a different wavefront, unlike the target signals where all targets within the same isoplanatic patch share the same optimal wavefront.



Supplementary Fig. 14. Effect of the quadruple summation on the image metric landscape. The right-most column plots the image quality metric M of the USAF-target-under-tissue sample as a function of two Zernike coefficients of $\phi_{\text{out}}(\mathbf{k}_{\text{out}})$ when we perform the complete quadruple summation (top row), when we reduce the range of the spatial summation \mathbf{r} (second row), when we restrict to a single incident angle \mathbf{k}_{in} (third row), and when we restrict to a single frequency ω (bottom row) in the evaluation of M .



Supplementary Fig. 15. Flowchart for building SMT image with digital index-mismatch correction, dispersion compensation, and wavefront correction.

Supplementary Table 1. Time and memory usage of SMT dispersion compensation, wavefront correction, and image reconstruction. Each x - y slice covers $50 \times 50 \mu\text{m}^2$, with $0.7 \mu\text{m}$ grid spacing for optimization, $0.2 \mu\text{m}$ grid spacing for reconstruction. The precomputations refer to Eq. (S19), Eq. (S24), and the Zernike matrices in Eq. (S27). For the nanoparticle colloid, we perform dispersion compensation for the full volume together, wavefront correction for one sub-volume at a time (5 slices of $\{z_j\}$ per sub-volume).

Task		2D USAF target under tissue		3D nanoparticle colloid	
		Time (min)	Memory (GB)	Time (min)	Memory (GB)
Dispersion compensation	Data loading & precomputation	6.8	1.2	8.5	2.7
	Scan $\tilde{a}_1, \tilde{a}_3, \tilde{a}_3$	0.66		1.0	
	Gradient-based optimization	0.03		0.03	
Wavefront correction	Data loading & precomputation	5.0	0.2	8.7 (per sub-volume)	1.2
	1 x 1 zone	1	4.0	5.0 (per sub-volume)	6.2
	2 x 2 zones (all zones)	1.5		7.5 (per sub-volume)	
	4 x 4 zones (all zones)	1.0		N/A	
	8 x 8 zones (all zones)	1.6			
Image reconstruction	2D slice given precomputation	0.2		0.3	
	2D slice w/o precomputation	5.0	0.5	7.5	0.5
	3D volume w/o precomputation	N/A	N/A	280 (550 slices)	3.5

H. Digital correction flowchart

Supplementary Fig. 15 shows a flowchart of the digital correction and image reconstruction process.

I. Time usage and memory consumption

Supplementary Table 1 summarizes the time and memory usage for the digital dispersion compensation, wavefront correction, and image reconstruction. All tasks are performed using MATLAB on a personal laptop with an Intel Xeon E-2276M CPU with no GPU, 2×16 GB Dell DDR4 SODIMM 2666 MHz memory, and a KXG60ZNV512G Toshiba SSD. All data are stored and processed in the single-precision floating-point format.

IV. SYNTHESIS OF RCM, OCT, OCM/CASS, CAO-OCM, AND VRM IMAGES

Since the hyperspectral reflection matrix enables arbitrary virtual wavefront shaping, we can use it to synthesize other reflection-based imaging methods for comparison with SMT. Here, we describe the synthesis of reflectance confocal microscopy (RCM), optical coherence tomography (OCT), optical coherence microscopy (OCM), “collective accumulation of single scattering” (CASS) microscopy, computational adaptive optics OCM (CAO-OCM), and “volumetric reflection-matrix microscopy” (VRM).

A. RCM

RCM uses a single frequency $\omega = \omega_{\text{RCM}}$ with no time gating while spatially filtering both the incident and the reflected light with a high-NA objective lens [13]. Therefore, to synthesize an RCM image with index-mismatch correction, we use

$$I_{\text{RCM}}(\mathbf{r}) = \left| \sum_{\mathbf{k}_{\parallel}^{\text{out}}, \mathbf{k}_{\parallel}^{\text{in}}}^{\text{NA}=0.5} e^{i(\mathbf{k}_{\parallel}^{\text{sam}} - \mathbf{k}_{\parallel}^{\text{sam}}) \cdot \mathbf{r}} R(\mathbf{k}_{\parallel}^{\text{out}}, \mathbf{k}_{\parallel}^{\text{in}}, \omega = \omega_{\text{RCM}}) \right|^2, \quad (\text{S30})$$

with $R(\mathbf{k}_{\parallel}^{\text{out}}, \mathbf{k}_{\parallel}^{\text{in}}, \omega)$ defined in Eq. (S18b) and with $\mathbf{k}_{\parallel}^{\text{sam}}$ and $\mathbf{k}_{\parallel}^{\text{sam}}$ defined below Eq. (S6) and Eq. (S7). Note that, following Supplementary Sect. III B, the $R(\mathbf{k}_{\parallel}^{\text{out}}, \mathbf{k}_{\parallel}^{\text{in}}, \omega)$ here has already corrected for the dispersion and aberrations in the input path of the optical system. We use this version for the 3D nanoparticle colloid sample in Fig. 5 of the main text in order to compare the SMT and RCM images at the same depths.

Typically, the index mismatch is not corrected in RCM. To synthesize an RCM image without index-mismatch correction, we use

$$I_{\text{RCM}}(\mathbf{r}') = \left| \sum_{\mathbf{k}_{\parallel}^{\text{out}}, \mathbf{k}_{\parallel}^{\text{in}}}^{\text{NA}=0.5} e^{i(\mathbf{k}_{\parallel}^{\text{air}} - \mathbf{k}_{\parallel}^{\text{air}}) \cdot \mathbf{r}'} R'(\mathbf{k}_{\parallel}^{\text{out}}, \mathbf{k}_{\parallel}^{\text{in}}, \omega = \omega_{\text{RCM}}) \right|^2, \quad (\text{S31})$$

with $R'(\mathbf{k}_{\parallel}^{\text{out}}, \mathbf{k}_{\parallel}^{\text{in}}, \omega)$ being the sample reflection matrix after removing aberrations in the input path by subtracting $\Delta\phi_{\text{mirror}}(\mathbf{k}_{\parallel}^{\text{in}}, \omega)$ (see Supplementary Sect. III B) but before index-mismatch correction, which has its in-air reference plane at $z_{\text{ref}}^{\text{air}} = z_{\text{mirror}}$. Here, $\mathbf{r}' = (x, y, z')$, and $z' = z^{\text{air}} - z_{\text{ref}}^{\text{air}}$ is the apparent depth of the spatial focus looking from air relative to the reference plane in air. For the 2D USAF target under tissue sample in Fig. 4 of the main text, we use this version and choose $z' = z'_{\text{target}}$ to be the depth that maximizes the image intensity integrated over x - y .

B. OCT/OCM/CASS

For OCT and OCM, the spatial gate has its depth z_f fixed on the focal plane and is scanned in x and y . The z dimension of the image is mapped out through time/coherence gating. They have a limited depth of field because the strength of the spatial gate and the lateral resolution degrades when $|z - z_f|$ is larger than the Rayleigh range z_R .

We synthesize an OCM image with index-mismatch correction through

$$I_{\text{OCM}}(\mathbf{r}) = \left| \sum_{\omega} e^{i\theta_{\text{OCM}}(\omega) - 2i\omega\Delta t_f} \sum_{\mathbf{k}_{\parallel}^{\text{out}}, \mathbf{k}_{\parallel}^{\text{in}}}^{\text{NA}=0.5} e^{i(\mathbf{k}_{\parallel}^{\text{out}} - \mathbf{k}_{\parallel}^{\text{in}}) \cdot \mathbf{r}_f} R(\mathbf{k}_{\parallel}^{\text{out}}, \mathbf{k}_{\parallel}^{\text{in}}, \omega) \right|^2, \quad (\text{S32})$$

with $\mathbf{r} = (x, y, z)$, $\Delta t_f = n_{\text{sam}}(z - z_f)/c$ being the additional (or reduced) travel time to propagate from z_f to z in the sample, and $\mathbf{r}_f = (x, y, z_f)$ the location of the spatial gate. We perform the same dispersion compensation as in SMT (Supplementary Sect. III E) to determine the spectral phase correction $\theta_{\text{OCM}}(\omega)$. We use this version for the 3D nanoparticle colloid sample in Fig. 5 of the main text in order to compare the SMT and RCM images at the same depths.

Typically, the index mismatch is not corrected in OCM. To synthesize an OCM image without index-mismatch correction, we use

$$I_{\text{OCM}}(\mathbf{r}') = \left| \sum_{\omega} e^{i\theta_{\text{OCM}}(\omega) - 2i\omega\Delta t'_f} \sum_{\mathbf{k}_{\parallel}^{\text{out}}, \mathbf{k}_{\parallel}^{\text{in}}}^{\text{NA}=0.5} e^{i(\mathbf{k}_{\parallel}^{\text{out}} - \mathbf{k}_{\parallel}^{\text{in}}) \cdot \mathbf{r}'_f} R'(\mathbf{k}_{\parallel}^{\text{out}}, \mathbf{k}_{\parallel}^{\text{in}}, \omega) \right|^2, \quad (\text{S33})$$

with $\mathbf{r}' = (x, y, z')$, $z'_f = z_f^{\text{air}} - z_{\text{ref}}^{\text{air}}$ the apparent depth of the spatial gate relative to the in-air reference plane of the reflection matrix $R'(\mathbf{k}_{\parallel}^{\text{out}}, \mathbf{k}_{\parallel}^{\text{in}}, \omega)$, $\mathbf{r}'_f = (x, y, z'_f)$, and $\Delta t'_f = [n_{\text{glass}}h^{\text{glass}} + n_{\text{sam}}z - (h^{\text{glass}} + z_f^{\text{air}})]/c$ the additional (or reduced) travel time to propagate to z in the sample relative to propagating to the apparent depth z_f^{air} of the spatial gate in air (see **Supplementary Fig. 8**). For the 2D USAF target under tissue sample in Fig. 4 of the main text, we use this version and choose $z' = z'_f = z'_{\text{target}}$ to be the depth that maximizes the image intensity integrated over x - y .

To synthesize OCT images, we use a smaller NA = 0.1. For $\mathbf{k}_{\parallel}^{\text{in}}$ near the normal incidence, data points with $\mathbf{k}_{\parallel}^{\text{out}}$ near the normal incidence are excluded from our reflection matrix due to reflection from the objective lens (Supplementary Sect. I C). Therefore, for the synthesized OCT here, we use $\mathbf{k}_{\parallel}^{\text{in}}$ and $\mathbf{k}_{\parallel}^{\text{out}}$ within a disk with NA = 0.1 centered around angle $\alpha_{\text{in}} = \alpha_{\text{out}} = 10^\circ$. With index-mismatch correction, we have

$$I_{\text{OCT}}(\mathbf{r}) = \left| \sum_{\omega} e^{i\theta_{\text{OCT}}(\omega) - i\omega\Delta t_f \left(\frac{1}{\cos\alpha_{\text{in}}} + \frac{1}{\cos\alpha_{\text{out}}} \right)} \sum_{\mathbf{k}_{\parallel}^{\text{out}}}^{\text{NA}=0.1, \alpha_{\text{out}}} \sum_{\mathbf{k}_{\parallel}^{\text{in}}}^{\text{NA}=0.1, \alpha_{\text{in}}} e^{i(\mathbf{k}_{\parallel}^{\text{out}} - \mathbf{k}_{\parallel}^{\text{in}}) \cdot \mathbf{r}_f} R(\mathbf{k}_{\parallel}^{\text{out}}, \mathbf{k}_{\parallel}^{\text{in}}, \omega) \right|^2. \quad (\text{S34})$$

Similar to OCM, we build OCT images without index-mismatch correction with

$$I_{\text{OCT}}(\mathbf{r}') = \left| \sum_{\omega} e^{i\theta_{\text{OCT}}(\omega) - i\omega\Delta t'_f \left(\frac{1}{\cos\alpha_{\text{in}}} + \frac{1}{\cos\alpha_{\text{out}}} \right)} \sum_{\mathbf{k}_{\parallel}^{\text{out}}}^{\text{NA}=0.1, \alpha_{\text{out}}} \sum_{\mathbf{k}_{\parallel}^{\text{in}}}^{\text{NA}=0.1, \alpha_{\text{in}}} e^{i(\mathbf{k}_{\parallel}^{\text{out}} - \mathbf{k}_{\parallel}^{\text{in}}) \cdot \mathbf{r}'_f} R'(\mathbf{k}_{\parallel}^{\text{out}}, \mathbf{k}_{\parallel}^{\text{in}}, \omega) \right|^2. \quad (\text{S35})$$

In the ‘‘collective accumulation of single-scattering’’ (CASS) microscopy [14], the time-gated reflection matrix at one focal plane $z = z_f$ is measured using a pulsed laser. The time-gated reflection matrix $\tilde{\tilde{R}}(\mathbf{k}_{\parallel}^{\text{out}}, \mathbf{k}_{\parallel}^{\text{in}}; t_f)$ at arrival time t_f is related to the frequency-dependent reflection matrix through [15]

$$\tilde{\tilde{R}}(\mathbf{k}_{\parallel}^{\text{out}}, \mathbf{k}_{\parallel}^{\text{in}}; t_f) = \sum_{\omega} f(\omega) e^{-i\omega t} R(\mathbf{k}_{\parallel}^{\text{out}}, \mathbf{k}_{\parallel}^{\text{in}}, \omega), \quad (\text{S36})$$

where $f(\omega)$ is the field spectrum of the incident pulse. Comparing this to the synthetic time-gated reflection matrix $\tilde{R}(\mathbf{k}_{\parallel}^{\text{out}}, \mathbf{k}_{\parallel}^{\text{in}}; z_j)$ we defined earlier in Eq. (S24), we see that $\tilde{\tilde{R}}(\mathbf{k}_{\parallel}^{\text{out}}, \mathbf{k}_{\parallel}^{\text{in}}; t_f) \approx \tilde{R}(\mathbf{k}_{\parallel}^{\text{out}}, \mathbf{k}_{\parallel}^{\text{in}}; z_j = z_f)$ if we ignore the dispersion compensation $\theta(\omega)$ in $\tilde{R}(\mathbf{k}_{\parallel}^{\text{out}}, \mathbf{k}_{\parallel}^{\text{in}}; z_j)$ and set the reference plane at $z_j = z_f = 0$ and $t = 0$.

In CASS, matrix elements with the same in-plane momentum difference $\Delta\mathbf{k}_{\parallel} = \mathbf{k}_{\parallel}^{\text{out}} - \mathbf{k}_{\parallel}^{\text{in}}$, denoted as \mathbf{k}^s in Ref. [14], are summed over to accumulate the single-scattering contribution. Then, an inverse Fourier transform is performed to go from the momentum space $\Delta\mathbf{k}_{\parallel}$ to the real space \mathbf{r}_{\parallel} to produce an image on the focal plane:

$$I_{\text{CASS}}(\mathbf{r}_{\parallel}) = \left| \sum_{\Delta\mathbf{k}_{\parallel}} e^{i\Delta\mathbf{k}_{\parallel} \cdot \mathbf{r}_{\parallel}} \left[\sum_{\mathbf{k}_{\parallel}^{\text{in}}} \tilde{\tilde{R}}(\mathbf{k}_{\parallel}^{\text{in}} + \Delta\mathbf{k}_{\parallel}, \mathbf{k}_{\parallel}^{\text{in}}; t_f) \right] \right|^2. \quad (\text{S37})$$

By treating $\tilde{\tilde{R}}(\mathbf{k}_{\parallel}^{\text{out}}, \mathbf{k}_{\parallel}^{\text{in}}; t_f) \approx \tilde{R}(\mathbf{k}_{\parallel}^{\text{out}}, \mathbf{k}_{\parallel}^{\text{in}}; z_j = z_f)$, inserting the definition of $\tilde{R}(\mathbf{k}_{\parallel}^{\text{out}}, \mathbf{k}_{\parallel}^{\text{in}}; z_j)$ from Eq. (S24), and comparing to Eq. (S32), we can see that the CASS image equals the OCM image on the focal plane,

$$I_{\text{CASS}}(\mathbf{r}_{\parallel}) \approx I_{\text{OCM}}(\mathbf{r}_{\parallel}, z_f). \quad (\text{S38})$$

In the frequency-domain OCM images we synthesize, we have removed the dispersion and aberrations in the input path of the optical system by subtracting $\Delta\phi_{\text{mirror}}(\mathbf{k}_{\parallel}^{\text{in}}, \omega)$ (see Supplementary Sect. III B) and additionally compensated for the sample dispersion (Supplementary Sect. III E). A CASS image does not come with these corrections, so it would have a lower quality than the OCM image we synthesize.

C. CAO-OCM

The interferometric measurement of OCT and OCM provides phase information that can be used for digital aberration correction [16–21]. However, the correction only applies to the phase image itself; it cannot apply separately to the input spatial gate and the output spatial gate since OCT/OCM does not measure the reflection matrix. In this section, we consider computational adaptive optics (CAO) corrections onto the confocal OCM image, referred to as CAO-OCM [16–19]. CAO for full-field OCT without input spatial gate [20, 21] has a lower performance due to the lack of confocal gating, which will be considered later as a limiting case of SMT in Supplementary Sect. VI.

We start by synthesizing the phase image of OCM with index-mismatch correction and dispersion compensation, from Eq. (S32), at the focal plane $z = z_f$,

$$\psi_{\text{OCM}}(\mathbf{r}_{\parallel}; z_f) = \sum_{\omega} e^{i\theta_{\text{OCM}}(\omega)} \sum_{\mathbf{k}_{\parallel}^{\text{out}}, \mathbf{k}_{\parallel}^{\text{in}}} e^{i(\mathbf{k}_{\parallel}^{\text{out}} - \mathbf{k}_{\parallel}^{\text{in}}) \cdot \mathbf{r}_{\parallel}} R(\mathbf{k}_{\parallel}^{\text{out}}, \mathbf{k}_{\parallel}^{\text{in}}, \omega). \quad (\text{S39})$$

In CAO-OCM, the aberrations are corrected in the reciprocal space [16–19], $\mathbf{q}_{\parallel} = \mathbf{k}_{\parallel}^{\text{out}} - \mathbf{k}_{\parallel}^{\text{in}}$. So, we consider the 2D Fourier transform of the phase image, $\tilde{\psi}_{\text{OCM}}(\mathbf{q}_{\parallel}; z_f) = \sum_{\mathbf{r}_{\parallel}} e^{-i\mathbf{q}_{\parallel} \cdot \mathbf{r}_{\parallel}} \psi_{\text{OCM}}(\mathbf{r}_{\parallel}; z_f)$. After applying phase correction $e^{i\phi(\mathbf{q}_{\parallel})}$, the image is inverse Fourier transformed back to the real space

$$\psi_{\text{CAO}}(\mathbf{r}_{\parallel}; z_f) = \sum_{\mathbf{q}_{\parallel}} e^{i\mathbf{q}_{\parallel} \cdot \mathbf{r}_{\parallel} + i\phi(\mathbf{q}_{\parallel})} \tilde{\psi}_{\text{OCM}}(\mathbf{q}_{\parallel}; z_f) \quad (\text{S40})$$

to form the corrected image $I_{\text{CAO}}(\mathbf{r}_{\parallel}; z_f) = |\psi_{\text{CAO}}(\mathbf{r}_{\parallel}; z_f)|^2$.

To determine the phase correction $\phi(\mathbf{q}_{\parallel})$, we follow the same strategy as in Supplementary Sect. III F, expanding it in Zernike polynomials like in Eq. (S27),

$$\phi(\mathbf{q}_{\parallel}) = \sum_n c_n Z_n \left(\frac{\mathbf{q}_{\parallel}}{2k_0^{\text{maxNA}}} \right), \quad (\text{S41})$$

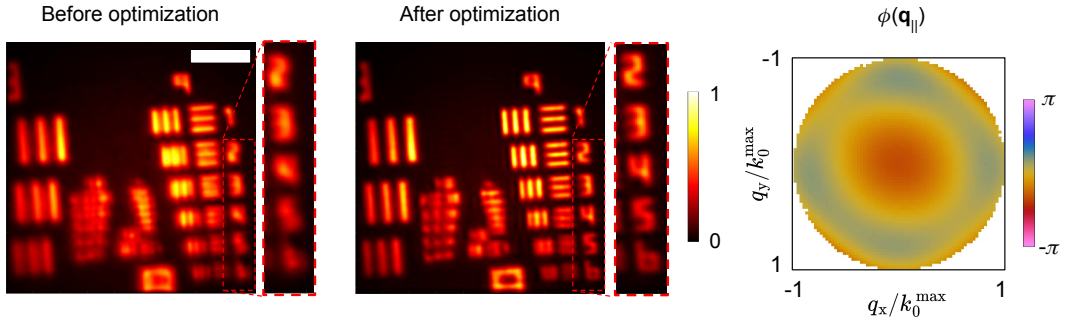
with $k_0^{\text{max}} = \omega_{\text{max}}/c$. The Zernike coefficients $\{c_n\}$ are then determined by maximizing the same image quality metric $M = \sum_{\mathbf{r}} I_{\text{CAO}}(\mathbf{r}) \ln [I_{\text{CAO}}(\mathbf{r})/I_0]$ using the same L-BFGS algorithm with initial guess $c_n = 0$. Here, the gradient of M with respect to $\{c_n\}$ is

$$\frac{\partial M}{\partial c_n} = -2 \sum_{\mathbf{r}_{\parallel}, \mathbf{q}_{\parallel}} \text{Im} \left\{ \left[1 + \ln \frac{I_{\text{CAO}}(\mathbf{r}_{\parallel}; z_f)}{I_0} \right] \psi_{\text{CAO}}^*(\mathbf{r}_{\parallel}; z_f) \tilde{\psi}_{\text{OCM}}(\mathbf{q}_{\parallel}; z_f) e^{i\mathbf{q}_{\parallel} \cdot \mathbf{r}_{\parallel} + i\phi(\mathbf{q}_{\parallel})} \right\} Z_n \left(\frac{\mathbf{q}_{\parallel}}{2k_0^{\text{maxNA}}} \right). \quad (\text{S42})$$

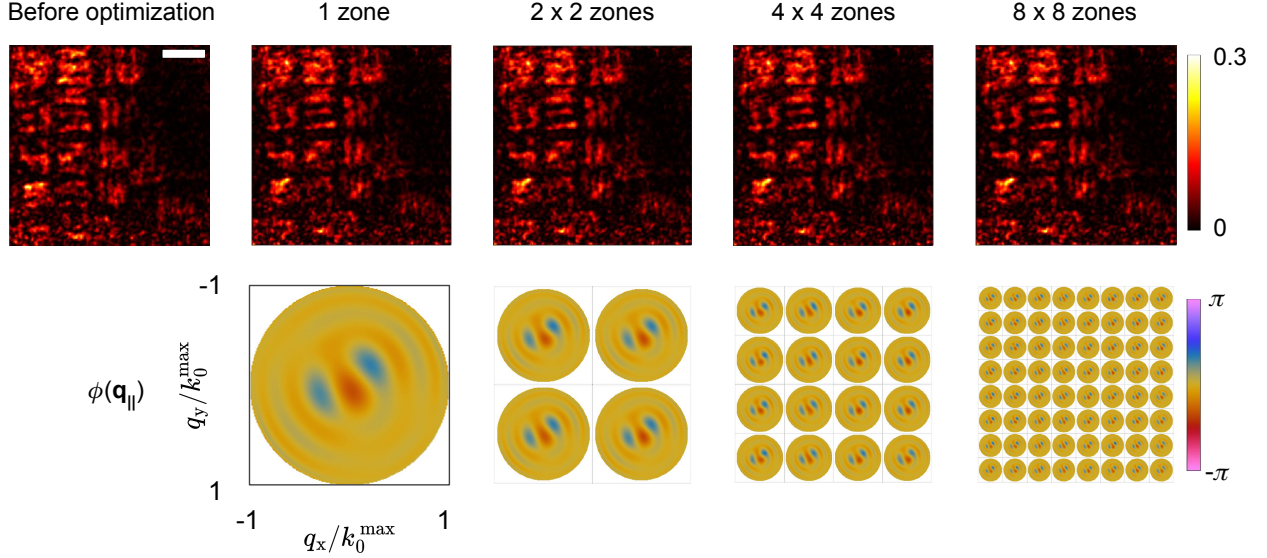
We adopt the same progressive bisection strategy as described in Supplementary Sect. III F, gradually dividing the FOV into smaller zones while increasing the number of Zernike polynomials per zone and truncating $\psi_{\text{CAO}}(\mathbf{r}_{\parallel}; z_f)$ to within the target zone.

To validate our implementation of CAO-OCM, we first test it on a bare USAF target not covered by any scattering medium. Before the CAO-OCM optimization, the aberrations in the input path of the optical system are already removed by subtracting $\Delta\phi_{\text{mirror}}(\mathbf{k}_{\parallel}^{\text{in}}, \omega)$ (Supplementary Sect. III B), but there are still weak aberrations in the output path, which is visible when we image group 9 of the USAF target with a reduced NA of 0.25. As shown in **Supplementary Figs. 16**, CAO-OCM successfully removes these low-order aberrations and improves the image quality. Progressive bisection is not necessary since the isoplanatic patch size of these low-order aberrations is very large.

Next, we test CAO-OCM for the USAF target under mouse brain sample considered in the main text. **Supplementary Fig. 17** shows the CAO-OCM images and the corresponding phase correction maps during the progressive optimization. We use the same focal depth $z_f = 977.5 \mu\text{m}$, the same number of Zernike polynomials, and the same momentum spacing δq as in **Supplementary Figs. 10**. Despite applying all of these strategies and allowing up to 275 Zernike polynomials per zone, the optimization only identified some low-order aberrations, with no significant improvement to the image. This is because (1) prior to this optimization, the low-order aberrations in the input path of the optical system have already been removed through a calibration mirror (Supplementary Sect. III B), and (2) double-path wavefront correction is crucial for the high-order terms [19] but is not possible with CAO-OCM.



Supplementary Fig. 16. Validation of OCM corrected with computational adaptive optics (CAO-OCM). The sample is a USAF target in air, not covered by any scattering medium. Scale bar: 10 μm .



Supplementary Fig. 17. CAO-OCM images of USAF target under 1-mm of mouse brain tissue. The same progressive optimization as in SMT is applied. The bottom row shows the corresponding phase correction maps in the reciprocal space \mathbf{q}_{\parallel} . Only some low-order variations get corrected despite allowing up to 275 Zernike polynomials per zone because the high-order wavefront distortions can only be corrected separately through $\phi_{\text{in}}(\mathbf{k}_{\parallel}^{\text{in}})$ and $\phi_{\text{out}}(\mathbf{k}_{\parallel}^{\text{out}})$. Scale bar: 10 μm .

D. Volumetric reflection-matrix microscopy (VRM)

Here we detail our implementation of the VRM method [22], present analyses that reveal the quantities that VRM implicitly maximizes, and compare the VRM method to the SMT method.

1. VRM spectral dispersion compensation

The very first step of VRM is to “minimize defocus error” through “a numerical propagation to the depth with the maximum reflectance (z_{max})” [22]:

$$R_{\text{max}}(\mathbf{k}_{\parallel}^{\text{out}}, \mathbf{k}_{\parallel}^{\text{in}}, \omega) \equiv R(\mathbf{k}_{\parallel}^{\text{out}}, \mathbf{k}_{\parallel}^{\text{in}}, \omega) e^{i(k_z^{\text{out}} - k_z^{\text{in}})z_{\text{max}}}. \quad (\text{S43})$$

Doing so places the reference plane of the reflection matrix at z_{max} . This step is only mentioned on page 5 of the Supplementary Materials of Ref. [22], but it is important because our analysis below shows that the VRM dispersion compensation implicitly maximizes the image brightness at this particular depth z_{max} . To find the “maximum reflectance,” we build the volumetric SMT image without corrections using Eq. (1) of the main text, and choose z_{max} to be the depth where the x - y -integrated image intensity is the largest. We start with inclusion of the index-mismatch

correction, so the $R(\mathbf{k}_{\parallel}^{\text{out}}, \mathbf{k}_{\parallel}^{\text{in}}, \omega)$ in Eq. (S43) is the corrected one defined in Eq. (S18b), the k_z^{in} and k_z^{out} in Eq. (S43) are abbreviations of $k_{z,\text{in}}^{\text{sam}}$ and $k_{z,\text{out}}^{\text{sam}}$, and the \mathbf{k}_{out} and \mathbf{k}_{in} below are abbreviations of $\mathbf{k}_{\text{out}}^{\text{sam}}$ and $\mathbf{k}_{\text{in}}^{\text{sam}}$.

VRM then uses an iterative phase conjugation scheme to estimate the spectro-angular dispersion $\phi_{\text{in}}(\mathbf{k}_{\parallel}^{\text{in}}, \omega)$ and $\phi_{\text{out}}(\mathbf{k}_{\parallel}^{\text{out}}, \omega)$ relative to the center frequency ω_c . At the n -th iteration, a compensation of $-\Delta\phi_{\text{in}}^{(n)}(\mathbf{k}_{\parallel}^{\text{in}}, \omega)$ and $-\Delta\phi_{\text{out}}^{(n)}(\mathbf{k}_{\parallel}^{\text{out}}, \omega)$ is applied onto the columns and rows of the reflection matrix,

$$R^{(n+1)}(\mathbf{k}_{\parallel}^{\text{out}}, \mathbf{k}_{\parallel}^{\text{in}}, \omega) = e^{-i\Delta\phi_{\text{out}}^{(n)}(\mathbf{k}_{\parallel}^{\text{out}}, \omega)} R^{(n)}(\mathbf{k}_{\parallel}^{\text{out}}, \mathbf{k}_{\parallel}^{\text{in}}, \omega) e^{-i\Delta\phi_{\text{in}}^{(n)}(\mathbf{k}_{\parallel}^{\text{in}}, \omega)}, \quad (\text{S44})$$

with $n = 0, 1, 2, \dots$ and with initial condition

$$\begin{aligned} R^{(0)}(\mathbf{k}_{\parallel}^{\text{out}}, \mathbf{k}_{\parallel}^{\text{in}}, \omega) &= R_{\text{max}}(\mathbf{k}_{\parallel}^{\text{out}}, \mathbf{k}_{\parallel}^{\text{in}}, \omega), \\ \Delta\phi_{\text{in}}^{(0)}(\mathbf{k}_{\parallel}^{\text{in}}, \omega) &= \Delta\phi_{\text{out}}^{(0)}(\mathbf{k}_{\parallel}^{\text{out}}, \omega) = 0. \end{aligned} \quad (\text{S45})$$

The compensation at the n -th iteration is determined by phase conjugation,

$$\Delta\phi_{\text{in}}^{(n)}(\mathbf{k}_{\parallel}^{\text{in}}, \omega) = \arg \left[\sum_{\mathbf{k}_{\parallel}^{\text{out}}} R^{(n)}(\mathbf{k}_{\parallel}^{\text{out}}, \mathbf{k}_{\parallel}^{\text{in}}, \omega) R^{(n)*}(\mathbf{k}_{\parallel}^{\text{out}}, \mathbf{k}_{\parallel}^{\text{in}}, \omega_c) \right], \quad (\text{S46})$$

$$\Delta\phi_{\text{out}}^{(n)}(\mathbf{k}_{\parallel}^{\text{out}}, \omega) = \arg \left[\sum_{\mathbf{k}_{\parallel}^{\text{in}}} R^{(n)}(\mathbf{k}_{\parallel}^{\text{out}}, \mathbf{k}_{\parallel}^{\text{in}}, \omega) R^{(n)*}(\mathbf{k}_{\parallel}^{\text{out}}, \mathbf{k}_{\parallel}^{\text{in}}, \omega_c) \right]. \quad (\text{S47})$$

Here, we iterate to the N_{dc} -th iteration, until $|\Delta\phi_{\text{in}}^{(n)}(\mathbf{k}_{\parallel}^{\text{in}}, \omega)|$ and $|\Delta\phi_{\text{out}}^{(n)}(\mathbf{k}_{\parallel}^{\text{out}}, \omega)|$ are both smaller than 10° for every pair of $(\mathbf{k}_{\parallel}^{\text{in}}, \omega)$ and every pair of $(\mathbf{k}_{\parallel}^{\text{out}}, \omega)$. The reflection matrix after the VRM dispersion compensation (dc) is then

$$R_{\text{dc}}(\mathbf{k}_{\parallel}^{\text{out}}, \mathbf{k}_{\parallel}^{\text{in}}, \omega) \equiv R^{(N_{\text{dc}}+1)}(\mathbf{k}_{\parallel}^{\text{out}}, \mathbf{k}_{\parallel}^{\text{in}}, \omega) = e^{-i\phi_{\text{out}}(\mathbf{k}_{\parallel}^{\text{out}}, \omega)} R_{\text{max}}(\mathbf{k}_{\parallel}^{\text{out}}, \mathbf{k}_{\parallel}^{\text{in}}, \omega) e^{-i\phi_{\text{in}}(\mathbf{k}_{\parallel}^{\text{in}}, \omega)}, \quad (\text{S48})$$

where $\phi_{\text{in}}(\mathbf{k}_{\parallel}^{\text{in}}, \omega) = \sum_{n=1}^{N_{\text{dc}}} \Delta\phi_{\text{in}}^{(n)}(\mathbf{k}_{\parallel}^{\text{in}}, \omega)$ and $\phi_{\text{out}}(\mathbf{k}_{\parallel}^{\text{out}}, \omega) = \sum_{n=1}^{N_{\text{dc}}} \Delta\phi_{\text{out}}^{(n)}(\mathbf{k}_{\parallel}^{\text{out}}, \omega)$. Note we can see from Eq. (S46)–(S47) that $\phi_{\text{in}}(\mathbf{k}_{\parallel}^{\text{in}}, \omega_c) = \phi_{\text{out}}(\mathbf{k}_{\parallel}^{\text{out}}, \omega_c) = 0$ at the center frequency throughout the iterations.

These VRM dispersion compensation steps are very different from the SMT dispersion compensation steps described in Supplementary Sect. III E. To facilitate comparison and to gain insights into VRM, here we identify the objective functions that the VRM dispersion compensation implicitly maximizes. Define

$$M_{\text{in}}^{\text{VRM}}(\mathbf{k}_{\parallel}^{\text{in}}, \omega) \equiv \sum_{\mathbf{r} \in z_{\text{max}}} I_{\text{in}}(\mathbf{r}, \mathbf{k}_{\parallel}^{\text{in}}, \omega), \quad M_{\text{out}}^{\text{VRM}}(\mathbf{k}_{\parallel}^{\text{out}}, \omega) \equiv \sum_{\mathbf{r} \in z_{\text{max}}} I_{\text{out}}(\mathbf{r}, \mathbf{k}_{\parallel}^{\text{out}}, \omega), \quad (\text{S49})$$

where $\sum_{\mathbf{r} \in z_{\text{max}}}$ denotes $\mathbf{r} = (x, y, z_{\text{max}})$ with summations over x and y in the FOV while fixing the depth at z_{max} . Here,

$$I_{\text{in}}(\mathbf{r}, \mathbf{k}_{\parallel}^{\text{in}}, \omega') \equiv \left| \sum_{\omega=\omega', \omega_c} \sum_{\mathbf{k}_{\parallel}^{\text{out}}} e^{i(\mathbf{k}_{\text{out}} - \mathbf{k}_{\text{in}}) \cdot \mathbf{r} - i\phi_{\text{out}}(\mathbf{k}_{\parallel}^{\text{out}}, \omega) - i\phi_{\text{in}}(\mathbf{k}_{\parallel}^{\text{in}}, \omega)} R(\mathbf{k}_{\text{out}}, \mathbf{k}_{\text{in}}, \omega) \right|^2, \quad (\text{S50})$$

$$I_{\text{out}}(\mathbf{r}, \mathbf{k}_{\parallel}^{\text{out}}, \omega') \equiv \left| \sum_{\omega=\omega', \omega_c} \sum_{\mathbf{k}_{\parallel}^{\text{in}}} e^{i(\mathbf{k}_{\text{out}} - \mathbf{k}_{\text{in}}) \cdot \mathbf{r} - i\phi_{\text{out}}(\mathbf{k}_{\parallel}^{\text{out}}, \omega) - i\phi_{\text{in}}(\mathbf{k}_{\parallel}^{\text{in}}, \omega)} R(\mathbf{k}_{\text{out}}, \mathbf{k}_{\text{in}}, \omega) \right|^2. \quad (\text{S51})$$

By substituting Eq. (S43) into Eqs. (S49)–(S50), using Parseval's theorem, and taking the derivative, we see that

$$\frac{\partial M_{\text{in}}^{\text{VRM}}}{\partial \phi_{\text{in}}(\mathbf{k}_{\parallel}^{\text{in}}, \omega)} \propto \text{Im} \left[\sum_{\mathbf{k}_{\parallel}^{\text{out}}} R_{\text{dc}}(\mathbf{k}_{\parallel}^{\text{out}}, \mathbf{k}_{\parallel}^{\text{in}}, \omega) R_{\text{dc}}^*(\mathbf{k}_{\parallel}^{\text{out}}, \mathbf{k}_{\parallel}^{\text{in}}, \omega_c) \right]. \quad (\text{S52})$$

When the VRM dispersion compensation converges, $\Delta\phi_{\text{in}}^{(N)}(\mathbf{k}_{\parallel}^{\text{in}}, \omega) \approx 0$, so the term inside the square brackets of Eq. (S46) is purely real, and $\frac{\partial M_{\text{in}}^{\text{VRM}}}{\partial \phi_{\text{in}}(\mathbf{k}_{\parallel}^{\text{in}}, \omega)} \approx 0$. We can similarly show that $\frac{\partial M_{\text{out}}^{\text{VRM}}}{\partial \phi_{\text{out}}(\mathbf{k}_{\parallel}^{\text{out}}, \omega)} \approx 0$ when VRM converges.

Therefore, we conclude that the iterative phase conjugation of VRM dispersion compensation reaches a local maximum of $M_{\text{in}}^{\text{VRM}}(\mathbf{k}_{\parallel}^{\text{in}}, \omega)$ and $M_{\text{out}}^{\text{VRM}}(\mathbf{k}_{\parallel}^{\text{out}}, \omega)$ in Eq. (S49) for all $\mathbf{k}_{\parallel}^{\text{in}}, \mathbf{k}_{\parallel}^{\text{out}}, \omega$. Note this analysis is new and was not carried out in Ref. [22].

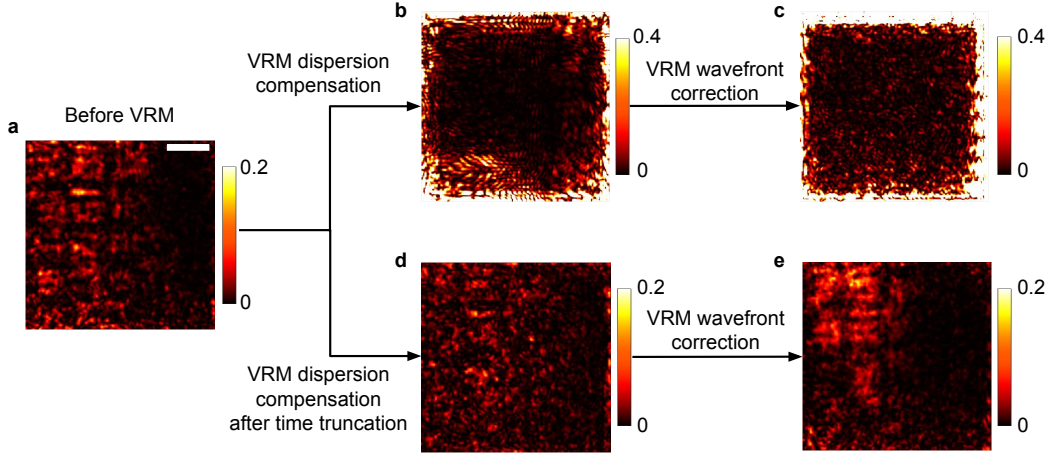
This analysis allows direct comparison between the VRM dispersion compensation above and the SMT dispersion compensation of Supplementary Sect. III E. We see four major differences:

1. To avoid overfitting and to alleviate the curse of dimensionality in an optimization problem, SMT employs only three variables for dispersion compensation: $\tilde{a}_1, \tilde{a}_2, \tilde{a}_3$, each having a physical meaning (group velocity, group velocity dispersion, and asymmetric pulse distortion). Meanwhile, VRM uses $\phi_{\text{in}}(\mathbf{k}_{\parallel}^{\text{in}}, \omega)$ and $\phi_{\text{out}}(\mathbf{k}_{\parallel}^{\text{out}}, \omega)$ as free variables for every pair of $(\mathbf{k}_{\parallel}^{\text{in}}, \omega)$ and every pair of $(\mathbf{k}_{\parallel}^{\text{out}}, \omega)$.
2. The spatial summation of SMT dispersion compensation in Eq. (S20) sums over a 3D volume, which avoids overfitting. The spatial summation of VRM dispersion compensation in Eq. (S49) sums over a 2D slice at a single depth z_{max} , which can create serious artifacts. This is the reason that the volumetric VRM image in Fig. 5 of the main text shows bright slices, with each slice being the z_{max} of that sub-volume.
3. The SMT image (I_{SMT} , defined in Eq. (2) of the main text) used in the SMT objective function of Eq. (S20) employs both input spatial gating (through a summation over \mathbf{k}_{in}) and output spatial gating (through a summation over \mathbf{k}_{out}). The confocal spatial gate is crucial for the optimization, as shown in **Supplementary Fig. 14**. Meanwhile, the I_{in} and I_{out} of Eqs. (S50)–(S51) used in the VRM dispersion compensation drops one of the two spatial gates, which reduces its ability to suppress multiple scattering and other undesired signals.
4. The SMT image I_{SMT} used in the SMT dispersion compensation also employees temporal gating through a summation over all frequencies ω . The temporal gate is crucial for the optimization, as shown in **Supplementary Fig. 14**. The VRM frequency summation in Eqs. (S50)–(S51) only sums over two frequencies, ω' and ω_c , so the temporal gate is gone, which further reduces its ability to suppress multiple scattering and other undesired signals.

Also, with the SMT dispersion compensation, we pre-compute the angular summations over \mathbf{k}_{in} and \mathbf{k}_{out} in Eq. (S19), which makes the SMT dispersion compensation much faster than the VRM dispersion compensation. For the nanoparticle colloid sample here, the SMT dispersion compensation took less than 10 minutes for the full volume (across the 110 μm depth of field), while the VRM dispersion compensation took around 2 hours per sub-volume (32 hours in total for the full volume).

In our tests, we find the VRM dispersion compensation to work reasonably well with high-contrast planar targets in a weakly scattering system, such as a USAF target in air or under a thin layer of tissue. However, for the strongly scattering systems we consider in the main text, the VRM dispersion compensation introduces very bright artifacts on the edges of the image (**Supplementary Fig. 18b**). We observe the same behavior with VRM when using a reflection matrix measured without any sample. This is because instead of maximizing the signal from the intended targets, VRM maximizes the signal from the objective lens reflection. Recall that after triple gating and after we exclude the peak of the objective lens signal from the reflection matrix data (Supplementary Sect. I C), the sensitivity of $I_{\text{SMT}}(\mathbf{r})$ is still limited by the residual reflection from the objective lens (Supplementary Sect. II C). Since the objective lens lies at depths very far away from the sample (but still within the coherence length of the laser), the most effective way to filter out the objective lens reflection is time gating. But the $I_{\text{in}}(\mathbf{r}, \mathbf{k}_{\parallel}^{\text{in}}, \omega')$ and $I_{\text{out}}(\mathbf{r}, \mathbf{k}_{\parallel}^{\text{out}}, \omega')$ that the VRM dispersion compensation maximizes only use two frequencies (ω' and ω_c) with no time gating, so the objective lens signal dominates over the weak target signal in $I_{\text{in}}(\mathbf{r}, \mathbf{k}_{\parallel}^{\text{in}}, \omega')$ and $I_{\text{out}}(\mathbf{r}, \mathbf{k}_{\parallel}^{\text{out}}, \omega')$ and is maximized by VRM. This may not be as much of an issue in Ref. [22], which used lasers with much shorter coherence lengths and considered samples dominated by the aberrations (namely, single scattering) of a thin plastic layer rather than the multiple scattering from a volumetric medium. To improve the VRM performance, here we suppress the objective lens signal by incorporating a coarse temporal gate prior to the VRM dispersion compensation. We do so by (1) shifting the reference plane of the reflection matrix to the center of a truncation volume [same as Eq. (S43) but to the center of the truncation volume instead], (2) perform a non-uniform discrete Fourier transform to convert the reflection matrix data from frequency domain ω to time domain t , (3) perform another non-uniform discrete Fourier transform to convert from time domain t back to frequency domain ω , and (4) shift the reference plane of the reflection matrix back. In time domain, we only use the values of t within the truncation volume, which sets the coarse temporal gate. As shown in **Supplementary Fig. 18d**, this “temporal truncation” suppresses the objective-lens contributions in the reflection matrix data and prevents the VRM dispersion compensation from maximizing the objective lens signal. However, the performance of VRM is still substantially worse than SMT due to the four differences described above.

For the 3D nanoparticle colloid sample, we perform the first SMT dispersion compensation simultaneously over the full 110 μm depth of field, $z \in [1470, 1580] \mu\text{m}$, to avoid overfitting. However, simultaneous dispersion compensation over such a large volume is not possible with VRM: when the temporal truncation spans such a large volume, there



Supplementary Fig. 18. Evolution of the VRM image of the USAF target under tissue without and with temporal truncation. Scale bar: 10 μm .

is not enough suppression of the objective lens signal (since the VRM dispersion compensation itself has no temporal gate), and the VRM dispersion compensation always maximizes the objective lens signal instead. So, here we divide the 110 μm depth of field into 16 overlapping sub-volumes (same as in the SMT wavefront correction) and perform VRM separately for each sub-volume (both dispersion compensation and wavefront correction), each with its temporal truncation. The final images of the sub-volumes are then stitched together, same as in SMT.

2. VRM angular wavefront correction and reconstruction

After estimating the spectro-angular dispersion relative to the center frequency ω_c , VRM performs another iterative phase conjugation to estimate the angular wavefront distortion $\phi_{\text{in}}(\mathbf{k}_{\parallel}^{\text{in}}, \omega_c)$ and $\phi_{\text{out}}(\mathbf{k}_{\parallel}^{\text{out}}, \omega_c)$ at ω_c , and then adds the same wavefront correction of $-\phi_{\text{in}}(\mathbf{k}_{\parallel}^{\text{in}}, \omega_c)$ and $-\phi_{\text{out}}(\mathbf{k}_{\parallel}^{\text{out}}, \omega_c)$ to all frequencies.

This wavefront correction procedure is identical to the “closed-loop accumulation of single-scattering” (CLASS) [23, 24] scheme except that VRM builds the coherence-gated matrices from frequency domain while generalizing CLASS to include multiple depth slices (referred to as “volumetric dispersion correction” in Ref. [22]). It starts with selecting J depth slices $\{z_1, \dots, z_J\}$ and building the coherence-gated (cg) reflection matrices at these depths,

$$\tilde{R}_{\text{cg}}(\mathbf{k}_{\parallel}^{\text{out}}, \mathbf{k}_{\parallel}^{\text{in}}; z_j) = \sum_{\omega} R_{\text{dc}}(\mathbf{k}_{\parallel}^{\text{out}}, \mathbf{k}_{\parallel}^{\text{in}}, \omega) e^{i(k_z^{\text{out}} - k_z^{\text{in}})(z_j - z_{\text{max}})}, \quad (\text{S53})$$

with the dispersion-compensated reflection matrix $R_{\text{dc}}(\mathbf{k}_{\parallel}^{\text{out}}, \mathbf{k}_{\parallel}^{\text{in}}, \omega)$ from Eq. (S48). Another iterative phase conjugation follows, as

$$\tilde{R}_{\text{cg},j}^{(n+1)}(\mathbf{k}_{\parallel}^{\text{out}}, \mathbf{k}_{\parallel}^{\text{in}}) = e^{-i\Delta\phi_{\text{out}}^{(n)}(\mathbf{k}_{\parallel}^{\text{out}})} \tilde{R}_{\text{cg},j}^{(n)}(\mathbf{k}_{\parallel}^{\text{out}}, \mathbf{k}_{\parallel}^{\text{in}}) e^{-i\Delta\phi_{\text{in}}^{(n)}(\mathbf{k}_{\parallel}^{\text{in}})}, \quad (\text{S54})$$

with $n = 0, 1, 2, \dots$ and with initial condition $\tilde{R}_{\text{cg},j}^{(0)}(\mathbf{k}_{\parallel}^{\text{out}}, \mathbf{k}_{\parallel}^{\text{in}}) = \tilde{R}_{\text{cg}}(\mathbf{k}_{\parallel}^{\text{out}}, \mathbf{k}_{\parallel}^{\text{in}}; z_j)$, $\Delta\phi_{\text{in}}^{(0)}(\mathbf{k}_{\parallel}^{\text{in}}) = \Delta\phi_{\text{out}}^{(0)}(\mathbf{k}_{\parallel}^{\text{out}}) = 0$. The correction at the n -th iteration is determined by phase conjugation,

$$\Delta\phi_{\text{in}}^{(n)}(\mathbf{k}_{\parallel}^{\text{in}}) = \arg \left[\sum_{j, \Delta\mathbf{k}_{\parallel}} \tilde{R}_{\text{cg},j}^{(n)}(\mathbf{k}_{\parallel}^{\text{in}} + \Delta\mathbf{k}_{\parallel}, \mathbf{k}_{\parallel}^{\text{in}}) \tilde{R}_{\text{cg},j}^{(n)*}(\Delta\mathbf{k}_{\parallel}) \right], \quad (\text{S55})$$

$$\Delta\phi_{\text{out}}^{(n)}(\mathbf{k}_{\parallel}^{\text{out}}) = \arg \left[\sum_{j, \Delta\mathbf{k}_{\parallel}} \tilde{R}_{\text{cg},j}^{(n)}(\mathbf{k}_{\parallel}^{\text{out}}, \mathbf{k}_{\parallel}^{\text{out}} - \Delta\mathbf{k}_{\parallel}) \tilde{R}_{\text{cg},j}^{(n)*}(\Delta\mathbf{k}_{\parallel}) \right], \quad (\text{S56})$$

where

$$\tilde{R}_{\text{cg},j}^{(n)}(\Delta\mathbf{k}_{\parallel}) = \sum_{\mathbf{k}_{\parallel}^{\text{in}}} \tilde{R}_{\text{cg},j}^{(n)}(\mathbf{k}_{\parallel}^{\text{in}} + \Delta\mathbf{k}_{\parallel}, \mathbf{k}_{\parallel}^{\text{in}}) \quad (\text{S57})$$

is the confocal and coherence-gated (cgg) reflection matrix at depth z_j . Here, we iterate to the N_{wc} -th iteration, until $|\Delta\phi_{\text{in}}^{(n)}(\mathbf{k}_{\parallel}^{\text{in}})|$ and $|\Delta\phi_{\text{out}}^{(n)}(\mathbf{k}_{\parallel}^{\text{out}})|$ are both smaller than 10° for every $\mathbf{k}_{\parallel}^{\text{in}}$ and every $\mathbf{k}_{\parallel}^{\text{out}}$.

Ref. [22] only reported images at these individual slices $\{z_j\}$, obtained by taking the inverse Fourier transform of the final confocal and coherence-gated reflection matrices similar to Eq. (S37),

$$I_{\text{VRM}}(\mathbf{r}_{\parallel}, z_j) = \left| \sum_{\Delta\mathbf{k}_{\parallel}} e^{i\Delta\mathbf{k}_{\parallel} \cdot \mathbf{r}_{\parallel}} \tilde{R}_{\text{cgg},j}^{(N_{\text{wc}}+1)}(\Delta\mathbf{k}_{\parallel}) \right|^2. \quad (\text{S58})$$

In order to examine how VRM works for volumetric reconstruction, here we generalize Eq. (S58) to

$$I_{\text{VRM}}(\mathbf{r}) = \left| \sum_{\mathbf{k}_{\parallel}^{\text{out}}, \mathbf{k}_{\parallel}^{\text{in}}, \omega} e^{i(\mathbf{k}_{\text{out}} - \mathbf{k}_{\text{in}}) \cdot \mathbf{r}} R_{\text{VRM}}(\mathbf{k}_{\parallel}^{\text{out}}, \mathbf{k}_{\parallel}^{\text{in}}, \omega) \right|^2, \quad (\text{S59})$$

with the wavefront-corrected (wc) reflection matrix

$$R_{\text{VRM}}(\mathbf{k}_{\parallel}^{\text{out}}, \mathbf{k}_{\parallel}^{\text{in}}, \omega) \equiv e^{-i\phi_{\text{out}}(\mathbf{k}_{\parallel}^{\text{out}}) - i\phi_{\text{in}}(\mathbf{k}_{\parallel}^{\text{in}}) - i(k_z^{\text{out}} - k_z^{\text{in}})z_{\text{max}}} R_{\text{dc}}(\mathbf{k}_{\parallel}^{\text{out}}, \mathbf{k}_{\parallel}^{\text{in}}, \omega), \quad (\text{S60})$$

where $\phi_{\text{in}}(\mathbf{k}_{\parallel}^{\text{in}}) = \sum_{n=1}^{N_{\text{wc}}} \Delta\phi_{\text{in}}^{(n)}(\mathbf{k}_{\parallel}^{\text{in}})$ and $\phi_{\text{out}}(\mathbf{k}_{\parallel}^{\text{out}}) = \sum_{n=1}^{N_{\text{wc}}} \Delta\phi_{\text{out}}^{(n)}(\mathbf{k}_{\parallel}^{\text{out}})$, with $R_{\text{dc}}(\mathbf{k}_{\parallel}^{\text{out}}, \mathbf{k}_{\parallel}^{\text{in}}, \omega)$ from Eq. (S48). Note that Eq. (S59) was not derived and not used in Ref. [22], but it mathematically reduces to Eq. (S58) when $z = z_j$, so we use it to extend the formalism of Ref. [22] from individual slices to volumetric reconstruction. This $I_{\text{VRM}}(\mathbf{r})$ in Eq. (S59) is the VRM image we build.

To facilitate comparison with SMT, here we carry out an analysis similar to that in the dispersion compensation section above. The objective function that the VRM wavefront correction implicitly maximizes is

$$M_{\text{wc}}^{\text{VRM}} \equiv \sum_{\mathbf{r} \in \{z_j\}} I_{\text{VRM}}(\mathbf{r}), \quad (\text{S61})$$

where $\sum_{\mathbf{r} \in \{z_j\}}$ denotes $\mathbf{r} = (x, y, z)$ with summations over x and y in the FOV and summations over z at the chosen J depth slices $\{z_1, \dots, z_J\}$. We can show that

$$\frac{\partial M_{\text{wc}}^{\text{VRM}}}{\partial \phi_{\text{in}}(\mathbf{k}_{\parallel}^{\text{in}})} \propto \text{Im} \left[\sum_{j, \Delta\mathbf{k}_{\parallel}} \tilde{R}_{\text{cgg},j}(\mathbf{k}_{\parallel}^{\text{in}} + \Delta\mathbf{k}_{\parallel}, \mathbf{k}_{\parallel}^{\text{in}}) \tilde{R}_{\text{cgg},j}^*(\Delta\mathbf{k}_{\parallel}) \right]. \quad (\text{S62})$$

When the VRM wavefront correction converges, $\Delta\phi_{\text{in}}^{(N)}(\mathbf{k}_{\parallel}^{\text{in}}) \approx 0$, so the term inside the square brackets of Eq. (S55) is purely real, and $\frac{\partial M_{\text{wc}}^{\text{VRM}}}{\partial \phi_{\text{in}}(\mathbf{k}_{\parallel}^{\text{in}})} \approx 0$. We can similarly show that $\frac{\partial M_{\text{wc}}^{\text{VRM}}}{\partial \phi_{\text{out}}(\mathbf{k}_{\parallel}^{\text{out}})} \approx 0$ when the VRM wavefront correction converges. Therefore, we conclude that the iterative phase conjugation of VRM wavefront correction (and similarly of CLASS) reaches a local maximum of $M_{\text{wc}}^{\text{VRM}}$ in Eq. (S61).

This analysis allows direct comparison between the VRM wavefront correction above and the SMT wavefront correction of Supplementary Sect. III F. We see four major differences:

1. To avoid overfitting, SMT regularize the problem by expanding $\phi_{\text{in}}(\mathbf{k}_{\parallel}^{\text{in}})$ and $\phi_{\text{out}}(\mathbf{k}_{\parallel}^{\text{out}})$ in Zernike polynomials and only using the Zernike coefficients as the free variables. In CLASS and VRM, every $\phi_{\text{in}}(\mathbf{k}_{\parallel}^{\text{in}})$ and every $\phi_{\text{out}}(\mathbf{k}_{\parallel}^{\text{out}})$ is a free variable.
2. SMT starts from an initial guess of no wavefront correction, $\phi_{\text{in}}(\mathbf{k}_{\parallel}^{\text{in}}) = \phi_{\text{out}}(\mathbf{k}_{\parallel}^{\text{out}}) = 0$. VRM starts with the $\phi_{\text{in}}(\mathbf{k}_{\parallel}^{\text{in}}, \omega)$ and $\phi_{\text{out}}(\mathbf{k}_{\parallel}^{\text{out}}, \omega)$ from its dispersion compensation step.
3. To avoid getting trapped in a poor local optimum, SMT first optimizes $\phi_{\text{in/out}}$ over the full volume and then progressively optimizes over smaller zones while using the previous $\phi_{\text{in/out}}$ as the initial guess. There is no such progression in CLASS and VRM. As shown in Fig. 2c-f of the main text, optimizing the wavefront inside smaller zones without regularization and progression can result in an image that is brighter but with worse quality.
4. SMT also increases the number of Zernike terms when progressing to smaller zones to account for the relation between isoplanatic patch size and the smoothness of wavefront variation. This is not possible in CLASS and VRM.

While the VRM wavefront correction uses multiple slices, it cannot reverse the over-optimization of the intensity at the single slice z_{\max} during the VRM dispersion compensation because the wavefront correction does not modify the temporal gate.

The formalism above starts from the reflection matrix $R(\mathbf{k}_{\parallel}^{\text{out}}, \mathbf{k}_{\parallel}^{\text{in}}, \omega)$ of Eq. (S18b), which has corrected for the refractive index mismatch at interfaces. This is what we use for the 3D nanoparticle colloid sample in Fig. 5 of the main text in order to compare the SMT and VRM images at the same depths.

The VRM formalism from Ref. [22] does not include index-mismatch correction, so we do not include such correction for the 2D USAF target under tissue sample in Fig. 4 of the main text, for which quantitative values of z is not necessary. In this case, we build the VRM image with

$$I_{\text{VRM}}(\mathbf{r}') = \left| \sum_{\mathbf{k}_{\parallel}^{\text{out}}, \mathbf{k}_{\parallel}^{\text{in}}, \omega} e^{-2i\omega\Delta t' + i(\mathbf{k}_{\text{out}}^{\text{air}} - \mathbf{k}_{\text{in}}^{\text{air}}) \cdot \mathbf{r}'} R'_{\text{VRM}}(\mathbf{k}_{\parallel}^{\text{out}}, \mathbf{k}_{\parallel}^{\text{in}}, \omega) \right|^2, \quad (\text{S63})$$

with $\mathbf{r}' = (x, y, z')$, $z' = z^{\text{air}} - z_{\text{ref}}^{\text{air}}$ the apparent depth of the spatial gate relative to the in-air reference plane $z_{\text{ref}}^{\text{air}}$, and with $R'_{\text{VRM}}(\mathbf{k}_{\parallel}^{\text{out}}, \mathbf{k}_{\parallel}^{\text{in}}, \omega)$ built from the reflection matrix $R(\mathbf{k}_{\parallel}^{\text{out}}, \mathbf{k}_{\parallel}^{\text{in}}, \omega)$ without index-mismatch correction. Here, $\Delta t' = [n_{\text{glass}} h^{\text{glass}} + n_{\text{sam}} z - (h^{\text{glass}} + z^{\text{air}})]/c$ is the additional travel time to propagate to z in the sample relative to propagating to the apparent depth z^{air} in air, which aligns the temporal gate with the spatial gate in the presence of index mismatch (also considered in Supplementary Sect. 6 of Ref. [25]). For this 2D target, we build the VRM image at $z' = z'_{\text{target}}$, the depth that maximizes the image intensity integrated over x - y .

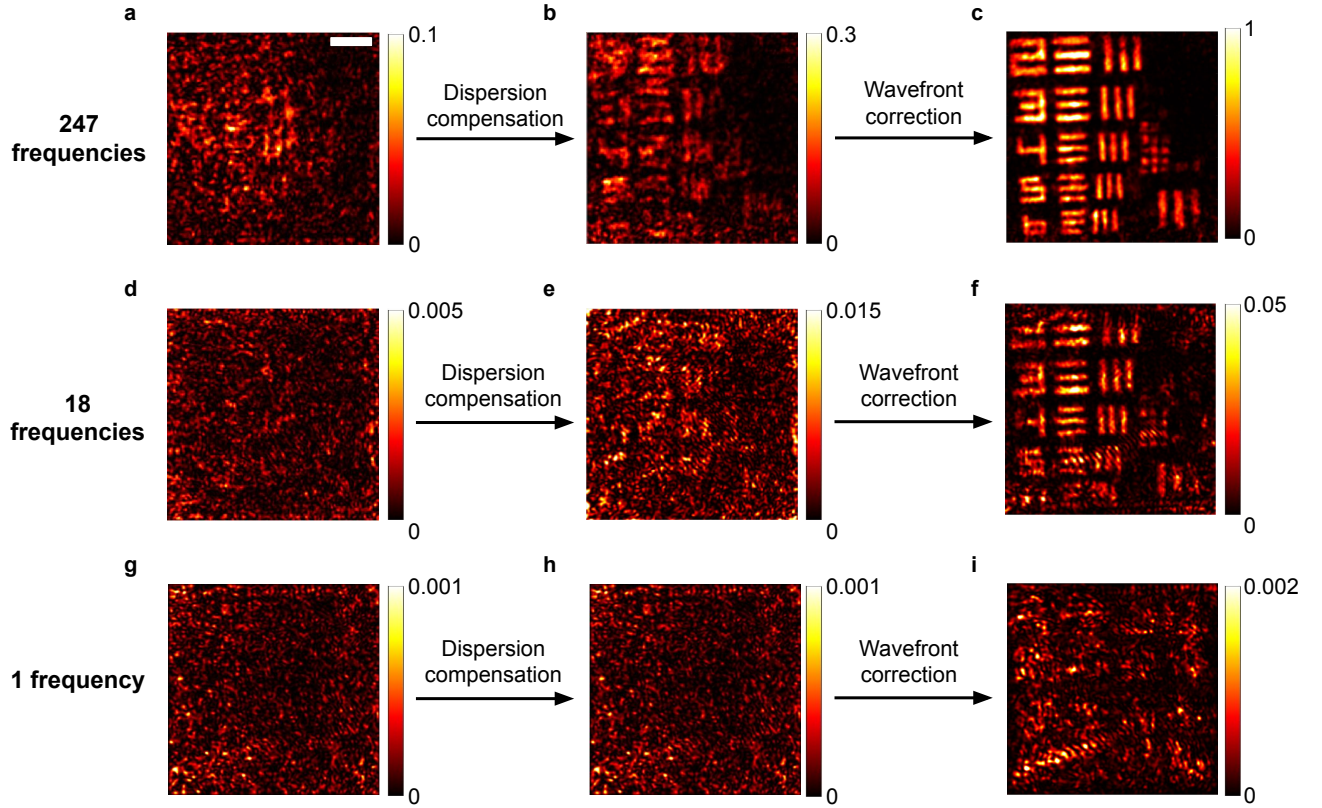
V. SMT WITH FEWER FREQUENCIES

In this section, we study the role of time gating. **Supplementary Fig. 19** shows the SMT images of the USAF-target-under-tissue sample when we keep all 247 frequencies (top row), when we reduce the temporal gate by using only 18 frequencies while keeping the 741–899 nm wavelength range (middle row), and when we completely remove the temporal gate by only using the central frequency (bottom row). SMT still works quite well even when the number of frequencies is reduced by over an order of magnitude. But it utterly fails when the temporal gate is completely removed. This failure is due to two reasons: (1) the single-to-multiple-scattering ratio in ψ_{SMT} is much lower without the temporal gate, and (2) with the lowered single-to-multiple-scattering ratio, wavefronts that maximize the multiple-scattering background may have a comparable or higher image quality metric compared to wavefronts that maximize signals from the target (shown in **Supplementary Fig. 14**), making the optimization fail.

VI. SMT WITH FEWER INCIDENT ANGLES

In this section, we study the role of spatial gating. **Supplementary Fig. 20** shows the SMT images of the USAF-target-under-tissue sample when we keep all 3761 incident angles (top row), when we reduce the spatial gate by using only 750 incident angles while keeping the NA at 0.5 (middle row), and when we completely remove the input spatial gate by only using one incident angle at normal incidence (bottom row). When the input spatial gate is fully removed, the image reconstruction fails even after the optimizations. This failure, similar to the single-frequency case in **Supplementary Fig. 19**, can be attributed (1) a reduced single-to-multiple-scattering ratio in ψ_{SMT} , and (2) a deteriorated optimization landscape due to the reduced single-to-multiple-scattering ratio (**Supplementary Fig. 14**).

Full-field OCT corrected by computational adaptive optics (CAO-FF-OCT) [20, 21] also has no input spatial gate; their output spatial gate is also weaker due to the lower NA used. Previously, CAO-FF-OCT was applied to correct for the aberrations from a plastic layer and thin film of milk [20] and from the retina [21]. The results in **Supplementary Fig. 20g-i** indicate that CAO-FF-OCT would not work in a strongly scattering medium even after increasing the NA and after adopting more advanced optimization strategies because it does not have a confocal spatial gate.



Supplementary Fig. 19. SMT images of the USAF-target-under-tissue sample using all 247 frequencies measured (top row), using 18 frequencies across the full bandwidth (middle row), and using only 1 frequency (bottom row). Scale bar: 10 μm .

VII. POINT SPREAD FUNCTION (PSF)

To evaluate the point spread function (PSF) of the USAF-target-under-tissue sample, we fix the input at \mathbf{r}_{in} while varying the position of the output \mathbf{r} . Specifically, for SMT, we generalize Eq. (2) of the main text to get

$$\text{PSF}_{\text{SMT}}(\mathbf{r}) = \left| \sum_{\omega} e^{i\theta(\omega)} \sum_{\mathbf{k}_{\parallel}^{\text{out}}, \mathbf{k}_{\parallel}^{\text{in}}}^{\text{NA}=0.5} e^{i[\mathbf{k}_{\parallel}^{\text{sam}} \cdot \mathbf{r} - \mathbf{k}_{\parallel}^{\text{sam}} \cdot \mathbf{r}_{\text{in}} + \phi_{\text{out}}(\mathbf{k}_{\parallel}^{\text{out}}) + \phi_{\text{in}}(\mathbf{k}_{\parallel}^{\text{in}})]} R(\mathbf{k}_{\parallel}^{\text{out}}, \mathbf{k}_{\parallel}^{\text{in}}, \omega) \right|^2, \quad (\text{S64})$$

with $\mathbf{r} = (x, y, z_{\text{target}})$ and $\mathbf{r}_{\text{in}} = (x_{\text{in}}, y_{\text{in}}, z_{\text{target}})$. For the other methods, we generalize Eqs. (S31), (S33), (S35), (S63) to get

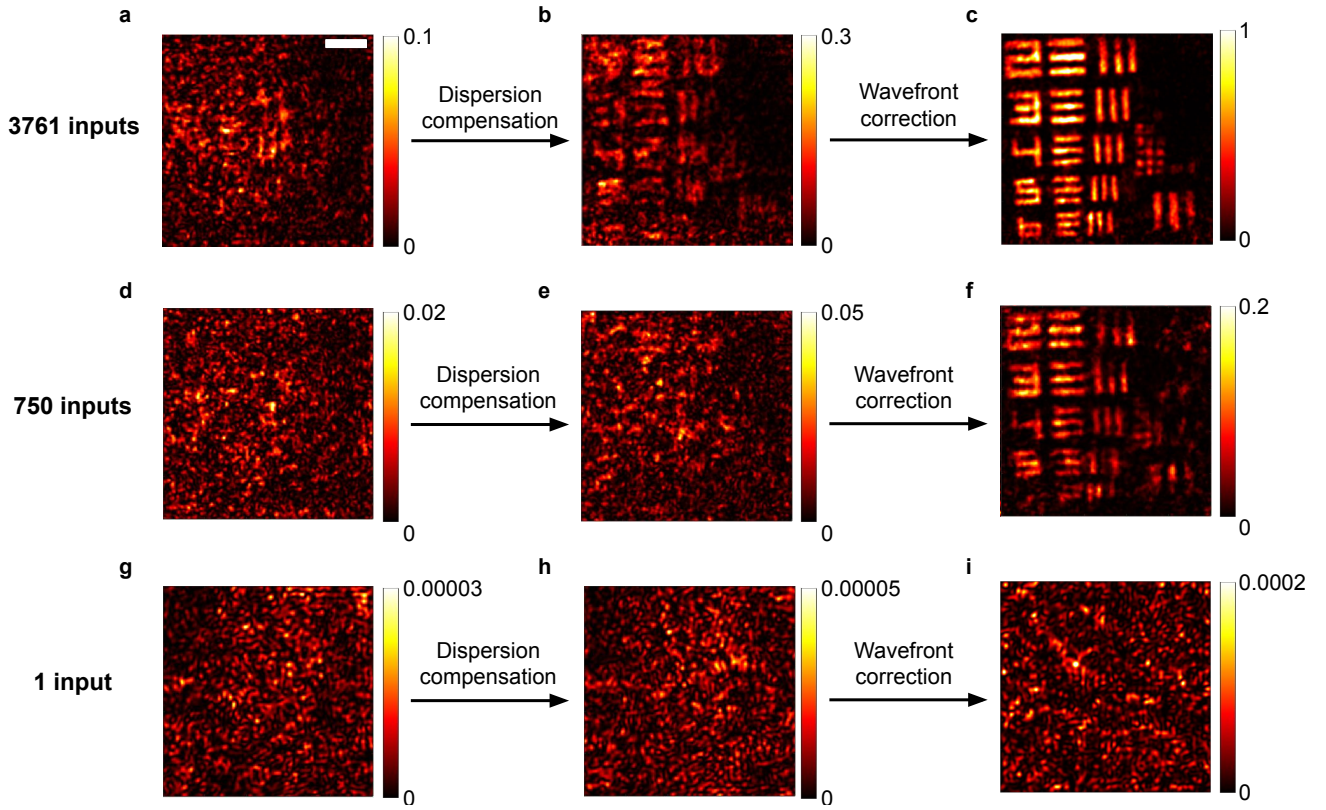
$$\text{PSF}_{\text{RCM}}(\mathbf{r}') = \left| \sum_{\mathbf{k}_{\parallel}^{\text{out}}, \mathbf{k}_{\parallel}^{\text{in}}}^{\text{NA}=0.5} e^{i(\mathbf{k}_{\parallel}^{\text{air}} \cdot \mathbf{r}' - \mathbf{k}_{\parallel}^{\text{air}} \cdot \mathbf{r}'_{\text{in}})} R'(\mathbf{k}_{\parallel}^{\text{out}}, \mathbf{k}_{\parallel}^{\text{in}}, \omega = \omega_{\text{RCM}}) \right|^2, \quad (\text{S65})$$

$$\text{PSF}_{\text{OCM}}(\mathbf{r}') = \left| \sum_{\omega} e^{i\theta_{\text{OCM}}(\omega) - 2i\omega\Delta t'_f} \sum_{\mathbf{k}_{\parallel}^{\text{out}}, \mathbf{k}_{\parallel}^{\text{in}}}^{\text{NA}=0.5} e^{i(\mathbf{k}_{\parallel}^{\text{air}} \cdot \mathbf{r}' - \mathbf{k}_{\parallel}^{\text{air}} \cdot \mathbf{r}'_{\text{in}})} R'(\mathbf{k}_{\parallel}^{\text{out}}, \mathbf{k}_{\parallel}^{\text{in}}, \omega) \right|^2, \quad (\text{S66})$$

$$\text{PSF}_{\text{OCT}}(\mathbf{r}') = \left| \sum_{\omega} e^{i\theta_{\text{OCT}}(\omega) - i\omega\Delta t'_f \left(\frac{1}{\cos\alpha_{\text{in}}} + \frac{1}{\cos\alpha_{\text{out}}} \right)} \sum_{\mathbf{k}_{\parallel}^{\text{out}}}^{\text{NA}=0.1, \alpha_{\text{out}}} \sum_{\mathbf{k}_{\parallel}^{\text{in}}}^{\text{NA}=0.1, \alpha_{\text{in}}} e^{i(\mathbf{k}_{\parallel}^{\text{air}} \cdot \mathbf{r}' - \mathbf{k}_{\parallel}^{\text{air}} \cdot \mathbf{r}'_{\text{in}})} R'(\mathbf{k}_{\parallel}^{\text{out}}, \mathbf{k}_{\parallel}^{\text{in}}, \omega) \right|^2, \quad (\text{S67})$$

$$\text{PSF}_{\text{VRM}}(\mathbf{r}') = \left| \sum_{\omega} e^{-2i\omega\Delta t'_f} \sum_{\mathbf{k}_{\parallel}^{\text{out}}, \mathbf{k}_{\parallel}^{\text{in}}}^{\text{NA}=0.5} e^{i(\mathbf{k}_{\parallel}^{\text{air}} \cdot \mathbf{r}' - \mathbf{k}_{\parallel}^{\text{air}} \cdot \mathbf{r}'_{\text{in}})} R'_{\text{VRM}}(\mathbf{k}_{\parallel}^{\text{out}}, \mathbf{k}_{\parallel}^{\text{in}}, \omega) \right|^2, \quad (\text{S68})$$

with $\mathbf{r}' = (x, y, z'_{\text{target}})$ and $\mathbf{r}'_{\text{in}} = (x_{\text{in}}, y_{\text{in}}, z'_{\text{target}})$.

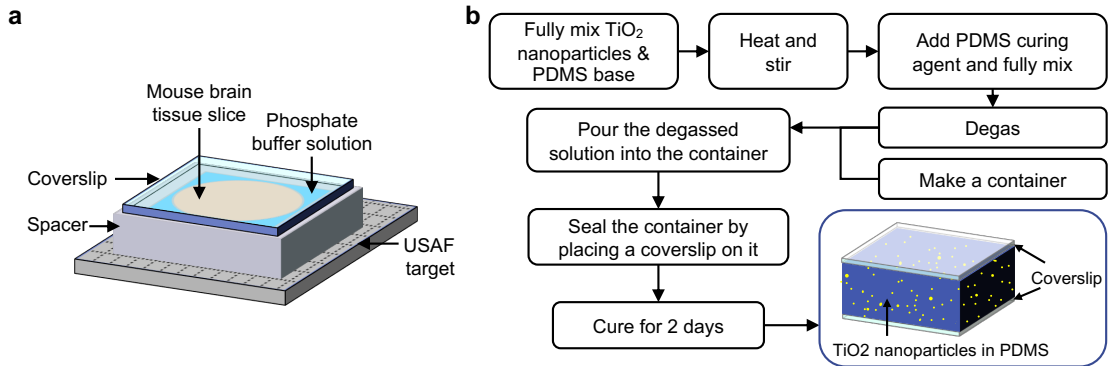


Supplementary Fig. 20. SMT images using all 3761 incident angles measured (top row), using 750 incident angles across the full NA (middle row), and using only 1 incident angle (bottom row). Scale bar: 10 μm .

VIII. SAMPLE PREPARATION

For imaging through tissue, we excised a slice from a fresh CD-1 adult mouse brain that is rinsed of blood (BioChemed Mouse tissue Brain) and placed the tissue slice on top of a USAF target (PhotomaskPORTAL Resolution target RTUSAF519P), immersed in a phosphate buffer solution. The specimen was sealed by a surrounding spacer and a coverslip on top (**Supplementary Fig. 21a**).

The nanoparticle colloid sample consists of a mixture of polydimethylsiloxane (PDMS) silicone (MicroLubrol SYL-CAP 284-S) and titanium dioxide (TiO_2) nanoparticles with a mean size of 500-nm diameter. We first dilute the



Supplementary Fig. 21. Sample preparation a. A schematic of the sample with a USAF target beneath mouse brain tissue. The tissue slice is immersed in phosphate buffer solution and sealed by a spacer and a coverslip. **b.** Preparation of the TiO_2 nanoparticle colloid sample.

TiO₂ solution (Sigma-Aldrich Titania nanoparticles 914320) with ethanol and mix it with the PDMS base material. The mixture is stirred and heated at 150 °C on a stirring hot plate until it is fully mixed and water and ethanol have evaporated. Then, we add the curing agent of PDMS into the mixture and stir at room temperature. After a thorough mix, the solution is placed into a vacuum chamber for degassing. We make a container by placing tapes (thickness of 2-3 mm) on a coverslip and then pour the degassed solution into the container. The sample is sealed by another coverslip on top and cured for 2 days at room temperature (**Supplementary Fig. 21b**).

The TiO₂ mass concentration of the sample is 1.8 ppm which gives a volume particle number density of $n_v = 6.35 \times 10^{-3} \mu\text{m}^{-3}$ with the material density of $\rho_{\text{TiO}_2} = 4.23 \text{ g/cm}^3$ [26] and $\rho_{\text{PDMS}} = 0.965 \text{ g/cm}^3$ [27]. Mie theory [28] yields a scattering cross section of $\sigma = 0.839 \mu\text{m}^2$ and anisotropy factor of $g = 0.599$ for 500-nm particle diameter and wavelength $\lambda = 840 \text{ nm}$, with the particle and the background refractive indices being 2.51 [29] and 1.41 [7]. The volume fraction of TiO₂ is 0.04%, sufficiently low that spatial correlation effects [30] are expected to be negligible, so we use the independent-particle approximation [31] to obtain the scattering mean free path as $\ell_{\text{sca}} = 1/(n_v\sigma) = 0.19 \text{ mm}$ and the transport mean free path as $\ell_{\text{tr}} = 1/[n_v\sigma(1-g)] = 0.47 \text{ mm}$.

IX. RESOLUTION AND DEPTH OF FIELD OF SMT

In this section, we consider the resolution and depth of field (DOF) for the nanoparticle colloid sample, with theoretical estimates and a statistical analysis on the experimental data.

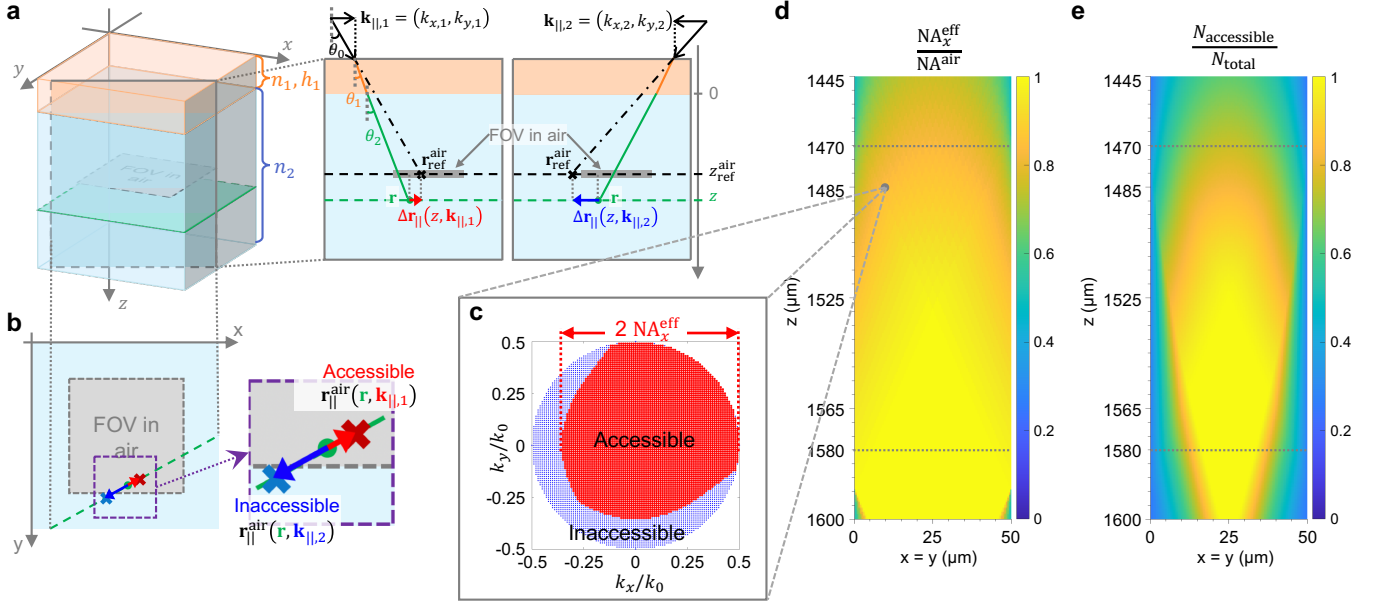
The simplest form of SMT is $\psi_{\text{SMT}}(\mathbf{r}) = \sum_{\mathbf{k}_{\text{out}}, \mathbf{k}_{\text{in}}, \omega} e^{i(\mathbf{k}_{\text{out}} - \mathbf{k}_{\text{in}}) \cdot \mathbf{r}} S(\mathbf{k}_{\text{out}}, \mathbf{k}_{\text{in}}, \omega)$. Here, we can see that the spatial dependence comes from $e^{i(\mathbf{k}_{\text{out}} - \mathbf{k}_{\text{in}}) \cdot \mathbf{r}}$, so the spread of $\mathbf{k}_{\text{out}} - \mathbf{k}_{\text{in}}$ in the summation determines the spatial resolution. When the FOV of illumination and detection is infinite, the spread of $\mathbf{k}_{\text{out}} - \mathbf{k}_{\text{in}}$ will be the same everywhere, giving SMT a location-independent resolution and an infinite DOF. In practice, the FOV is finite, so the large-angle beams will cease to illuminate the FOV of interest and/or cease to be detected at depths z sufficiently far from the reference plane under which the reflection matrix was measured. This reduces the lateral resolution and the signal strength away from the reflection-matrix reference plane, giving SMT a finite (but still large) DOF. Roughly speaking, the SMT DOF covers the volume of overlap among the input/output beams in the scattering matrix data.

A. Theoretical axial resolution

The frequency summation and the angular summations both contribute to the axial spread of $\mathbf{k}_{\text{out}} - \mathbf{k}_{\text{in}}$. In other words, the temporal gate and the spatial gate both set the axial resolution, with the tighter gate being the main factor. The maximal axial spread of $\mathbf{k}_{\text{out}} - \mathbf{k}_{\text{in}}$ comes from small incident angles, so it is roughly depth independent. For the nanoparticle colloid sample, the expected diffraction-limited axial resolution from the spatial gate is approximately $2z_{\text{R}} = 2n_{\text{sam}}\lambda_0/(\pi\text{NA}^2) \approx 2.99 \mu\text{m}$, with center wavelength $\lambda_0 = 840 \text{ nm}$ and $n_{\text{sam}} = 1.4$ for PDMS. Meanwhile, the expected bandwidth-limited FWHM axial resolution from the temporal gate is $\delta z = \gamma \frac{2 \ln 2}{n_{\text{sam}} \pi} \frac{\lambda_0^2}{\Delta \lambda} = 1.42 \mu\text{m}$, where $\Delta \lambda = 187 \text{ nm}$ is the bandwidth and $\gamma = 1.19$ for a flat-top spectrum [32]. The latter is tighter and determines the axial resolution here. Dispersion, aberration, and scattering degrade the resolution, but the dispersion compensation and wavefront correction of SMT can restore the resolution to near the ideal value.

B. Theoretical lateral resolution and depth of field

For the lateral resolution and the DOF, we analyze the range of accessible angles at point \mathbf{r} in the sample, using geometric optics. The range of accessible angles sets the lateral resolution through the lateral spread of $\mathbf{k}_{\text{out}} - \mathbf{k}_{\text{in}}$, and it also provides the signal strength at \mathbf{r} . In our setup (Supplementary Sect. IA), the camera sensor plane is conjugate to the focal plane of the objective lens, so the reference planes for the illumination and detection are both at $z_{\text{ref}}^{\text{air}}$ in air. The area that the camera sensor images at $z_{\text{ref}}^{\text{air}}$ is labeled by the gray square as ‘‘FOV in air’’ in **Supplementary Fig. 22a–b**. Given a point $\mathbf{r} = (\mathbf{r}_{\parallel}, z)$ in the sample and a transverse momentum \mathbf{k}_{\parallel} , we can backpropagate the associated ray to air (while accounting for refraction at the interfaces) and then forward propagate the ray (without refraction) to find its would-be intersection point with the reference plane in air if the sample is not there, $\mathbf{r}_{\text{ref}}^{\text{air}} = (x^{\text{air}}, y^{\text{air}}, z_{\text{ref}}^{\text{air}})$ (**Supplementary Fig. 22a**). If $\mathbf{r}_{\parallel}^{\text{air}} = (x^{\text{air}}, y^{\text{air}})$ is within the FOV in air (the gray square), such transverse momentum \mathbf{k}_{\parallel} is accessible at point \mathbf{r} in the sample. If $\mathbf{r}_{\parallel}^{\text{air}}$ is outside the gray square, then this \mathbf{k}_{\parallel} is not accessible, meaning such ray cannot be detected by the camera. **Supplementary Fig. 22a–b** schematically illustrate examples of an accessible \mathbf{k}_{\parallel} (in red) and an inaccessible \mathbf{k}_{\parallel} (in blue).



Supplementary Fig. 22. Theoretical lateral resolution, signal strength, and depth of field for the nanoparticle colloid sample. **a.** For each point \mathbf{r} in the sample and each transverse momentum \mathbf{k}_{\parallel} , we can determine its would-be position $\mathbf{r}_{\text{ref}}^{\text{air}}$ at the reference plane $z_{\text{ref}}^{\text{air}}$ in air, which is the plane imaged by the camera. **b.** When $\mathbf{r}_{\text{ref}}^{\text{air}}$ falls within the FOV in air, the \mathbf{k}_{\parallel} is accessible (red). When $\mathbf{r}_{\text{ref}}^{\text{air}}$ falls outside the FOV in air, the \mathbf{k}_{\parallel} is not accessible (blue). **c.** Example of accessible and inaccessible \mathbf{k}_{\parallel} points, at $\mathbf{r} = (10, 10, 1485) \mu\text{m}$. **d.** Effective NA defined by the range of accessible angles, which determines the ideal (diffraction-limited) lateral resolution. **e.** Ratio of accessible \mathbf{k}_{\parallel} points, which determines the overall signal strength in SMT.

Specifically, here we have the sample refractive index $n_2 = n_{\text{sam}} = 1.4$ (PDMS), a coverslip with thickness $h_1 = h_{\text{glass}} = 154 \mu\text{m}$ and refractive index $n_1 = n_{\text{glass}} = 1.5$, and a reference plane of $z_{\text{ref}}^{\text{air}} = 996 \mu\text{m}$. Using Snell's law and geometry, we obtain

$$\Delta \mathbf{r}_{\parallel} \equiv \mathbf{r}_{\parallel}^{\text{air}} - \mathbf{r}_{\parallel} = [(z_{\text{ref}}^{\text{air}} + h_1) \tan \theta_0 - h_1 \tan \theta_1 - z \tan \theta_2] \frac{\mathbf{k}_{\parallel}}{|\mathbf{k}_{\parallel}|}, \quad \sin \theta_0 = n_1 \sin \theta_1 = n_2 \sin \theta_2 = |\mathbf{k}_{\parallel}|/k_0, \quad (\text{S69})$$

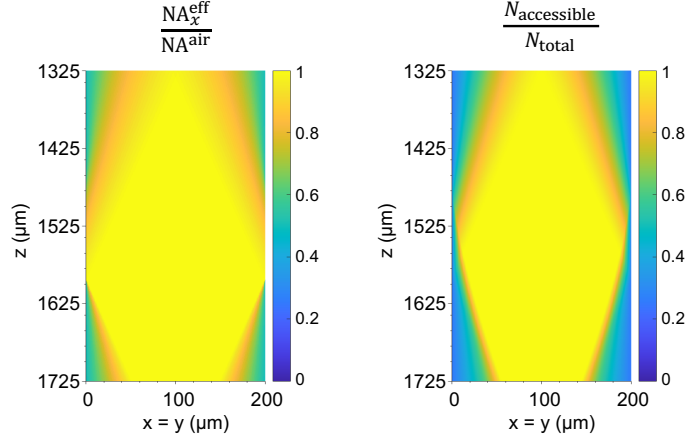
where θ_0 , θ_1 and θ_2 are the propagation angles relative to the z axis in different media, and $k_0 = 2\pi/\lambda$ is the vacuum wave number. Note that the in-plane momentum $\mathbf{k}_{\parallel} = (k_x, k_y)$ is the same in all media. For each point \mathbf{r} in the 3D space of the sample, we loop through the list of in-plane momentum \mathbf{k}_{\parallel} within the NA of the objective lens and use Eq. (S69) to determine if each \mathbf{k}_{\parallel} is accessible or not. We denote the accessible ones as $\mathbf{k}_{\parallel}^{\text{accessible}} = (k_x^{\text{accessible}}, k_y^{\text{accessible}})$. **Supplementary Fig. 22c** provides an example.

The ideal (diffraction-limited) lateral resolution is determined primarily by the maximal spread of $\mathbf{k}_{\parallel}^{\text{out}} - \mathbf{k}_{\parallel}^{\text{in}}$. Since we use the same NA for the input and the output, this is determined by the maximal spread of \mathbf{k}_{\parallel} . So, we define an effective NA as

$$\text{NA}_x^{\text{eff}} \equiv \frac{\max(k_x^{\text{accessible}}) - \min(k_x^{\text{accessible}})}{2k_0} \quad (\text{S70})$$

and similarly for NA_y^{eff} . **Supplementary Fig. 22d** plots NA_x^{eff} along a diagonal ($x = y$) slice of the 3D sample. Within the total volume we consider in Fig. 4 of the main text (from $z = 1470 \mu\text{m}$ to $z = 1580 \mu\text{m}$, indicated by dashed lines), NA_x^{eff} remains close to the ideal value of $\text{NA}^{\text{air}} = 0.5$. If one defines the DOF as where the lateral resolution increases by a factor of $\sqrt{2}$ (which is the typical definition in RCM and OCM/OCT), the SMT DOF will be much larger than the $110 \mu\text{m}$ considered.

Note that the NA_x^{eff} in **Supplementary Fig. 22d** is asymmetric in z . This is because of the refraction at the air-glass and glass-sample interfaces. As mentioned in Supplementary Sect. IIID and illustrated in **Supplementary Fig. 8b**, the depth z_f^{sam} of the focal plane in the sample depends on the incident angle. Here, $z_f^{\text{sam}}(0^\circ) = 1466 \mu\text{m}$ and $z_f^{\text{sam}}(30^\circ) = 1594 \mu\text{m}$. Since NA_x^{eff} is determined by the maximal angle, it is larger near $z_f^{\text{sam}}(30^\circ) = 1594 \mu\text{m}$, so the lateral resolution is the sharpest there. Without refractive index mismatches, z_f^{sam} will be independent of the incident angle, and NA_x^{eff} will decay symmetrically away from the reference plane.



Supplementary Fig. 23. Depth of field with expanded field of view. The effective NA (left) and the ratio of accessible k_{\parallel} (right) when the field of view is 200 μm .

The strength of the signal depends on the number of accessible k_{\parallel} . Therefore, in **Supplementary Fig. 22e**, we plot the ratio $N_{\text{accessible}}/N_{\text{total}}$ between the number of accessible k_{\parallel} points and the total number of k_{\parallel} within the NA of the objective lens. This ratio remains above 0.5 across most points within the volume considered in the main text.

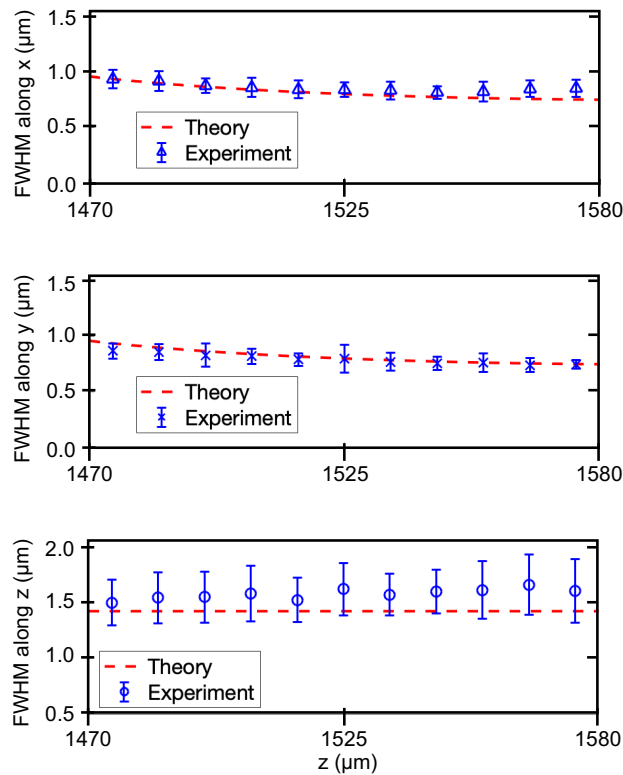
With the geometry shown above, we expect the SMT DOF to grow with the FOV. As an example, **Supplementary Fig. 23** shows the corresponding predictions given a FOV of 200 μm . In this case, SMT has a DOF of roughly 400 μm .

C. Experimental FWHM resolution

To systematically study the resolution of the experimental SMT image, we use the Trackmate [33, 34] plugin in Fiji [35] with a Laplacian of Gaussian (LoG) detector to analyze the 3D SMT image of the nanoparticle colloid, setting the estimated diameter as 4 pixels (0.2 μm per pixel), quality threshold as 130. The analysis locates $\sim 3,610$ particles. For each located particle, we extract the FWHM resolution of its SMT image along the x , y , and z directions using the `findpeaks` function in MATLAB. We bin the data set with a depth interval of 10 μm and calculate the mean and standard deviation within each depth interval, with results shown in **Supplementary Fig. 24**. The FWHM resolution in y is slightly better than in x because our incident angular range in y is larger after excluding incident angles with weak signals (Supplementary Sect. I C).

We also plot the theoretically predicted results as red dashed lines. For the lateral resolution, we use the model of Supplementary Sect. IX B above to calculate $\text{NA}^{\text{eff}}(x, y, z)$ at each position (x, y, z) in the 3D volume and average over (x, y) for each z to obtain $1/\text{NA}^{\text{eff}}(z) \equiv \langle 1/\text{NA}^{\text{eff}}(x, y, z) \rangle_{x, y}$ to model the z dependence of the lateral resolution. For the axial resolution, we show the theoretical estimate of $\delta z = 1.42 \mu\text{m}$ from Supplementary Sect. IX A.

-
- [1] N. Verrier and M. Atlan, Off-axis digital hologram reconstruction: some practical considerations, *Appl. Opt.* **50**, H136 (2011).
 - [2] H. Yu, T. R. Hillman, W. Choi, J. O. Lee, M. S. Feld, R. R. Dasari, and Y. Park, Measuring large optical transmission matrices of disordered media, *Phys. Rev. Lett.* **111**, 153902 (2013).
 - [3] C. Wang, X. Lee, T. Cui, Y. Qu, Y. Li, H. Li, and Q. Wang, Reducing the influence of direct reflection on return signal detection in a 3D imaging lidar system by rotating the polarizing beam splitter, *Appl. Opt.* **55**, 1559 (2016).
 - [4] Phantom TMX 7510, <https://www.phantomhighspeed.com/products/cameras/tmx/7510>.
 - [5] Refractive index of SCHOTT multiple purpose D263TECO, <https://refractiveindex.info/?shelf=glass&book=SCHOTT-multipurpose&page=D263TECO>.
 - [6] M. Daimon and A. Masumura, Measurement of the refractive index of distilled water from the near-infrared region to the ultraviolet region, *Appl. Opt.* **46**, 3811 (2007).
 - [7] V. Gupta, P. T. Probst, F. R. Gößler, A. M. Steiner, J. Schubert, Y. Brasse, T. A. F. König, and A. Fery, Mechanotunable



Supplementary Fig. 24. Experimental FWHM resolution of nanoparticle colloid. Each experimental data point is the mean value over a 10- μm depth interval, with error bars indicating plus/minus one standard deviation.

surface lattice resonances in the visible optical range by soft lithography templates and directed self-assembly, *ACS Appl. Mater. Interfaces* **11**, 28189 (2019).

- [8] M. N. Polyanskiy, Refractive index database, <https://refractiveindex.info>.
- [9] M. Wojtkowski, V. J. Srinivasan, T. H. Ko, J. G. Fujimoto, A. Kowalczyk, and J. S. Duker, Ultrahigh-resolution, high-speed, Fourier domain optical coherence tomography and methods for dispersion compensation, *Opt. Express* **12**, 2404 (2004).
- [10] S. G. Johnson, The NLOpt nonlinear-optimization package, <http://github.com/stevengj/nlopt>.
- [11] D. C. Liu and J. Nocedal, On the limited memory BFGS method for large scale optimization, *Math. Program.* **45**, 503 (1989).
- [12] P. Fricker, Zernike polynomials, <https://www.mathworks.com/matlabcentral/fileexchange/7687-zernike-polynomials> (2023), MATLAB Central File Exchange.
- [13] P. Calzavara-Pinton, C. Longo, M. Venturini, R. Sala, and G. Pellacani, Reflectance confocal microscopy for in vivo skin imaging, *Photochem. Photobiol.* **84**, 1421 (2008).
- [14] S. Kang, S. Jeong, W. Choi, H. Ko, T. D. Yang, J. H. Joo, J.-S. Lee, Y.-S. Lim, Q.-H. Park, and W. Choi, Imaging deep within a scattering medium using collective accumulation of single-scattered waves, *Nat. Photon.* **9**, 253 (2015).
- [15] C. W. Hsu, A. Goetschy, Y. Bromberg, A. D. Stone, and H. Cao, Broadband coherent enhancement of transmission and absorption in disordered media, *Phys. Rev. Lett.* **115**, 223901 (2015).
- [16] S. G. Adie, B. W. Graf, A. Ahmad, P. S. Carney, and S. A. Boppart, Computational adaptive optics for broadband optical interferometric tomography of biological tissue, *Proc. Natl. Acad. Sci. U.S.A.* **109**, 7175 (2012).
- [17] N. D. Shemonski, F. A. South, Y.-Z. Liu, S. G. Adie, P. S. Carney, and S. A. Boppart, Computational high-resolution optical imaging of the living human retina, *Nat. Photon.* **9**, 440–443 (2015).
- [18] F. A. South, Y.-Z. Liu, P.-C. Huang, T. Kohlfarber, and S. A. Boppart, Local wavefront mapping in tissue using computational adaptive optics oct, *Opt. Lett.* **44**, 1186 (2019).
- [19] S. Liu, F. Xia, X. Yang, M. Wu, L. A. Bizimana, C. Xu, and S. G. Adie, Closed-loop wavefront sensing and correction in the mouse brain with computed optical coherence microscopy, *Biomed. Opt. Express* **12**, 4934 (2021).
- [20] A. Kumar, W. Drexler, and R. A. Leitgeb, Subaperture correlation based digital adaptive optics for full field optical coherence tomography, *Opt. Express* **21**, 10850 (2013).
- [21] D. Hillmann, H. Spahr, C. Hain, H. Sudkamp, G. Franke, C. Pfäffle, C. Winter, and G. Hüttmann, Aberration-free volumetric high-speed imaging of in vivo retina, *Sci. Rep.* **6**, 35209 (2016).

- [22] Y.-R. Lee, D.-Y. Kim, Y. Jo, M. Kim, and W. Choi, Exploiting volumetric wave correlation for enhanced depth imaging in scattering medium, *Nat. Commun.* **14**, 1878 (2023).
- [23] S. Kang, P. Kang, S. Jeong, Y. Kwon, T. D. Yang, J. H. Hong, M. Kim, K.-D. Song, J. H. Park, J. H. Lee, *et al.*, High-resolution adaptive optical imaging within thick scattering media using closed-loop accumulation of single scattering, *Nat. Commun.* **8**, 2157 (2017).
- [24] S. Yoon, H. Lee, J. H. Hong, Y.-S. Lim, and W. Choi, Laser scanning reflection-matrix microscopy for aberration-free imaging through intact mouse skull, *Nat. Commun.* **11**, 5721 (2020).
- [25] Z. Wang, Y. Zhang, and C. W. Hsu, Full-wave simulations of tomographic optical imaging inside scattering media, preprint at <https://arxiv.org/abs/2308.07244> (2023).
- [26] T. Theivasanthi and M. Alagar, Titanium dioxide (TiO₂) nanoparticles XRD analyses: an insight, arXiv:1307.1091 (2013).
- [27] S. Mohanty, L. B. Larsen, J. Trifol, P. Szabo, H. V. R. Burri, C. Canali, M. Dufva, J. Emnéus, and A. Wolff, Fabrication of scalable and structured tissue engineering scaffolds using water dissolvable sacrificial 3D printed moulds, *Mater. Sci. Eng. C* **55**, 569 (2015).
- [28] C. Mätzler, MATLAB functions for Mie scattering and absorption, Institute of Applied Physics Research Report No. 2002-08, University of Bern (2002).
- [29] J. R. DeVore, Refractive indices of rutile and sphalerite, *J. Opt. Soc. Am.* **41**, 416 (1951).
- [30] L. F. Rojas-Ochoa, J. M. Mendez-Alcaraz, J. J. Sáenz, P. Schurtenberger, and F. Scheffold, Photonic properties of strongly correlated colloidal liquids, *Phys. Rev. Lett.* **93**, 073903 (2004).
- [31] R. Carminati and J. C. Schotland, *Principles of Scattering and Transport of Light* (Cambridge University Press, 2021).
- [32] M. Duell and K. Hsu, SLEDs and swept source laser technology for OCT, in *Optical Coherence Tomography: Technology and Applications*, edited by W. Drexler and J. G. Fujimoto (Springer, 2015) pp. 527–561.
- [33] J.-Y. Tinevez, N. Perry, J. Schindelin, G. M. Hoopes, G. D. Reynolds, E. Laplantine, S. Y. Bednarek, S. L. Shorte, and K. W. Eliceiri, Trackmate: An open and extensible platform for single-particle tracking, *Methods* **115**, 80 (2017).
- [34] D. Ershov, M.-S. Phan, J. W. Pylvänäinen, S. U. Rigaud, L. Le Blanc, A. Charles-Orszag, J. R. W. Conway, R. F. Laine, N. H. Roy, D. Bonazzi, G. Duménil, G. Jacquemet, and J.-Y. Tinevez, Trackmate 7: integrating state-of-the-art segmentation algorithms into tracking pipelines, *Nature Methods* **19**, 829 (2022).
- [35] Fiji: an open-source platform for biological-image analysis, *Nature Methods* **9**, 676 (2012).